Design and Optimization of Adsorption Systems for Automotive Climate Control

by

Cody L. Jacobucci

B.S. Mechanical Engineering

Massachusetts Institute of Technology, 2017

Submitted to the Department of Mechanical Engineering

in partial fulfillment of the requirements for the

Degree of Master of Science in Mechanical Engineering

at the

MASSACHUSETTS INSTITUTE OF TECHNOLOGY

June 2021

Author .....

Department of Mechanical Engineering

May 14, 2021

Certified by .....

Evelyn N. Wang

Department Head; Gail E. Kendall Professor of Mechanical Engineer

Thesis Supervisor

Accepted by .....

Nicolas Hadjiconstantinou

Chairman, Department Committee on Graduate Theses

Design and Optimization of Adsorption Systems for Automotive Climate Control

by

Cody L. Jacobucci

Submitted to the Department of Mechanical Engineering on May 14, 2021

in Partial Fulfillment of the Requirements for the

Degree of Master of Science in Mechanical Engineering

Abstract

Adsorption systems have a wide range of applications that sit at the forefront of challenges presented by climate change, spanning direct air carbon capture, to atmospheric water harvesting, to thermal energy storage. Decades of research and development has led to the optimization of adsorption materials to customize them for a specific application by tailoring their affinity for particular molecules, among other properties. The rapid discovery and development of new metal organic frameworks (MOF), a class of materials that prove to be more customizable than more traditional adsorbents such as zeolites and silica gel, offer promise for sorption systems to be further enhanced. However, the practical design of these systems for climate control and atmospheric water harvesting has yet to be perfected.

Adsorption systems need to balance many factors to be successful for a given objective, weighing the kinetics of a given process against the device mass and volume for a variety of operational conditions. This thesis aims to elucidate design principles and optimization guidelines to facilitate the design and analysis of future sorption systems that are general enough to grow with the field as material and manufacturing capabilities expand.

In this work, we describe the theoretical model used to design and optimize a waste heat driven air conditioning system for an internal combustion engine vehicle. The proposed device has a tube and fin architecture, where each fin has copper foam brazed to it to serve as a porous, conductive scaffold for the deposition of AQSOA Z02. The device will use the waste heat from the engine coolant at 90 ℃ for desorption, and produce 1.5 kW cooling power over a 400 second cycle. The proposed design met all of the specifications proposed by Ford for automotive air conditioning systems, marking a significant milestone for the deployment of adsorption-based cooling for portable cooling applications. The design optimization process is repeated to produce a 1:10 scale prototype delivering an average cooling power of 150 W, which is currently under fabrication.

In order to validate our model, we conducted a series of adsorbent coating characterizations in a custom adsorption bed simulator. We found good agreement with the model for traditional immersion drying fabrication techniques. We also propose a new boiling assisted channel templating (BACT) method to facilitate better vapor transport through the coatings to increase the potential cooling power via enhanced adsorption kinetics, reduce material waste, and decrease required fabrication time. This resulted in a performance of a specific cooling power of 1875 W/kg Z02 for a 120 second cycle- a record high number

for Z02 under these operating conditions. Preliminary analysis suggests it would enable a system level specific cooling power of 375 W/kg of the entire adsorbent bed, compared to our previously proposed design with a specific cooling power of 200 W/kg.

In the final chapter, we will review the lessons learned from this work and describe the next steps that we think are essential in translating adsorption technology out of the lab and into real devices for adsorption driven cooling. We also provide recommendations as to how this framework can easily be applied to other adsorption systems, such as atmospheric water harvesting, and next steps for enhancing the performance of BACT samples.

Thesis Supervisor: Evelyn N. Wang

Title: Department Head; Gail E. Kendall Professor of Mechanical Engineering

Acknowledgments

"And whatever you do, in word or deed, do everything in the name of the Lord Jesus, giving thanks to God the Father through him" Colossians 3:23.

I thank God for the privilege I have had to work alongside and grow with the men and women He has placed in my life over this past year and a half. He has provided this opportunity to study at MIT not just once, but twice, given me an incredible community to learn from every day, the perseverance required to work through a largely remote Master's Degree, all while staying healthy, and maintaining and strengthening the relationships that I hold most dear. While I personally own any shortcomings in the work that follows, all of its merit should glorify God and only God.

This work would not have been possible without the unwavering support of my advisor, Evelyn Wang. I will never be able to express gratitude proportionate to the generosity you have shown me in the chance to study in the Device Research Lab, your selfless dedication to each of your students despite having an incredibly heavy load as Department Head during a pandemic and much unrest, nor commensurate to the amount of growth I have felt during this time. Thank you for this chance and your mentorship along the way.

I would like to thank the Device Research Lab in its entirety, from the current members that have taught me so much in and outside of the lab, to alumni (specifically Sameer Rao) that have been generous enough with their time to pass along their lessons learned. Xiangyu Li has been instrumental to my success, offering technical solutions openly in one hand, and perspective in the other when it was needed to encourage me and help me find my way as an independent researcher. I admire his ambition, work ethic, and headstrong pursuit in advancing thermal sciences, as well as his ability to have fun along the way. Bachir El Fil, despite only overlapping for a short period of time, has brought such optimism to this work and I am excited and comforted to know that its completion rests in such capable hands. Finally, rounding out the trio of postdocs I have worked with, Mohammed Alshrah has been an incredible partner in research and thinking about what life has in store for us next. While still in his PhD, Samuel Cruz was there every step of the way, and it has been incredible sharing this research experience and fellowshipping in our faith with each other along the way.

Arny Leroy is the paragon of a curious, creative scientist with the practicality of an engineer at each step, and our discussions that seamlessly bounce back and forth between baking bread and the fundamental processes involved in atmospheric water harvesting will hold a special place in my memory of MIT. His friendship has been incredibly important to me at this time and his example in and out of the lab has helped me find balance in my life, which is often a hard line to follow in graduate school.

I would also like to thank my colleagues, Chad and Carlos, for being such great trench buddies during this degree as we learned heat transfer and how to be a researcher during the pandemic together. Chad has been generous with his time in the lab to help me, and always finds a way to make work fun. I will miss our gym sessions, riverside runs, and life reflections over stretches, but I look forward to making up for them in other ways in the years to come. Carlos has made me at least 15 times better at asking critical questions of my own work and assumptions, as well as served as a model for embodying genuine, relentless interest in the fundamentals of how the world works. His impact on my life, despite knowing each other for such a short period of time, will be far greater than he knows.

In addition, if it was not for his generosity in attending a Camp Kesem fundraiser, I am not sure I ever would have gone to graduate school if it were not for Ahmed Ghoniem. I will always be thankful to you for believing in me. In addition, I would like to thank the Tata Center, specifically Rob Stoner and Jason

Prapas, for their guidance and experience working abroad and instilling a passion for global development in me.

This work would not have been possible without the support of incredible industry professionals I have had the privilege to work with. Hassan Farhat has been instrumental in his guidance of this project. Dr. Jian Yu of Super Radiator Coils went above and beyond to make this project possible for me in such tight timelines, and Bob Carlo has been an incredible pleasure to work with. I thank Bob for his guidance, genuine care for customers, and the beginning of what I hope will be a long friendship, full of calculus lessons and woodshop/tooling advice as we learn so we can build a better world.

It cannot be overstated that Leslie Regan is the unsung hero of every MIT MechE graduate student's experience. Leslie, thank you for giving your all to each and every student, and supporting us every second of the day for even the tiniest of details, all the way up to helping me navigate a difficult time to manage family matters without having to give up on my graduate degree. Leslie is a significant reason for my ability to return to MIT, and it is impossible to thank someone enough for the opportunity to be home when it is needed.

I thank each and every member of my family for their support during this time, and I am not sure I would have gotten through it without the guidance and perspective of my father, Frank. My mother, Terry, has always given me unconditional love that has propelled me forward in all that I do, and my siblings, Colton and Cedona, are the best friends that anyone could ever ask for. Our relationships and unwavering dedication to the support of one another are not only what made my graduation possible, but what makes my life meaningful. I am looking forward to our next adventures together on my return home! I also would like to thank Hal and Trudy Graber for letting us stay with them for the majority of this thesis work. It was a true blessing to be home during COVID, and I appreciate how much closer we grew through it.

I would also like to thank the friends and mentors that I have had through my life that have helped make me who I am, including Trish Hatton, Doug Smith, Alex Kim, Nathan Warfield, Fred Catalano, Jinman Parks, Chris Resto, Julie Knight, Wendy Davis, Jessica Chen, Veronika Johnson, Jacob Jurewicz, Alec Anderson, Dillon Dumesnil, Pete Baddoo, Asher Kaithern, Matthew Kalinowski, Chris Rickard, Dominic Mazzone, Asa and Amber Reini, Jackson Graves, Quantum Wei, Yan Yan, Jackie Xu, Chris Swanson, and of course, my dog- Bear.

Finally, my partner in crime, Hali. Hali is the best friend I have ever had, and the single greatest blessing in my life. There is no one in the world I would want to walk alongside as we undertake the difficult task to further embody Christ's character and share His love with others as freely as it is given to us. You will never cease to amaze me in your selflessness, perspective, and radiative joy that brings every single person you meet up. I have tried in every shape and form, whether it be through prose or art, to express the gratitude I feel for having you as my partner in life, but have always fallen short as I do now. I will love you forever and always, and the only thing more exciting than getting to spend each passing day with you is the one that comes next- the one that holds nothing we can predict except God's faithfulness and the ever-increasing love and joy we share together.

Table of Contents

1. Introduction 16
   1.1. Motivation 16
   1.2. Energy utilization and emissions 17
   1.3. Adsorption and Adsorption Materials 19
   1.4. Adsoprtion Cooling For Automobiles 22
   1.5. Thesis objectives and outline 24
2. Modeling of Waste Heat Driven Adsorption Cooling for Automotive Climate Control 25
   2.1. Cooling cycles 25
   2.2. Material Review 28
   2.3. Design architectures 34
   2.4. Adsorption Layer Modeling Approach 37
   2.5. COMSOL Finite Element Model 39
   2.6. Summary 41
3. Design and Optimization of a Full Scale and Reduced Scale Adsorption Based Cooling System 43
   3.1. Design constraints: Adsorption Bed 43
   3.2. Design Optimization: Adsorption Bed 44
   3.3. Heat Transfer Design Considerations 46
   3.4. Mass Transfer Design Considerations 49
   3.5. Multi-Objective Design Framework 55
   3.6. Device Design Results 56
   3.7. Evaporator Design and Analysis 60
   3.8. Summary 65
4. Adsorption Coating Fabrication and Testing 67
   4.1. Adsorbent Coating Fabrication 67
   4.2. Adsorbent Coating Fabrication Results 68
   4.3. Experimental Setup and procedure 72
   4.4. Adsorption Experimental Results 74
   4.5. Discussion and extensions 79
   4.6. Summary 80
5. Conclusions and Future Work 83
   5.1. Conclusions 83
   5.2. Future Work 84
   5.3. Final Remarks 86

Bibliography 87
Appendix 93
COMSOL model to evaluate axially symmetric assumption of unit cell 93
Cyclical Stability 95
Modeling Straight Channel Pores 95

List of Figures

Figure 1. Graphical depiction of areas expected to see increases in two metrics of water scarcity: Water Crowding Index (WCI) and Water Stress Index (WSI), by 2050 according to recent global climate models [2]. 17
Figure 2. Sankey diagram breaking down energy consumption by industry [4]. 18
Figure 3. Potential technical solutions across the low to middle range waste heat sources [7]. 19
Figure 4. Water molecules, shown as red dots, collecting inside of MIL-101, decreasing in density as temperature increases. The physical phenomena can be described using isotherms and the impact of functional groups can be seen in shifting the isotherm [25]. 20
Figure 5. Increase in number of publications about metal-organic framework composites b)Number of metal-organic framework related publications [27]. 21
Figure 6. a) Silica gel dual-bed prototype installed in the back of the Fiat for testing. b) CAD of the final device design complete with the evaporator and condenser. c) The working schematic demonstrating the fluid lines for circulating waste heat and cooling the cabin [17]. 23
Figure 7. a) Schematic of the ABU and ECU inside of the vacuum enclosure. b) Adsorption process with operating temperatures for this work. c) Desorption process with operating temperatures in this work. 27
Figure 8. Adsorption cooling thermodynamic cycle, where $Q12$ and $Q23$ are the energy added from the waste heat source during isosteric heating and desorption respectively. $Q34$ and $Q41$ are the heat rejected during cooling of the ABU and the adsorption enthalpy released during adsorption [37]. 27
Figure 9. Equilibrium, thermal, and mass transport considerations for adsorption material selection. 29
Figure 10. Isotherms for AQSOA Z02 in low-grade waste heat regime. Uptake is both a function of RP and the temperature of the adsorbent, so each curve corresponds to a constant temperature process to measure the uptake for a given RP [40]. 29
Figure 11. a) Black squares, red circles, and blue triangles represent the isotherms for KMF-1 at 20, 30, and 40 ℃ respectively. ref. b) Isotherms for various materials. All reference data is at 20 ℃, except Co-CUK-1 at 30 ℃ and CAU-23 at 25 ℃ [41],[42],[43],[44], [45]. These figures come from [38]. 31
Figure 12. a) Uptake potential for Z02 for various adsorption temperatures and desorption temperatures with a vapor source at 5.5 ℃ b) Uptake potential for MOF-801 for various adsorption temperatures and desorption temperatures 5.5 ℃. 33
Figure 13. Mass of Z02 required to achieve 3 kW cooling power for a 200 second adsorption cycle as a function of adsorption temperature and desorption temperature at an evaporation temperature of 5.5 ℃. 33
Figure 14. Predominant ABU design architectures [58]. 35
Figure 15. a) Coated tube design shown with the repeating unit cell for adsorption performance analysis, with idealized adiabatic boundaries shown in red. A spacing of 1.25 D is used, as is industry standard for tube bundles. b) A unit cell of the tube-fin configuration with a pitch distance of 3.5 D, a value selected based on our later analysis. c) The surface area available for coating divided by the volume of the unit cell as a function of tube OD for different designs including an efficiency knockdown. 36
Figure 16. a) Example of a single integrated fin. The dashed line represents the idealized unit fin used for analysis. b) Idealized unit cell with adiabatic and zero mass flux boundary conditions. 39
Figure 17. Design and optimization flow chart for adsorption based cooling system design. 41
Figure 18. Adsorption and desorption flow patterns with the LHS system. The LHS provides cooling during desorption, while the ABU recharges the LHS during adsorption by providing cold circulating water that simultaneously cools the cabin. 44
Figure 19. a) Side and b) Front view schematic of a plate and fin type adsorption bed, indicating key parameters of the physical design that dictate performance. 45

Figure 20. a) SCP with respect to adsorbent mass and volume as a function of S/D for different fin thicknesses. b) Fin resistance as a function of S/D and fin thickness. 47
Figure 21. a) Total device volume and mass as a function of S/D. Fin thicknesses vary from 50 μm to 150 μm. b) Normalized pumping power as a function of S/D. 47
Figure 22. Pumping power and device mass as a function of S/D and fin thickness. 49
Figure 23. Effective diffusivity as a function of porosity on left axis, assuming a crystal radius of 2.5 micrometers. On the right axis is the characteristic diffusive time scale for a 2 mm adsorbent coating as a function of porosity. 50
Figure 24. The normalized power curve for a 1 mm adsorbent coating, S/D =3, with 200 seconds for adsorption and desorption. Also shown are the characteristic time of adsorption for this design for optimal performance, and the time for 90% power saturation. 51
Figure 25. Spatial variations in uptake as a function of porosity and coating thickness from COMSOL model. The top figures have an adsorbent coating of 2 mm, and the bottom are 0.5 mm. 52
Figure 26. Uptake difference as a function of porosity shown with the packing density of adsorbent per unit volume. Outputs are shown for various adsorbent coating thicknesses. 54
Figure 27. Absolute adsorbed water density in kg of water per volume of adsorbent as a function of porosity. Outputs are shown for various adsorbent coating thicknesses. 54
Figure 28. a) Total device mass in kg as a function of porosity. Values are shown for various adsorption coating thicknesses. b) Device volume as a function of porosity. 55
Figure 29. a) Pressure drop and device mass shown with the Pareto front in the black dashed line from simulation results. b) Volume and device mass shown with the Pareto front in the black dashed line from simulation results. Each dot represents a simulated design. 58
Figure 30. Final design of the 1:10 scaled down prototype, complete with seventy-five fins, and three 5 mm tubes. 59
Figure 31. a) Copper foam and copper fins cut to size for the final device. b) Copper fins aligned show precise positional location of flanges ensures sufficient tolerance for tube expansion process. 60
Figure 32. a) Fully submerged evaporator coil that must overcome the thermal mass of the water layer before providing cooling to the coolant. b) Schematic of proposed thin film evaporator in a serpentine path. c) Detailed view of working principal of the ECU. *Figures b) and c) were created by Dr. Xiangyu Li and adapted for this work. 61
Figure 33. Impact of a/b ratio on the total required length of ECU tubing and the % pumping power required. This ratio compares the required pumping power to the cooling load for a constant flow rate and starting tube of 0.25” for the prototype. 63
Figure 34. Pareto front for the prototype ECU in terms of pumping power and volume, with a pumping power cutoff value in green. 64
Figure 35. Comparison of the footprint and thermal mass of serpentine versus tiered hairpin design. 65
Figure 36. a) Tiered hairpin ECU design, shown with water trays for reference. b) Final ABU and ECU prototypes shown in the 16"x16"x16" vacuum chamber for future testing. 65
Figure 37. Rendering of the ABU and ECU prototypes currently under fabrication. 66
Figure 38. a) SEM image of the immersion dried sample. b) Zoomed in SEM of a single pore of the same sample shown in a). 69
Figure 39. a) BACT sample using 150 ℃, with clear coalesced vapor pockets resulting in large sections of sparsely coated copper foam and clogged pores elsewhere. b) Magnified view of sample revealing limited adsorbent crystals coating the foam in the coalesced vapor pocket. 71
Figure 40. Different adsorbent coating structures as a function of temperature used for BACT coatings, where the blue circles represent adsorbent crystal alignment. Low temperatures result in a random porous

media, and high temperatures results in large vapor pockets that escape through sides rather than the top of the coating, as well as scaffolding that forms at the bottom. The red bar represents the hot plate..... 71
Figure 41. a) SEM image of BACT sample. b) Magnified SEM of a single pore of the same sample in a). 72
Figure 42. Schematic of experimental setup to test the performance of fabricated adsorbent samples..... 73
Figure 43. a) Heat flux and change in temperature of the fluid over the course of the 200 second experiment. b) Pressure measured during the experiment using the Baratron pressure transducer. This was a 1 mm sample tested at 38 ℃ with a porosity of 0.6. 75
Figure 44. Uptake curve as a function of time for three experimental runs with 1 mm sample at 38 ℃ and 0.6 porosity. The error bars are shown for the run average, and the green line represents the reference model. 75
Figure 45. Average Power and SCP of sample as a function of time. Shorter adsorption periods result in higher performance metrics. In black is a reference point from recent work from Sapienza et al. as a literature leading benchmark for Z02 at these conditions[56]. 76
Figure 46. Uptake for optimized BACT sample compared against the straight channel limit model for a 2 mm sample at 38 ℃, 0.68 porosity. Also shown is a 2 mm ID sample tested at 38 ℃, 0.63 porosity compared against the random porous model..... 78
Figure 47. a) Ratio of the mass transfer convective resistance of water vapor to the mass transfer conductive resistance for a coating height of 1 mm. A $Bi < 0.1$ indicates that the pore can be modeled as having a constant concentration through the height of the pore. b) Resistance ratio for a 2 mm coating height. 79
Figure 48. a) Characteristic time to adsorb $1 - 1e\Delta w$ for traditional ID and BACT samples. b) Collected water in kg/m^2 of device as a function of adsorbent thickness for ID and BACT samples. 85
Figure 49. a) 3D model of adsorption bed unit cell. b) 2D model of unit cell with D_eff scaled to match the square unit cell area..... 94
Figure 50. Comparison of cooling power curves for 3D and 2D COMSOL models..... 94
Figure 51. Adsorption and desorption cycle with 1mm sample at 38 ℃ with a porosity of 0.6. This is measurement of the heat flux measured during the experiment. The initial curve is first curve after sitting in vacuum for 30 min, and the second and third peaks represent steady state. Dashed black lines are shown as a reference to highlight the repeatability of each cycle. 95
Figure 52. a) Boundary conditions for the straight channel pore model. b) The uptake at 75 seconds for a 1mm tall, 20 micrometer adsorbent coating shows a very small spatial dependence due to the small length scale of the coating..... 96

Chapter 1

1. Introduction

1.1. MOTIVATION

Climate change threatens every area of the economy and everyday life. Analysis shows that the results of climate change will disproportionally afflict people from less developed countries [1]- threatening even the most basic of human necessities for clean, reliable access to potable water [2]. Today, it is estimated that 2.4 billion people currently live in water stressed regions, where the withdrawal rate is significantly greater than the refresh rate, and that number is expected to grow to half of the global population by 2025 according to the World Health Organization [3]. The 2050 predictions of Gosling *et al.*. show that areas representing a majority of the world's population will only increase in water scarcity, impacting global health, agriculture, and many other aspects essential to the health, prosperity, and progress of mankind [2]. As such, strategic efforts must be made across academia, industry, and the public sector to combat the emission of products with global warming potential. Additionally, researchers must find a way to help decentralize water production as countries hit the hardest by this impact often lack the infrastructure in place to meet their water needs. Atmospheric water harvesting is one such solution and will be addressed at the end of this work due to the similarity of its governing principles as another adsorption-based process.

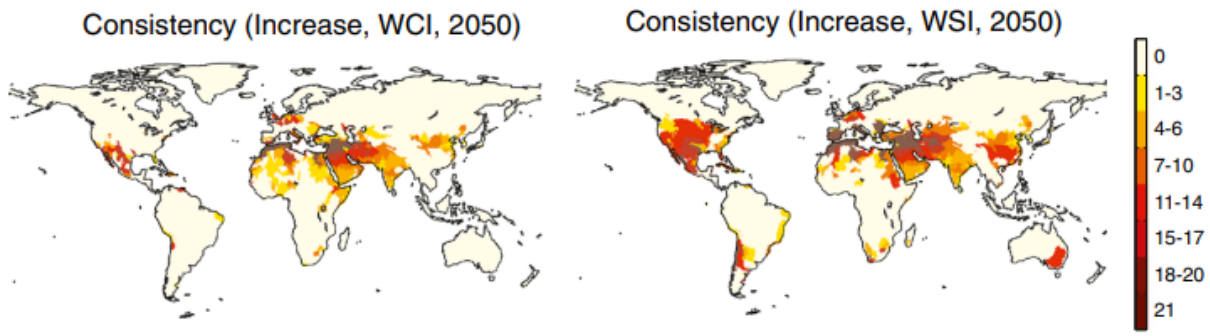

Figure 1. Graphical depiction of areas expected to see increases in two metrics of water scarcity: Water Crowding Index (WCI) and Water Stress Index (WSI), by 2050 according to recent global climate models [2].

1.2. ENERGY UTILIZATION AND EMISSIONS

Emissions with global warming potential, such as CO_2, NO_x, and the leakage of refrigerants found in air conditioning systems, are all related to mankind's increased activity. As the global population grows and the demand for electricity and building and heating follows, decarbonizing electricity generation will not be enough. In fact, examining the Sankey diagram from Lawrence Livermore National Laboratory reveals that roughly two-thirds of energy produced is rejected as heat to the environment [4]. This is an incredible amount of wasted energy, with approximately two-thirds of that wasted energy coming in equal parts from the electricity generation sector and the transportation sector, and a fifth from the industrial sector. Creating more efficient processes that involve waste heat recovery in the electricity generation, industrial, and transportation sectors will be key in reducing the global carbon footprint by simply reducing the demand in the first place. The cheapest, cleanest Joule is the one that never needs to be created, and waste heat recovery for storage or direct waste heat driven systems help reduce the demand for more energy.

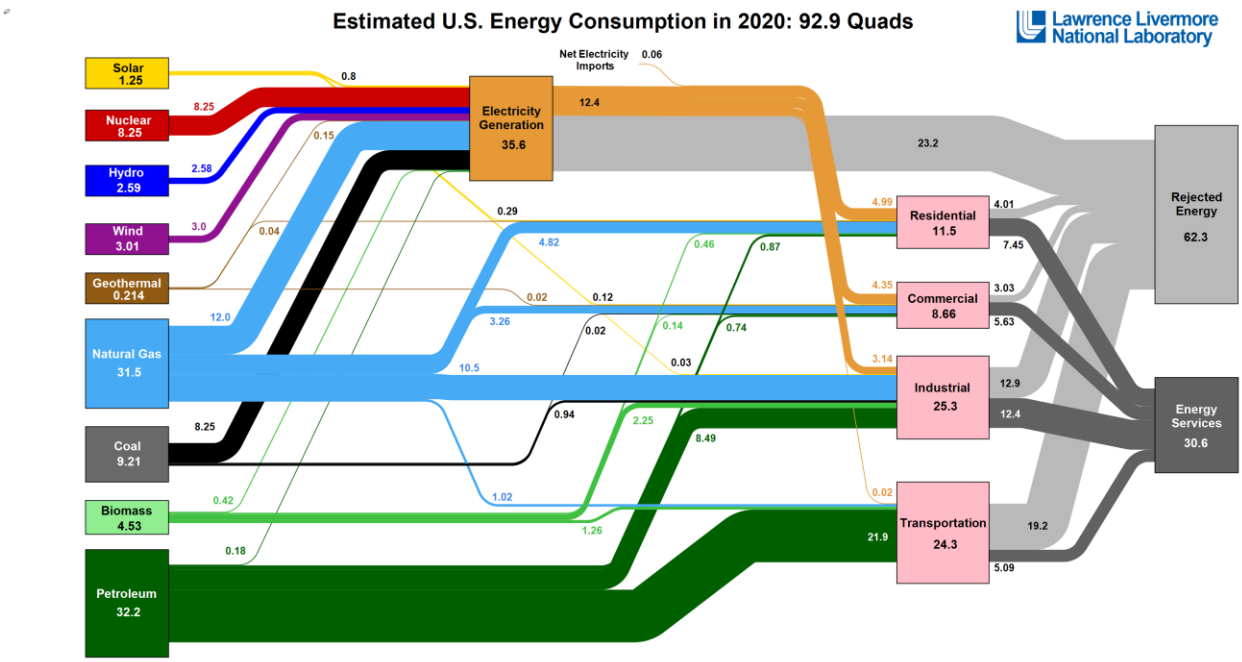

Figure 2. Sankey diagram breaking down energy consumption by industry [4].

To underscore the importance of the efficient generation and management of heat, it should be noted that the world economy runs on heat, as 90% of all energy produced is used for some form of temperature manipulating process [5]. It is clear from the International Energy Agency (IEA) reports that focusing on utilizing waste heat across the spectrum, from >1000 ℃ in heavy industrial processes to <90 ℃ in internal combustion engine coolant, is the most impactful approach to combat climate change [6]. There exists a plethora of solutions for high temperature waste heat, as the available exergy has attracted much attention for engineers and scientists due to the inherent efficiency of thermal processes with a high temperature source, as can be found in the steel or cement industries. While promising solutions exist to leverage high temperature waste heat for power cycles and recycling the heat for other industrial processes, the possibilities for utilizing that waste heat decrease as the available hot side temperature of a system decreases. Waste heat recovery processes are often limited by the ideal Carnot efficiency (Eq. (1)), and it is very challenging to efficiently utilize waste heat below 200 ℃ as the hot side temperature T_h when the cold side (ambient conditions) temperature T_c is 25 ℃.

$$\eta_{Carnot} = 1 - \frac{T_c}{T_h} \tag{1}$$

Even though systems aimed at utilizing these low grade waste heat sources suffer from low entropic efficiencies as classical Carnot efficiency shows, these low grade waste heat categories make up more than 66% percent of all total rejected heat [7]. Consequentially it is the most important area to develop and perfect new technologies to leverage it in the coming critical decades to combat climate change, and includes the considerably energy intensive space heating and cooling market. This includes climate control in buildings and automobiles, which often use high global warming potential (GWP) refrigerants that have anywhere from 100-10,000 times more GWP than CO_2 and is the topic of an increasing number of policy efforts. If left unabated, the leakage of these refrigerants could cause as much as 10 to 50% of all global warming by 2050 [8],[9].

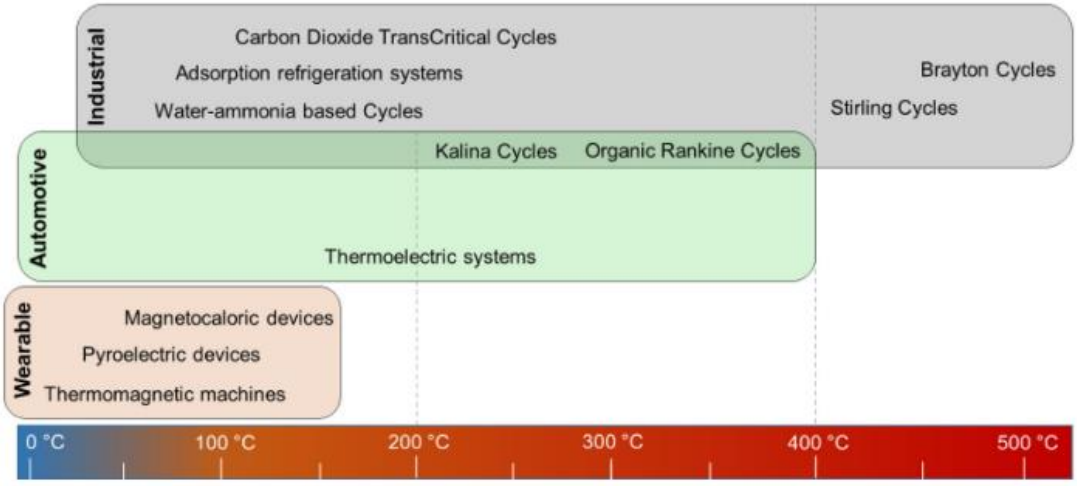

Figure 3. Potential technical solutions across the low to middle range waste heat sources [7].

In this work, we propose a solution to move adsorption refrigeration cycles into the space cooling market, including automotive climate control, enabled by the development of key material developments. This will help capitalize on and reduce the 33% of global wasted energy in the world in transportation, while simultaneously offering a refrigerant free solution for mobile and building heating and cooling needs.

1.3. ADSORPTION AND ADSORPTION MATERIALS

Adsorption is the key phenomena that enables various key technologies, such as carbon capture, atmospheric water harvesting, and adsorption driven cooling. Adsorption is the process of a molecule bonding to a surface by physical bonds (physisorption) or chemical bonds (chemisorption)[10]. As such, the ability for a molecule to bind to a surface depends on the surface area of the material, and the amount of volume that is available inside of that material. Selectivity, or the affinity for a particular molecule, such

as water, also determine how much of that particular molecule would be able to attach to that surface in the presence of other molecules. As such, adsorbents are designed specifically around a particular adsorbate, or the molecule to be adsorbed, which are referred to together as working pairs. A majority of the work done in this space has focused on an the broad class of zeolite materials, such as zeolite 13X and the widely commercially available AQSOA family from Mitsubishi [11]–[15], silica gels [16]–[20], with water, ammonia, or ethanol as the adsorbate [20]–[23]. These materials are relatively inexpensive, readily available, and most importantly hydrothermally stable. However, they do not have anywhere near the same raw working potential of newly developed metal organic frameworks (MOFs).

MOFs have been the focus of extensive work in the material science community, as it is a material framework that offers countless combinations to tailor the surface area, volume, and selectivity of the material. They have a crystalline structure composed of a metal-containing units called secondary building units (SBUs) bound to an organic ligand through reticular synthesis, and often created with functional groups to tailor their affinity towards a particular molecule [24].

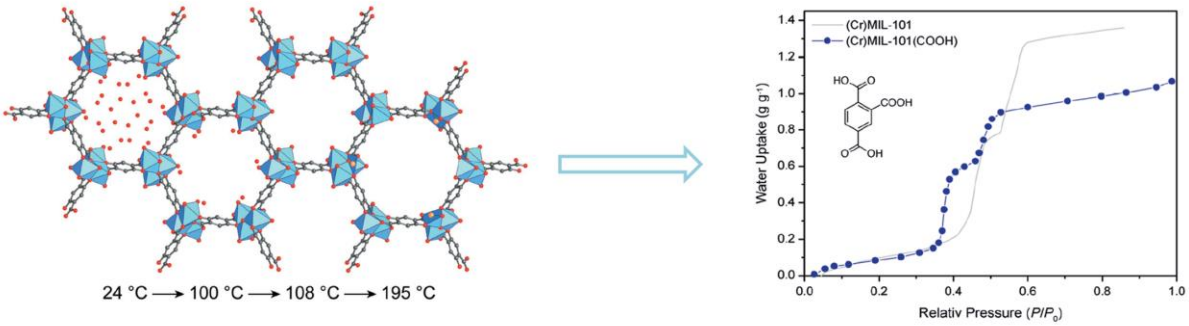

Figure 4. Water molecules, shown as red dots, collecting inside of MIL-101, decreasing in density as temperature increases. The physical phenomena can be described using isotherms and the impact of functional groups can be seen in shifting the isotherm [25].

Figure 4 shows the structure of the popular (Cr)MIL-101 MOF used with water as a working pair. The grey structures represent the organic ligands to bind the blue SBUs built around chromium metal ions. As the temperature increases, the difference between the vapor pressure inside of the pores and outside of the pores overcomes the affinity for the physically bonded pores first, then the chemically bonded water at higher temperatures. It is very hard to remove all of the water due to the strong ionic bond that forms at the metal sites. This behavior is captured in the isotherm, shown on the right, which describes how much water can be adsorbed at a given temperature and ambient vapor pressure. This will be covered in more depth later, but these charts are essential for engineers designing systems to understand how a material would perform for a given set of operational conditions, and can be tailored to some degree via post-

synthetic functionalization. This is illustrated in the shift from the dark blue baseline isotherm to the light grey isotherm with the addition of carboxylic acid groups.

With key adsorption technologies like adsorption based cooling, atmospheric water harvesting, and carbon capture increasing in technological readiness levels (TRL), the scientific community has been exponentially increasing their efforts to create materials to improve the performance of these technologies [26], [27]. This includes the production of MOF-composites to help with the thermal conductivity, adhesion, and synergy for enhanced uptake for adsorptive properties with mixed-MOF polymer matrices and the addition of thermally conductive particles or CNTs [28]–[33].

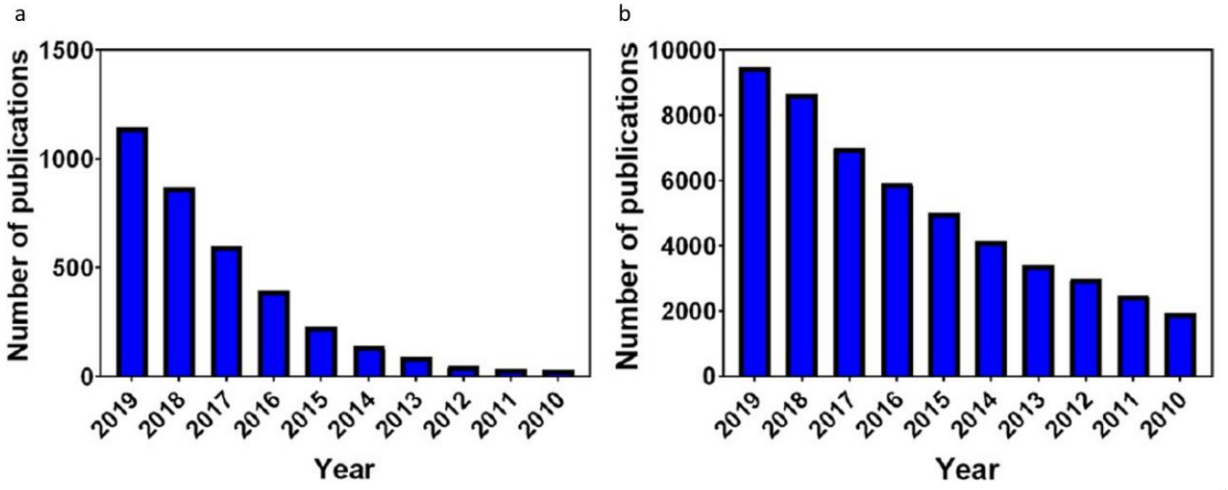

Figure 5. Increase in number of publications about metal-organic framework composites b)Number of metal-organic framework related publications [27].

Despite the rise in available materials to choose from with the advent of MOFs, MOFs have yet to be implemented into a commercial cooling solution due to their high costs and intensive fabrication processes, as well as poor cyclical stability resulting in degraded performance over time. Due to their lack of commercial feasibility, MOFs were not tested in this body of work so the focus could be on most near term, practical solutions for adsorption cooling for automobiles. Further, there are very few MOFs that have a significant working potential in the range of conditions used in the automotive industry. AQSOA Z02, a commercially available zeolite, is still the best material for this range as will be discussed later. As such, adsorption based cooling systems are predominately based on zeolites and silica gels to date, but efforts to make MOFs more practical offer hope for the performance benefits they offer at commercial scale in the future [34]. We aim to help bridge the gap in material development and practical application by informing the material scientist of the system level considerations that should be made for the

integration of their new materials, as well as the thermo-fluidic design engineer as to how material characteristics should guide their design.

1.4. ADSOPRTION COOLING FOR AUTOMOBILES

There has been considerable progress in the testing of adsorption systems for adsorption-based cooling using more established materials, such as zeolites and silica gel. For example, Mola *et al.* created a full prototype that was installed in the trunk of a Fiat Grande Punto, as seen in Figure 6 [17].

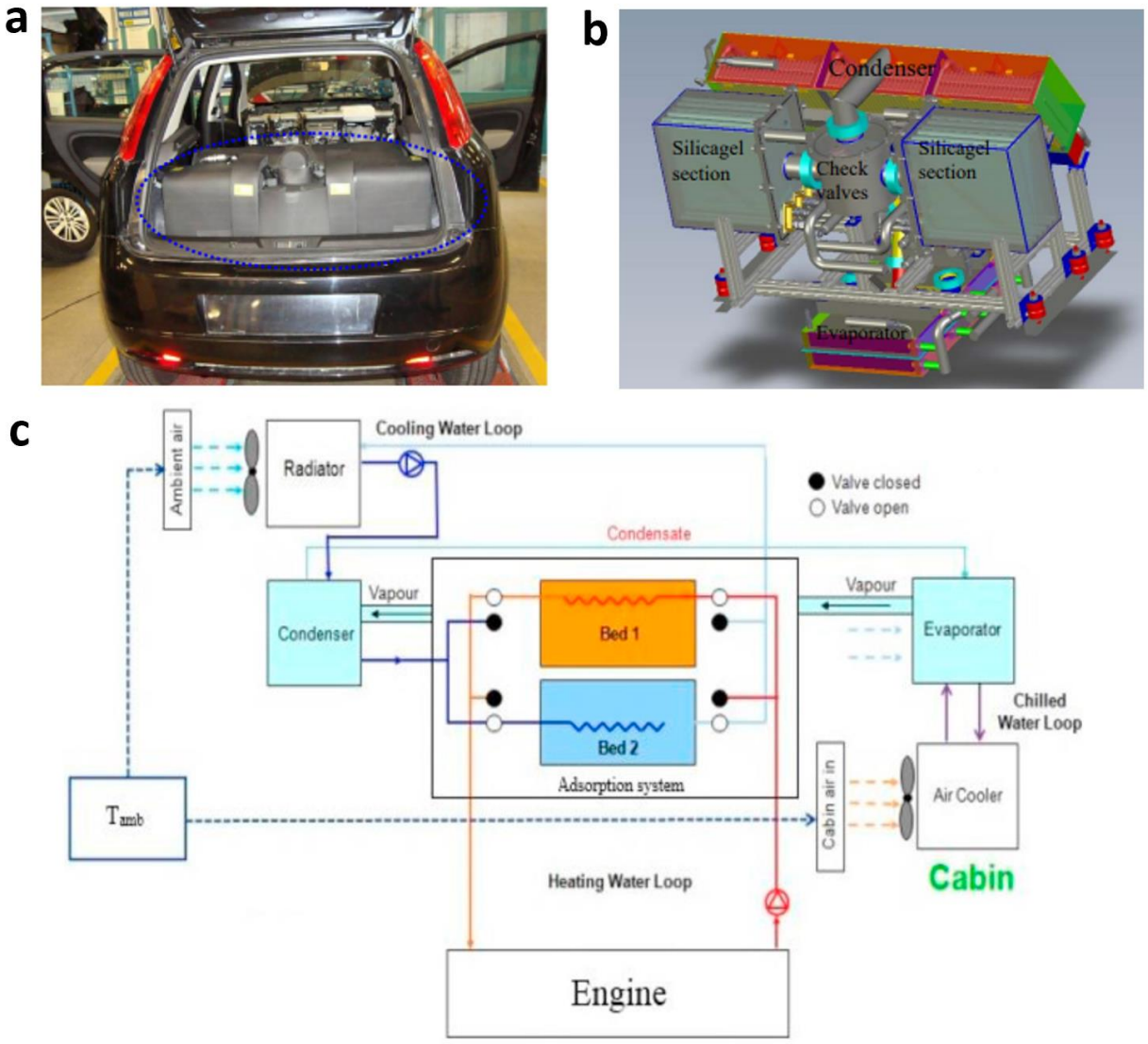

Figure 6. a) Silica gel dual-bed prototype installed in the back of the Fiat for testing. b) CAD of the final device design complete with the evaporator and condenser. c) The working schematic demonstrating the fluid lines for circulating waste heat and cooling the cabin [17]**.**

Despite the impressive engineering feat of creating this device, the prototype weight was 86 kg, making it much too heavy for commercial application. From the design, it is clear that the evaporator and condenser take up a significant amount of volume, and the valves used to route between them also take up considerable space. As each section is separated and under vacuum, they require a significant amount of mass to stay structurally sound. With the exception of this work, a majority of the sorption cooling community has mostly focused on the application of new materials to improve the performance and leaves engineers within industry with the difficult task of designing at the system level. As such, we aim to bridge the divide in the work by exploring in this thesis, moving from the methods of material deposition and binding, all the way

up to suggesting a new systems level design to reduce mass and volume to acceptable industry levels. Constraints for the system were informed directly by our collaboration with Ford to avoid this disconnect commonly found in the literature.

1.5. THESIS OBJECTIVES AND OUTLINE

The objective of this thesis is to present a convenient, rational set of design guidelines and considerations to aid in the acceleration of adsorption-based devices out of the lab and into the field for adsorption-based cooling. These guidelines will be shown alongside a practical example- a 1:10 scale prototype of an adsorption driven cooling system to replace vapor compression cooling systems currently found in automobiles, leveraging the waste heat extracted from the engine coolant. By optimizing at every length scale, from micrometer level vapor channels and binder integration, to system level mass, volume, and pressure drop calculations utilizing a multi-objective optimization framework, we present literature leading values in subcomponent characterization and projected system level performance.

First, we will review the current state of the art in sorption climate control solutions and introduce the governing equations that describe the adsorption-based cooling cycle that will be used on consequent modeling efforts. We also introduce thorough design guidelines for material selection, design architectures, and modeling approaches to assist in the design of portable climate control solutions.

Second, with an understanding of the governing equations and material constraints, we will explore system level design tradeoffs and introduce a formal multi-objective optimization approach that we recommend be adopted as the standard for future work to ensure designs are compared holistically.

Third, we will discuss characterization techniques used for subcomponent testing to validate our models and predictions, as well as introduce a novel manufacturing method to reduce time, material waste, and enhance mass transfer kinetics for a significant improvement over previous manufacturing methods.

In the final chapter, we will review the lessons learned from this work and describe the next steps that we think are essential to translating adsorption technology out of the lab and into real devices for adsorption driven cooling and other adsorption-based systems, such as atmospheric water harvesting.

Chapter 2

2. Modeling of Waste Heat Driven Adsorption Cooling for Automotive Climate Control

In this chapter, we present a review of existing designs and modeling approaches for automotive climate control. While there are also solutions for higher temperature exhaust sources for diesel vehicles with exhaust ranging from 150 - 450 ℃ [35], we will focus on applications with a waste heat source of less than 100 ℃, which is representative of the engine coolant temperature of a common internal combustion engine (ICE)[36]. This is a larger portion of the market, and such small temperature differences (40-60 ℃) between the waste heat and ambient conditions create some very strict challenges. The nomenclature to compare designs will be established, and recommendations will be made and utilized in work moving forward to more effectively compare potential designs. This nomenclature will then be summarized and a design flowchart will be introduced at the end of the chapter to summarize the process in hopes to aid future developments.

2.1. COOLING CYCLES

First, we will discuss the thermodynamics of the adsorption driven cooling (ADC) cycle. These cycles are fairly simple. In this work we will refer to an adsorption bed unit (ABU) that is entirely desorbed as fully charged, as this state has the most potential to adsorb water and thus drive the most cooling via evaporation. Conversely, a fully saturated ABU is discharged, as it has no remaining potential to adsorb and thus no cooling potential. Beginning with the charging portion of the cycle, we start with a fully saturated ABU. To charge it, we heat the ABU with fluid directed from the engine that comes in at 90 ℃. As the ABU heats up, the relative pressure in the adsorbent bed increases, and it becomes thermodynamically favorable for the adsorbed water to desorb, as indicated by the material's isotherm. This process absorbs a significant amount of heat equal to the adsorption enthalpy h_{ad} (J/kg water desorbed) plus the sensible heat required to heat up the heat exchanger, and this thermal energy is supplied via the circulating engine coolant. The desorbed water then condenses on the evaporator-condenser unit (ECU) that has ambient temperature fluid running through it to remove the latent heat of the condensed water on its surface. Once this process is complete, the ABU is charged and ready to drive cooling. The circulating fluid is switched to the ambient line to keep it cool, now releasing h_{ad} as it adsorbs, requiring sufficient flow to maintain this temperature and the adsorption rate that is very temperature dependent. This water is supplied from the surface of the wicking evaporator surface, which in turn cools the cabin coolant. The relevant temperature conditions for

the cycle are defined as follows: the temperature of the ABU during adsorption is the adsorption temperature T_a, and its temperature during desorption is T_d. This working principle can be seen in Figure 7, and the thermodynamic cycle can be seen in Figure 8. The thermodynamic cycle begins with a discharged ABU (1) that undergoes isosteric heating by convective heat transfer from the engine coolant, while the condensing unit increases the pressure of water vapor in the chamber to the pressure exerted at its operating temperature T_{cond}. Next (2), the material begins to desorb while the bed continues to be heated to overcome the enthalpy required to desorb water, until it is fully charged. Once desorption is complete (3), the ABU is cooled and then will start adsorbing as the evaporator supplies vapor at a pressure of p_e (4). The ABU is continuously cooled to reject the enthalpy of adsorption until fully discharged, and the cycle repeats. In most configurations, the system consists of two identical ABU's that alternate between adsorbing and desorbing to supply continuous power.

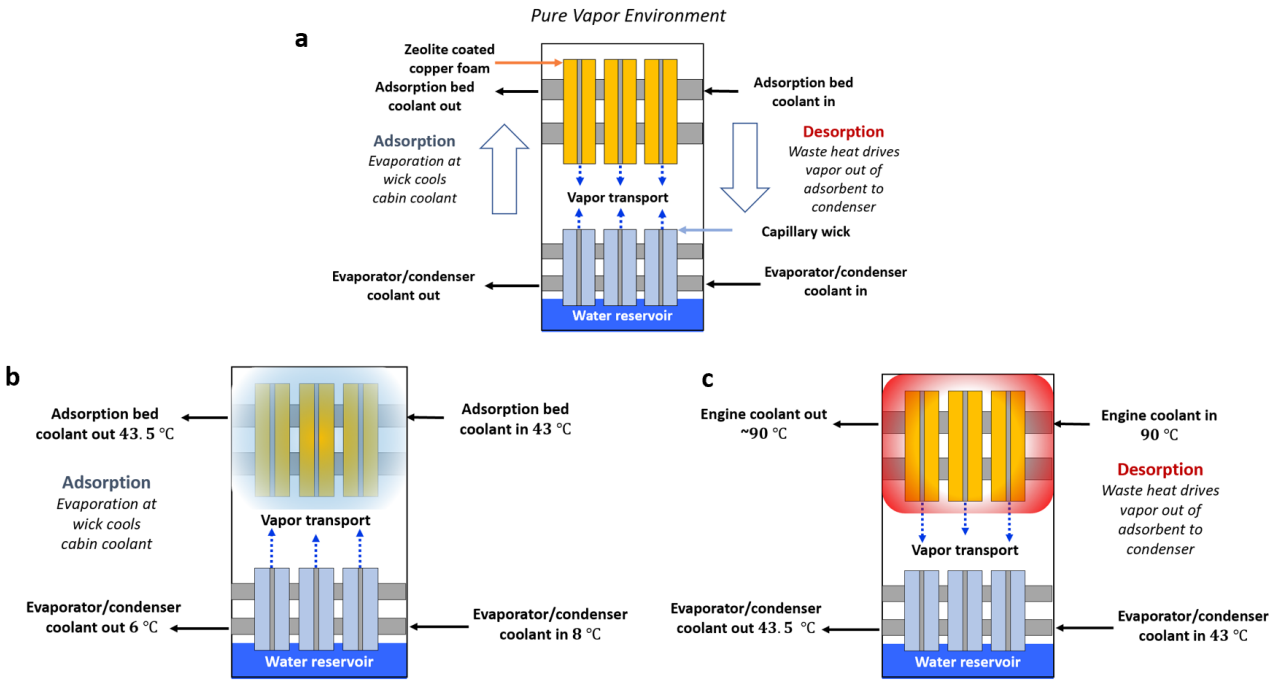

Figure 7. a) Schematic of the ABU and ECU inside of the vacuum enclosure. b) Adsorption process with operating temperatures for this work. c) Desorption process with operating temperatures in this work.

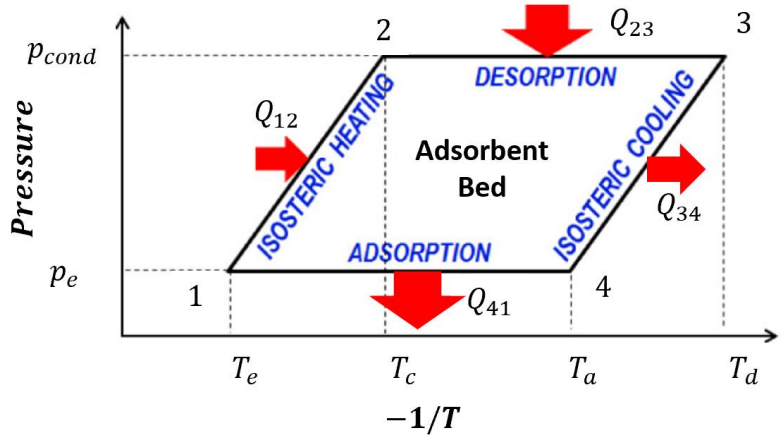

Figure 8. Adsorption cooling thermodynamic cycle, where Q_{12} and Q_{23} are the energy added from the waste heat source during isosteric heating and desorption respectively. Q_{34} and Q_{41} are the heat rejected during cooling of the ABU and the adsorption enthalpy released during adsorption [37].

The evaporator temperature at this evaporating surface, T_e, and the condenser temperature T_{cond} also have a significant impact on performance, as high evaporator temperatures provide higher pressures of water vapor available to be adsorbed, but also reduces the temperature difference between the cabin coolant and the air it is trying to cool. High condenser temperatures, directly limited by the ambient temperature

conditions, create high vapor pressures on the surface and reduce the amount of adsorbate that can be desorbed from the ABU before equilibrium is reached.

In literature, various operating temperatures are used, where T_e ranges from 5 to 20 ℃, T_a from $20-40$ ℃, T_d from $60-110$ ℃, and T_{cond} from $20-40$ ℃ [38]. Given the exponential nature of the vapor pressure of water with increasing temperature, these conditions make a large difference in the performance of the device, and care should be taken when comparing device performance. From our experience with industry, automotive cooling specifically requires testing of the air-conditioning system up to 43 ℃ [39], and while there is only a 3 ℃ difference from the commonly used 40 ℃, it can often make the difference between a highly effective design and a poor design based upon the chosen adsorbent-adsorbate working pair. Choice of this working pair requires careful consideration, and will be reviewed in the next section.

2.2. MATERIAL REVIEW

In order to select the appropriate material for an adsorption-based cooling system, one should start with defining the given set of conditions previously discussed to determine the relative pressure RP at adsorption and desorption, RP_a and RP_d, respectively. The relative pressure that the adsorption coating will be operating at can be determined with Eq (2),

$$RP = \frac{P_{Sat}(T_e)}{P_{sat}(T_{ads})} \tag{2}$$

The saturation pressure P_{sat} of the adsorbate in the working pair can be given as a function of temperature. Here, T_{ads} represents the temperature of the adsorbent cyrstals, which for a well-designed system will be close to T_a. However, adsorption is a highly transient process, so the temperature of the adsorbent should always be computed spatially at each time step in a finite element model to account for variations. The resulting RP can be considered as the driving force, as higher relative pressures will result in higher uptakes for a given material.

With these conditions defined, it is possible to quickly survey the available materials in literature to determine the best possible candidates from an equilibrium condition. There are some key material properties that are functions of the operating conditions listed above, as indicated in Figure 9.

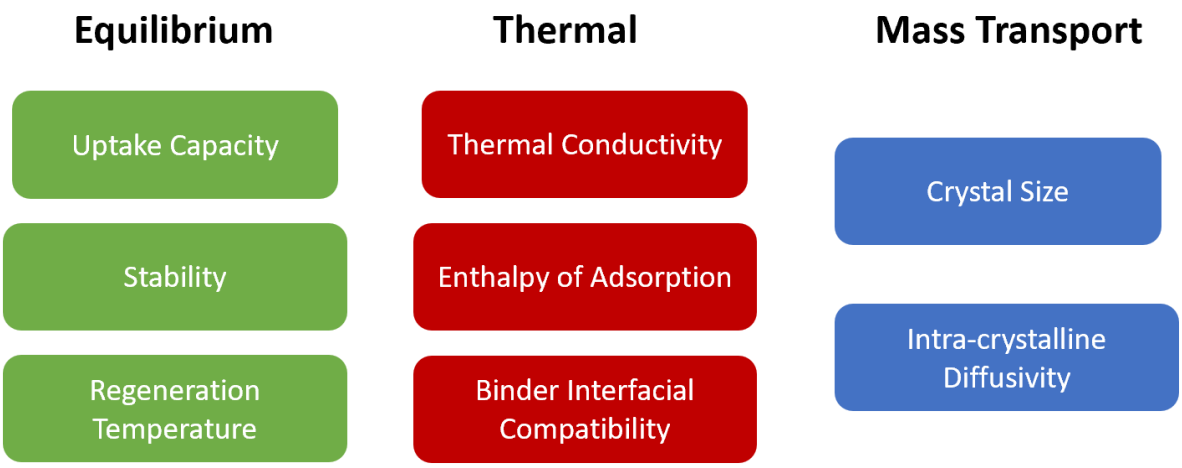

Figure 9. Equilibrium, thermal, and mass transport considerations for adsorption material selection.

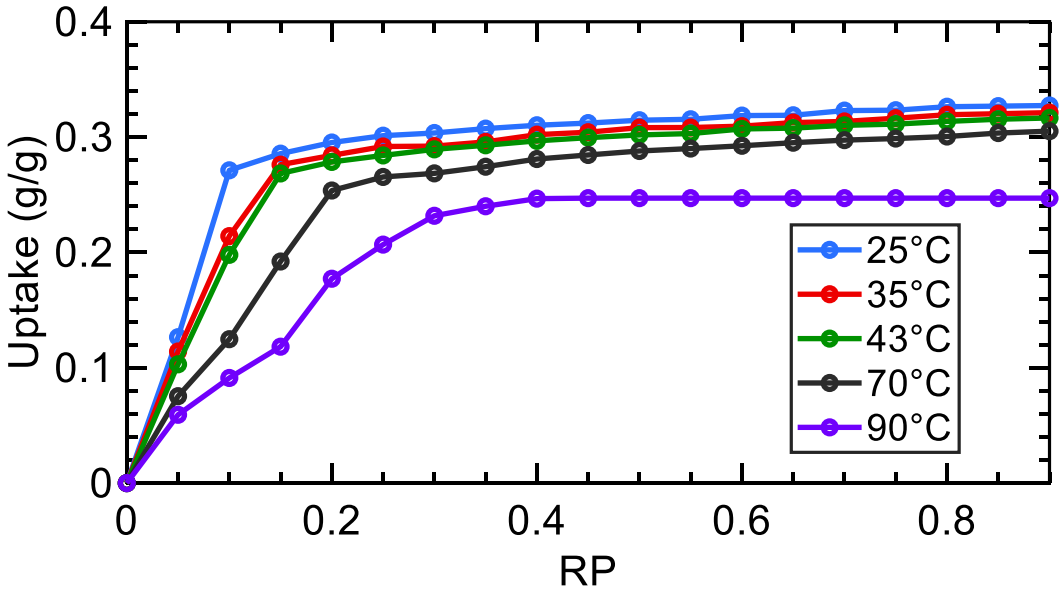

Figure 10. Isotherms for AQSOA Z02 in low-grade waste heat regime. Uptake is both a function of RP and the temperature of the adsorbent, so each curve corresponds to a constant temperature process to measure the uptake for a given RP [40].

Equilibrium conditions, such as the maximum amount of adsorbate that can be adsorbed at equilibrium conditions can be determined by examining or characterizing the isotherms of the adsorbent material, shown in Figure 10. An isotherm refers to the uptake as a function of the relative pressure of the adsorbate surrounding the adsorbent coating for a given temperature T_a. The isotherm of AQSOA Z02 (sometimes referred to as SAPO-34), a commercially available zeolite designed for cooling cycles with low regeneration temperatures, can be seen to exhibit high uptake at very low RP as is characteristic of materials

with type I isotherms. This is the material selected for this work, as it is one of the only materials capable of adsorbing at such high adsorption temperatures as is required by the automotive industry. Even recent work, such as that of Sapienza *et al.* in the creating of KMF-1 which demonstrates an impressive 'S' shaped (type IV) isotherm with a specifically tailored jump in uptake at an RP range for most ADCs, fails to meet the stringent requirements for portable climate control. In this case, with a $T_a = 43$ ℃, and an evaporator surface temperature of 5.5 ℃, RP is 0.1, resulting in very little uptake potential by any of the materials besides Z02. Further, the RP during desorption with a $T_a = 43$ ℃ is higher than the RP during adsorption at a value of 0.12. As a result, the working capacity at these conditions is a result of the partial derivative of the uptake with respect to the temperature of the adsorbent at a given RP $\frac{\partial w}{\partial T}|_{RP}$. While this is yet to be addressed in literature, it is $\frac{\partial w}{\partial T}|_{RP}$ for small temperature difference adsorption cycles that is the key to making productive adsorption systems. From Figure 10, we can see that this partial derivative is high, especially at low RP. At an RP = 0.1, the uptake of the material drops by two-thirds from 0.28 to 0.09 g/g as the temperature changes from 25 to 90 ℃. We see in Figure 11a that the newly developed KMF-1 material has a negligible $\frac{\partial w}{\partial T}|_{RP=0.1}$. Not only does Z02 have a favorable $\frac{\partial w}{\partial T}|_{RP=0.1}$, but in Figure 11b we see that SAPO-34 (AQSOA Z02) has the highest uptake at this RP as well. Accounting for both the maximum uptake and this newly highlighted derivative that we hope will serve as a more quantitative measurement for what is informally referred to as an isotherm "shift", we confirm that Z02 remains one of the only materials available, despite tremendous efforts to tailor materials for this challenging temperature range. As a comparison point, residential air conditioning systems are able to raise their target evaporator temperature to reflect a 20 degree temperature lift, which considerably increases the RP for the same adsorbent temperature to 0.33. Thus, the challenges to automotive cooling is uniquely constrained and outside of the bounds of most new materials.

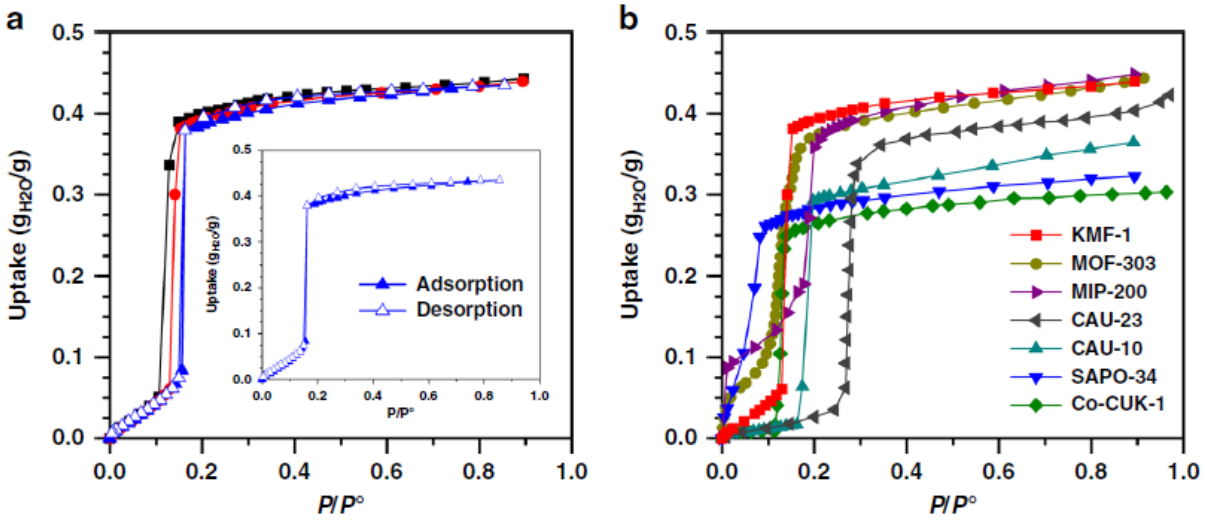

Figure 11. a) Black squares, red circles, and blue triangles represent the isotherms for KMF-1 at 20, 30, and 40 ℃ respectively. ref. b) Isotherms for various materials. All reference data is at 20 ℃, except Co-CUK-1 at 30 ℃ and CAU-23 at 25 ℃ [41],[42],[43],[44], [45]. These figures come from [38].

Moving to the second point on Figure 9, there are three kinds of stability that need to be considered when selecting a material for an application: mechanical, thermal, and cyclical. Mechanical stability is a large issue in MOFs, where the adsorbate can interact with the adsorbent's metal oxide clusters [42]. This is particularly challenging with water as the adsorbate, as water can irreversibly replace a ligand or form a metal-hydroxide bond and a pronated ligand, resulting in permanent damage and loss of performance [46]. Thermal stability refers to the ability for the material to maintain its performance after exposure to high temperatures, which is favorable for accelerating the desorption process to achieve higher cycle powers. Cyclical stability refers to the ability for the material to fully adsorb and desorb as expected for a given operating condition, which is impacted by the mechanical properties of the material and the characteristic pore size [47], [48], [49]. If the characteristic pore diameter of an adsorbent is less than the critical diameter D_c irreversible capillary condensation can occur resulting in hysteresis in the isotherm and loss of working potential for the material [50], [51]. For a given adsorbate, D_c can be determined as a function of the kinetic diameter σ, the operating temperature T, and the critical temperature of the adsorbate T_c (water is 646 K).

$$D_c = \frac{4\sigma T_c}{T_c - T} \qquad (3)$$

The regeneration temperature is the temperature at which the adsorbent will have a near zero uptake, and is an essential characteristic to determine. With too low of a regeneration temperature, the adsorbent may not be able to adsorb during the adsorption phase. If the regeneration temperature is too high, then the

adsorbent will never be able to release the adsorbate with a temperature swing approach, making it a poor choice for heat pump applications. It should be noted that there is no formal definition found in literature for this characteristic, as whether or not the material will regenerate is highly dependent on the operating condition. To try to create a general guideline, we recommend that for a given adsorption cycle a material is selected such that at the regeneration temperature it only between 10% of its adsorption uptake at RP_d for Aristov optimal cycling dynamics [52] and 34% of its adsorption uptake for a characteristic time scale based cycle. An Aristov based regeneration temperature will create higher peak power but a lower overall peak power, while a characteristic time scale based cycle can lead to higher average power at the cost of shorter cycles times and a higher thermal mass penalty. These time scale values are not specific to adsorption systems but rather general principles found for regulating dynamic systems cycling between two equilibrium points and have been adopted by the field. The optimal solution will depend on the application. For reference, RP_d can range from 30 to 60% for different space cooling applications depending on whether or not the system is a supplement to an existing vapor compression cycle (VCC) or a cascaded adsorption cycle. For automotive based adsorption cooling, $RP_d = 0.1$.

With the operating conditions (RP_a, RP_d and the appropriate operating temperatures), the isotherm, and selected thermodynamic cooling cycle (basic refrigeration cycle, cascaded cycle, etc.) along with the appropriate thermodynamic properties of the adsorbent and adsorbate (enthalpies and specific heats), we will obtain the cooling power/efficiencies for a given mass of adsorbent and operating conditions. We propose the design charts shown in Figure 12,, which we call operation contour maps, be used as a basis for early material selection. The iso-contours represent the uptake difference, or the total amount of water that can be adsorbed and desorbed for a given pressure at the evaporator surface, $\Delta\omega$. By varying T_a and T_d, we can effectively change the relative pressure and thus equilibrium uptake at each point. In this figure, we compare the operation contour maps of Z02 and MOF-801, a popular MOF used in some heat pump applications but mostly atmospheric water harvesting due to its high uptake potential. We show a sample operating point for T_a = 48 ℃ and $T_d = 90$℃ with $T_e = 5.5$ ℃ and $T_{cond} = T_a$. We show this point as green in the Z02 map as it has uptake potential at this point, while there is a negative value for MOF-801 at the red dot. This means it actually adsorbs more during desorption conditions because $\frac{\partial w}{\partial T}|_{RP_d}$ is negligible and $RP_d > RP_a$. These maps could also be adapted to highlight the operating temperatures to fall within the recommended uptake guidelines recommended earlier.

This figure can be taken a step further by multiplying the uptake difference $\Delta\omega(T_a, T_d, RP)$ by the latent heat of water h_{fg}, and dividing by the total cycle time $t_a + t_d$ to get the amount of cooling potential per kg of adsorbent. This is known as the specific cooling power (SCP). Note that $\Delta\omega$ in practice is very dependent

on the design features ensuring sufficient heat and mass transfer, as well as ample time for adsorption and desorption. The kinetics portion of the design considerations chart will be discussed in further detail in section 2.4.

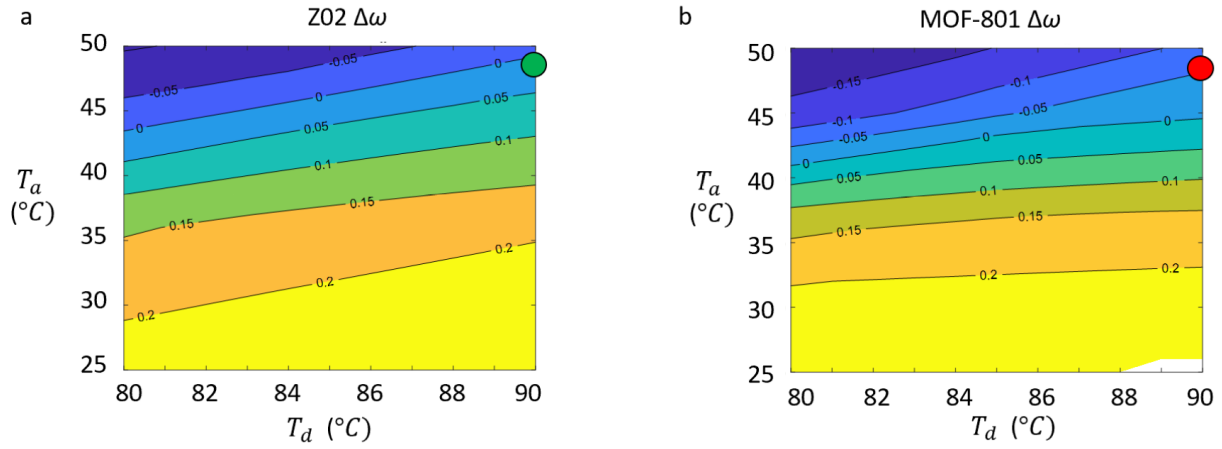

Figure 12. a) Uptake potential for Z02 for various adsorption temperatures and desorption temperatures with a vapor source at 5.5 ℃ b) Uptake potential for MOF-801 for various adsorption temperatures and desorption temperatures 5.5 ℃.

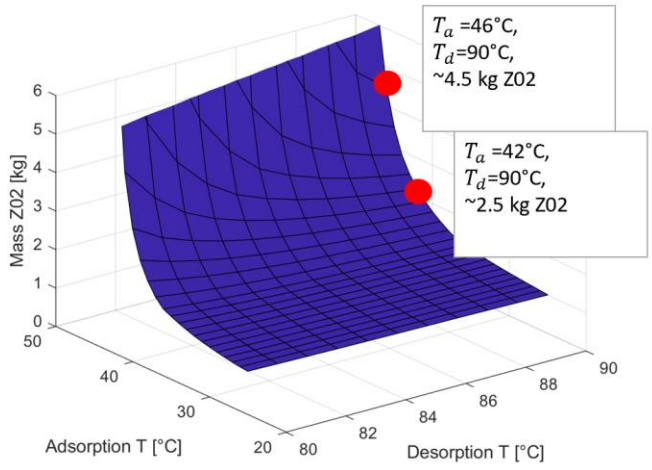

Figure 13. Mass of Z02 required to achieve 3 kW cooling power for a 200 second adsorption cycle as a function of adsorption temperature and desorption temperature at an evaporation temperature of 5. 5 ℃.

Figure 12 serves as method to down select materials to then begin systems level design. One of the first steps of the systems design process is to determine the mass of the adsorbent m_{ads} required to generate the required cooling power $\dot{Q}_c$.

$$m_{ads} = \frac{\dot{Q_c} * t_a}{\Delta\omega * h_{fg}} \quad (4)$$

We can transform Figure 12 into Figure 13 using Eq. (4) to begin to understand system level sensitivities to operation conditions. Figure 13 shows that for increasing T_a from 42 ℃ to 46 ℃, the amount of Z02 required increases by 80%, underscoring the importance of these charts early on in the design cycle to compare against any mass constraints. This shows immediate design implications if no material allows these constraints to be met: a different thermodynamic cycle should be considered, the material search may need to be expanded, or the operating conditions should be adjusted or specific market segments should be excluded. This mass consideration, even in missions that are not mass critical, is important as the adsorbent is often a major cost of the device (especially for MOFs), and thus must be tracked closely for techno-economic modeling.

The thermal conductivity of the adsorbent is also worth considering, as the adsorption enthalpy, or the amount of energy released when a molecule of water is adsorbed, is often greater than the enthalpy of condensation of the adsorbate and the adsorption process can create high temperatures locally without any thermal control [53]. Because adsorbents are inherently very porous, their thermal conductivity suffers as a result (often between 0.05 to 0.25 W/mK)[54]. That is why adsorbents are often integrated with other conductive materials to ensure heat generated during adsorption is quickly dissipated and that the heat generated for desorption can quickly transfer to the adsorbent [28],[55]. As a result, it is important to understand the surface chemistry of the conductive materials and the adsorbent chosen to create an adsorption heat pump as the interface could result in very large thermal resistances and thus limit the kinetics of the process. In many cases, researchers have chosen to pursue *in situ* coating methods that entail growing the adsorbent crystals on the surface of a heat exchanger component's surface, as this leads to very little interfacial resistance [56]. In this work, we chose to use a highly porous copper foam due to its low density and superior thermal performance, creating coatings with an effective thermal conductivity of 4 W/mK. This will be discussed in more detail in the next chapter.

2.3. DESIGN ARCHITECTURES

Adsorption bed designs have taken many shapes and sizes, and depend upon the working pair. In this work, we focus specifically on solid adsorbents and the various approaches taken to coat heat exchangers for optimal performance. The designs are generally plate-finned, where fluid flows between finned plates to

enhance surface are, finned tube as we use in this work, fin plates, or serpentine flat pipes [57]. The most common by far is the finned tube, as it allows for the easiest fabrication in the case of directly dip coating the fins to coat them with adsorbent.

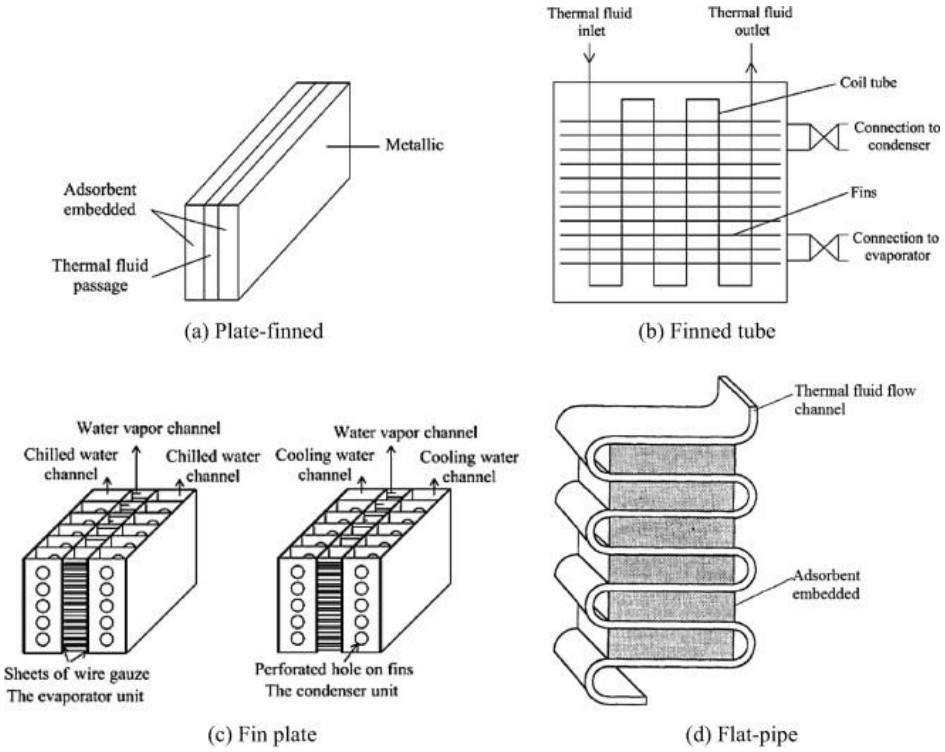

Figure 14. Predominant ABU design architectures [58]**.**

In addition to these designs, there has been a lot of traction surrounding thin coatings of adsorbent directly on top of circular tubes or tubes with annular fins [59]. These designs all have their advantages depending on the application. For example, if a short burst of heating or cooling is required, the device should have thin coatings directly on the tubes, as this will minimize the thermal resistance that is limiting for short time scales. Long, steady heating/cooling periods favor flat pipe or finned tube designs as they enable thicker coatings and more steady power, typically limited by mass transfer. However, literature has not provided any guidance as how to design for these different objectives. Often times, literature will only report the SCP with respect to the mass of the adsorbent (SCP_{ads}). While this is useful for comparing materials, it is a convoluted metric to use as it does not accurately describe the mass and volume efficiency of the entire system. With the mass of the metal of the heat exchanger varying from 3 to 10 times the adsorbent mass for a given design, the SCP_{ads} can be misleading and even favor poor device designs, as is the case with directly coated copper tubes [36]. Especially when considering the implications of the volume, the coated circular tube design will always fall short of the tube-fin design. Figure 15a shows in the coated tube design in a bundle with a pitch distance of $1.25D$ as is industry standard next to the fin and tube design in Figure

15b with a spacing of $3.5D$. In comparing these two designs, we see that the ratio of surface area of exposed adsorbent coating to the volume of the unit cell is 2-3 times smaller for coated tubes than the fin and tube design. Even applying a 20% performance reduction to the tube-fin design, which is conservative to drive home the point, the tube design is much less volume efficient than the tube-fin design. While the tube design could easily result in high SCP_{ads} due to its highly efficient heat transfer, it is not practical at a systems level as indicated by the poor SA/Vol ratio.

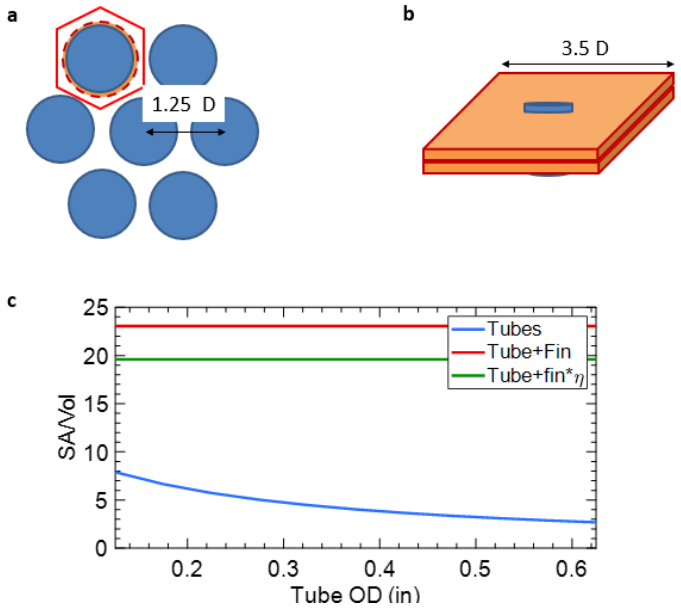

Figure 15. a) Coated tube design shown with the repeating unit cell for adsorption performance analysis, with idealized adiabatic boundaries shown in red. A spacing of 1.25 D is used, as is industry standard for tube bundles. b) A unit cell of the tube-fin configuration with a pitch distance of 3.5 D, a value selected based on our later analysis. c) The surface area available for coating divided by the volume of the unit cell as a function of tube OD for different designs including an efficiency knockdown.

Device level performance will be examined more through this work to highlight the difference between reporting in academic papers and what is required to produce designs that consider practical limitations, reducing the friction of translating this technology out of the lab and into the field. As such, we recommend that SCP be reported on the mass and volume of the full ABU (excludes the ECU mass and volume), and the ratio of heat exchanger mass to adsorbent mass be reported to easily move between the two. Further, it should be noted that literature can be inconsistent and report the SCP only accounting for the adsorption time, but other times the total cycle time [60]. This is a bit misleading, as most cases require an equal desorption time and thus the attainable power from the adsorbent bed is half of what is reported. At the system level, SCP should always be reported for the total cycle time to remove confusion.

2.4. ADSORPTION LAYER MODELING APPROACH

Across the various designs and materials used for adsorption-based cooling devices, the approach to modeling the mass and heat transfer in an adsorbent layer is well documented and there is strong consensus in literature. First, mass transfer within the adsorption coating can be described using Eq. (5) [14],[61]:

$$\frac{\partial C}{\partial t} + \nabla \cdot (uC) = \nabla \cdot \varepsilon^{\frac{3}{2}} D_K \nabla C - \frac{1-\varepsilon}{\varepsilon} \frac{\partial C_\mu}{\partial t} \quad (5)$$

Here, C is the concentration of water vapor within the inter-crystalline voids and u is the Darcian velocity of the water vapor through those voids. This advective term can be neglected as the Peclet number (Pe) in these circumstances is often very small and the process is diffusion dominant (Pe < 1). ε is the porosity of the adsorbent layer, and C_μ is the concentration inside of the adsorbent crystals. The porosity can be calculated in Eq. (6), where ρ_c is the crystalline density of the adsorbent and ρ is the observed density of adsorbent for the sample volume. ρ can be determined for a given sample by first determining the mass of the adsorbent in the layer, the volume of the layer, and the environmental conditions that the sample is in to subtract the mass of the adsorbed gas.

$$\varepsilon = 1 - \frac{\rho}{\rho_c} \quad (6)$$

With such small pores and high mean free paths at low pressures, the transport of the vapor is in the transitional flow regime and thus the inter-crystalline diffusion is due to Knudsen diffusion. The Knudsen diffusion coefficient D_K can be found using Eq. (7), where d_p is the characteristic pore size:

$$D_K = \frac{d_p}{3} \sqrt{\frac{8RT}{\pi M}} \quad (7)$$

$\boldsymbol{R}$ is the universal gas constant, $\boldsymbol{T}$ is the temperature of the vapor in degrees Kelvin, and $\boldsymbol{M}$ is the molar mass of the gas. The characteristic pore size, $\boldsymbol{d_p}$ of the inter-crystalline voids can be found assuming the adsorption coating forms a random porous media where the voids can best be approximated using a probabilistic model as a function of the adsorbent crystal size $\boldsymbol{r_c}$ and the porosity of the adsorbent coating. Simple geometric analysis reveals the fundamental limit of the porosity $\boldsymbol{\varepsilon_{HCP}}$ to be $\left(\mathbf{1} - \frac{\boldsymbol{\pi}}{\mathbf{3\sqrt{2}}}\right)$ for hexagonally packed spheres, and the void size can be predicted based on deviation from this limit [62]. By introducing $\boldsymbol{\chi}$ as the ratio of the characteristic void diameter to the crystal radius, we can use the probability function in Eq. (8) to determine the average pore size $\boldsymbol{d_p}$ using Eq. (9) [62]:

$$P(\chi) = 3(1+\chi)^2 \frac{\varepsilon(1-\varepsilon)(1-\varepsilon_{HCP})}{(\varepsilon-\varepsilon_{HCP})} \cdot \exp\left\{-\frac{(1-\varepsilon)(1-\varepsilon_{HCP})}{(\varepsilon-\varepsilon_{HCP})}\left[(1+\chi)^3-1\right]\right\} \quad (8)$$

$$\chi_{ave} = \frac{1}{\varepsilon}\int_0^{\infty} \chi P(\chi) d\chi \quad (9)$$

Once $\boldsymbol{\chi_{ave}}$ is computed, this can be used for the problem at hand as $\boldsymbol{d_p = 2r_c\chi_{ave}}$. In practice, it is challenging to change the size of the crystals for a given adsorbent without changing the inherent characteristics of it, so the packing porosity and coating thickness offer the greatest design variables to optimize performance for a given set of cycling conditions. However, the $\frac{\boldsymbol{\partial C_\mu}}{\boldsymbol{\partial t}}$ term in Eq. (5) scales with $\frac{\boldsymbol{1}}{\boldsymbol{r_c^2}}$, and thus should be considered when selecting a material for a particular objective. This sink term in the equation describes the amount of water entering into the adsorbent crystals themselves, and is often described using the Linear Driving Force Model [63] presented in Eq. (10).

$$\frac{\partial C_\mu}{\partial t} = \frac{15}{r_c^2} D_\mu (C_{eq} - C_\mu) \quad (10)$$

$\boldsymbol{C_{eq}}$ can be determined from the local temperature and pressure and given uptake for the particular material isotherm. Fundamentally, this value is limited by a combination of the pore volume that is available inside of the adsorbent crystal, the affinity for a particular molecule, and the selectivity of the material. Even if a material has high pore volume and affinity for a molecule, if it is not very selective, it may be filled with other molecules of less interest- in the case of atmospheric water harvesting it might allow $N_{2(g)}$ instead of just $H_2O_{(g)}$, reducing the water harvesting potential. $\boldsymbol{D_\mu}$ is the intra-crystalline diffusivity, which is also dependent on the local temperature.

With the mass transport described in the coating layer, the heat transfer must also be captured to fully solve Eq. (10) as it requires the local temperature and pressure to determine $\boldsymbol{C_{eq}}$. From energy conservation, Eq. (11) can be used to find the temperature distribution.

$$\rho c_p \frac{\partial T}{\partial t} + \rho c_p u \cdot \nabla T = \nabla \cdot k \nabla T + h_{ad}(1-\varepsilon)\frac{\partial C_\mu}{\partial t} \quad (11)$$

Here, $\boldsymbol{\rho}$, and the specific heat capacity $\boldsymbol{c_p}$ are averaged values based on the binder characteristics and the adsorbent material. The thermal conductivity of the adsorbent coating, $\boldsymbol{k}$, can be determined by weighting the conductivity of the binder with the adsorbent coating, which can be found using the modified Zhener-Schlunder model for porous media [14], [37], [64].

By coupling Eq. (11) to Eq. (5), the temperature and rate of adsorption can be determined to solve across the domain.

2.5. COMSOL FINITE ELEMENT MODEL

In order to model our device for the tube-fin heat exchanger design, we represent the unit cell for analysis as seen in Figure 16. Basic energy analysis for our operating conditions reveals that at the given flow rate we expect to be flowing through the vehicle (26.4 gal/min for the engine coolant) for a cooling power of 3 kW, there will be less than a 0.5 ℃ difference in fluid temperature from the inlet to the outlet, resulting in a negligible loss in working capacity across the device. Thus, we are able to model the entire system around a single unit cell analysis and scale the results to fit our initial concentration in the voids and crystals are based on the initial temperature T_i. Given that the temperature profile along the length of the fin is also negligible for a properly designed device, the unit cell is modeled as a radially symmetric unit for reduced computational time compared to a 3D model. r_{eff} can be found based on equating the areas of a square unit cell and circular unit cell such that $r_{eff} = \sqrt{\frac{S^2}{\pi}}$, where S equals the pitch between each tube. This is an essential parameter as a very long pitch will increase the conductive resistance of the fin and would require an exponentially increasing convective heat transfer coefficient to achieve the same temperature difference from base to tip.

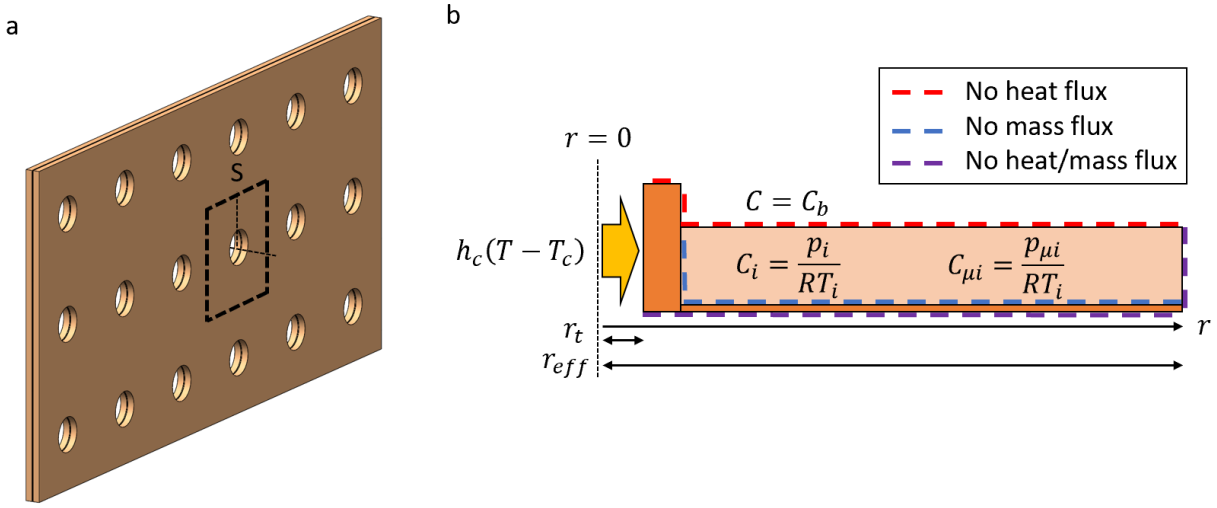

Figure 16. a) Example of a single integrated fin. The dashed line represents the idealized unit fin used for analysis. b) Idealized unit cell with adiabatic and zero mass flux boundary conditions.

The convective heat transfer at the base of the fin comes from pumping engine coolant, or the ambient fluid line, through the tubes running through the adsorbent fins. The temperature of the fluid running through

this line is $\boldsymbol{T_c(t)}$, which is either equal to $\boldsymbol{T_a}$ during adsorption of $\boldsymbol{T_d}$ during desorption. The convective heat transfer coefficient $\boldsymbol{h_c}$ can be found using the Dittus-Boelter correlation given that there is a negligible temperature difference between the tube wall and the working fluid [65]:

$$Nu = 0.023Re^{0.8}Pr^{n} \quad (12)$$

$$n = 0.3: cooling; n = 0.4: heating; Re > 10{,}000$$

$$\boldsymbol{Re} = \frac{\boldsymbol{\rho v D}}{\boldsymbol{\mu}} \quad (13)$$

$$Nu = \frac{hD}{k} \quad (14)$$

$$\mathrm{Pr} = \frac{c_p \mu}{k} \quad (15)$$

In the case of exploring a design with a coolant loop with a smaller Reynold's number, we use the Gnielinski equation[65]:

$$Nu = \frac{\left(\left(\frac{f}{8}\right)(Re - 1000)\, Pr\right)}{1 + 12.7\left(\frac{f}{8}\right)^{0.5}\left(\mathrm{Pr}^{\frac{2}{3}} - 1\right)} \quad (16)$$

$$0.5 \leq Pr \leq 2{,}000; 3{,}000 \leq Re \leq 5e6$$

In the above equations, $\boldsymbol{D}$ is the inner diameter of the tube, $\boldsymbol{f}$ is the friction factor for the tube at the given flow conditions, and $\boldsymbol{Re, Nu,}$ and $\boldsymbol{Pr}$ are the Reynolds, Nusselt, and Prandtl number accordingly. $\boldsymbol{\rho, k, c_p, and\ v}$ all refer to the properties of the fluid in the tube, which are density, thermal conductivity, specific heat, and average velocity respectively. The friction factor can be found using the implicit Colebrook equation [66]. The pressure drop for the device and consequent ideal pumping power can then be computed as:

$$\Delta P = f\frac{L}{D}\frac{\rho v^2}{2} \quad (17)$$

$$\dot{W}_{pump} = \dot{V}\Delta P \quad (18)$$

The volumetric flow rate $\dot{V}$ can be adjusted to ensure sufficient heat transfer to the adsorbent fin without excessive pressure loss.

2.6. SUMMARY

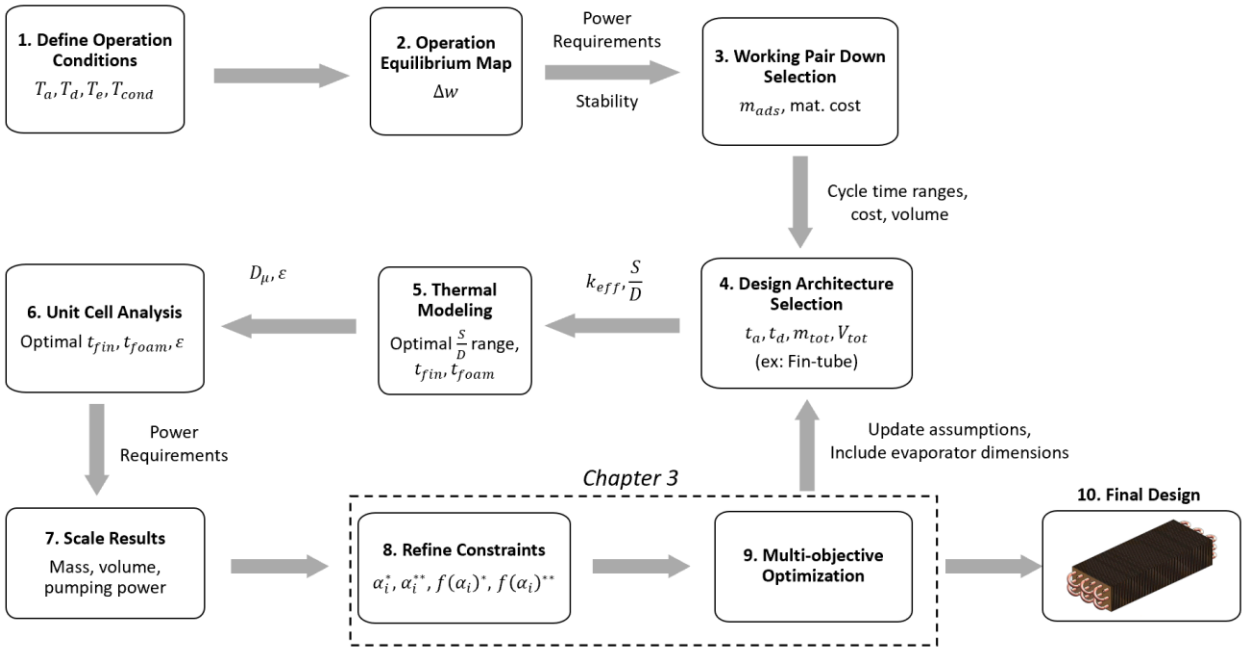

Figure 17. Design and optimization flow chart for adsorption based cooling system design.

In this chapter, we reviewed available literature and leveraged previous work in our lab to understand the thermodynamic cycle of adsorption heat pumps and their potential to replace vapor compression cycles for automotive cooling. We summarized the recommended steps taken in the flow chart found in Figure 17 to produce optimal adsorption-based cooling systems. Once the thermodynamic cycle was understood and operating temperatures established (1), we laid out a framework to select an adsorbent, working adsorbate, and thermal/mechanical binder for a given set of operational conditions based on first principles to generate operation equilibrium maps (2). Once the stability of the material is confirmed, these maps can be used to down select materials on the basis of material cost and mass (3). Based on the objectives and tradeoffs between mass, volume, and operating power, the appropriate design architecture can be selected (4). In order to create a more thorough understanding of the adsorption cycle and its transient nature, we present a set of fundamental equations and correlations to use to govern the heat transfer to determine get geometric parameters (5) and mass transfer in 3 domains: the low pressure vacuum environment the adsorption bed will sit in, the voids between the crystals, and inside of the adsorbent crystals themselves to generate unit cell performance (6). Once unit cell assumptions are validated, the results can be scaled to determine the system level mass, volume, and pumping power (7).

With the current problem well described, we will move on to examine the optimization approach taken for the multi-objective design problem of creating a volume and mass efficient adsorbent bed with maximal cooling/heating potential (8-9) to generate the final design (10).

Chapter 3

3. Design and Optimization of a Full Scale and Reduced Scale Adsorption Based Cooling System

This chapter presents the multi-objective optimization framework that was used to generate a design for a waste-heat driven cooling system for automobiles, as well as the consequent design for a prototype to test this design. We will review the design constraints and objectives for this device, and review the sensitivity of performance metrics to key geometric and operational variables. We will also outline the use of Pareto optimization to examine the tradeoffs between performance and mass/volume of the device. This approach has yet to be taken in the literature, and we present it here to overcome the practical obstacles in designing adsorption cooling systems. While many publications focus on performance based on the mass of the adsorbent in the system, we will show through this chapter that this can lead to sub-optimal integrated system designs when the mass, volume, and pumping power required for the entire system are considered.

3.1. DESIGN CONSTRAINTS: ADSORPTION BED

Everything in an automobile should be considered on a basis that weighs performance enhancement against the mass, volume, and cost of the component. In the case of automotive air conditioning, the expectations of the user are well-defined in terms of target output temperature, which sets the performance requirements for cooling systems in terms of cooling power required. This creates the optimization problem to meet the performance metric with the smallest possible volume, mass, and cost. We worked with our collaborators at Ford to determine the target mass and volume of an integrated cooling device that would fit well within a car, as is summarized in Table 1, without sacrificing passenger comfort by delivering 1.5 kW of average cooling power. It should be noted that this system is to be interfaced with a latent heat storage (LHS) system, rather than a second adsorption bed. As such, this device will need to create 3 kW during adsorption, and the LHS system will supply cooling during the desorption phase. In order to create a system supplying 3 kW at all times, one would simply build an identical ABU to the one proposed here. Details of the LHS system are not able to be shared at this time, so the focus will simply be on the design and optimization of the ABU given the design constraints. However, a diagram of the general system schematic is shown in Figure 18. There are three different fluid lines: the engine line that circulates 90 ℃ fluid in the ABU during desorption, the ambient line that will be the temperature of the environment (23 ℃ 43 ℃) and will cool the ABU during adsorption (absorbing the enthalpy of adsorption) or cool the ECU during desorption (where it will be condensing

and the heat of condensation needs to be rejected), and the cabin line that circulates in the cabin to keep passengers cool. The cabin line is connected to the ECU during adsorption, and the ECU is designed to take in 8 ℃ from the cabin and outlet 6 ℃ coolant. This will pass through the LHS to recharge it, which will then output 7 ℃ to the cabin for cooling. During desorption, the cabin line forms a closed loop with the LHS to provide cooling while the ABU recharges.

Table 1. Adsorption bed design constraints.

Constraints	Target
Adsorbent Mass m_{ads}	< 3.3 kg
Adsorbent Bed Mass $m_{ads,tot}$	< 9.5 kg
Adsorbent Bed Volume $V_{ads,tot}$	< 14 L
Ambient Temperature T_{amb}	23 - 43 ℃
Cooling Power $\dot{Q}_c$	1.5 kW (average)

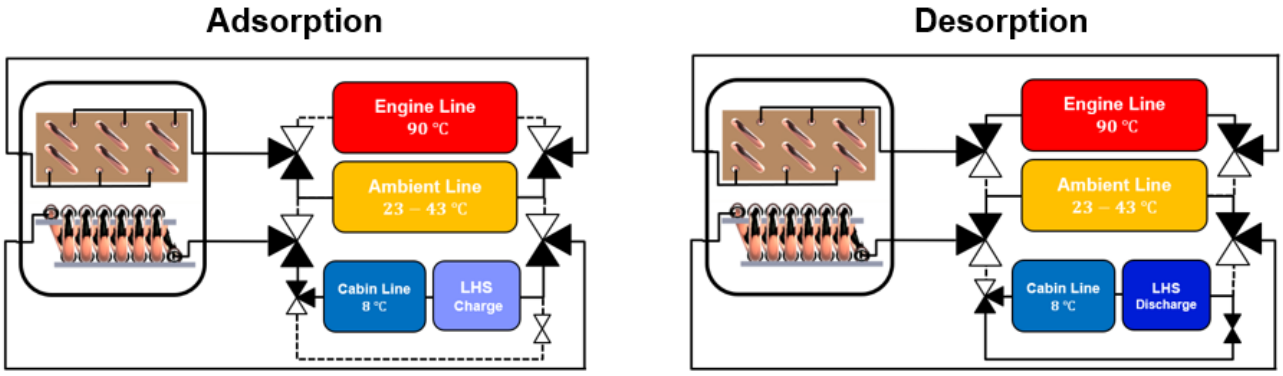

Figure 18. Adsorption and desorption flow patterns with the LHS system. The LHS provides cooling during desorption, while the ABU recharges the LHS during adsorption by providing cold circulating water that simultaneously cools the cabin.

3.2. DESIGN OPTIMIZATION: ADSORPTION BED

The design and optimization of the adsorption bed must account for many factors, across many length scales. The geometric and material packing factors can be seen in Figure 19, and the steady state operational variables are the adsorption time t_a, desorption time t_d, and the coolant flow rate $\dot{m}_c$. t_{foam}, t_{gap}, and t_{fin} are the thickness of the highly porous (95-98% porosity) copper foam, the vapor gap between fins to ensure unimpeded vapor transport, and the thickness of the copper fin. The foam and fin will later be brazed

together to form a highly conductive composite fin, which will then be coated with the adsorbent. The height, and width of these fins can be determined by the pitch distance between each tube S, the tube diameter D, and the number of tubes and tube passes. Finally, the overall length of the ABU L_{ads} can be determined once the number of fins is determined to reach the desired power. This will be highly depending upon the adsorbent coating performance, largely dictated by the target porosity ε, the adsorbent crystal radius r_c, and the inter-crystalline void side d_p.

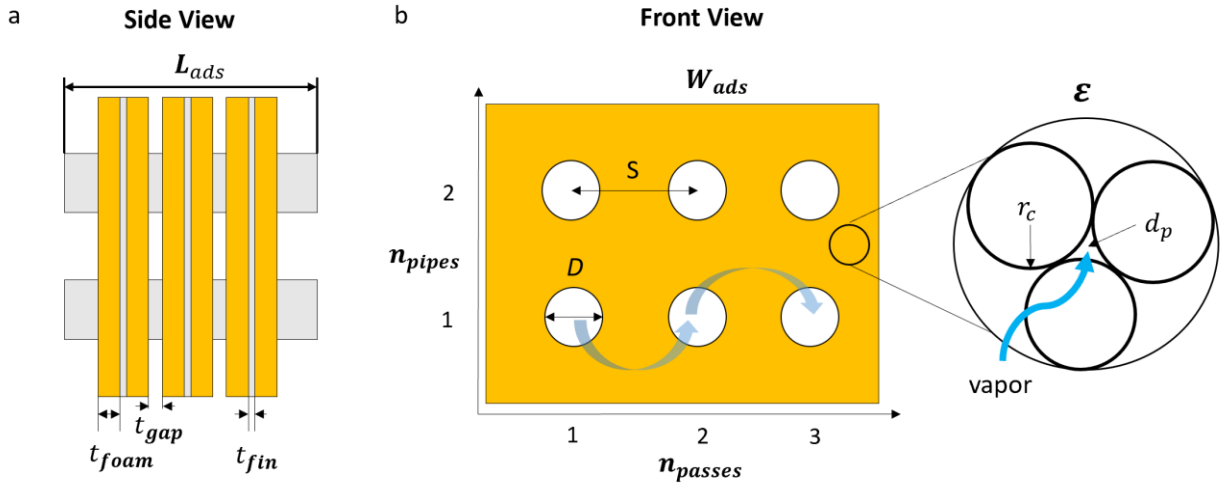

Figure 19. a) Side and b) Front view schematic of a plate and fin type adsorption bed, indicating key parameters of the physical design that dictate performance.

Adsorption based cooling systems are often compared across many metrics, such as the specific cooling power (SCP) with respect to mass or volume. The average cooling power $\dot{Q}_c$ can be calculated for a full adsorption and desorption cycle as:

$$\dot{Q}_c = \frac{\int_0^{t_a} \dot{m}_{ads}(t) h_{fg} dt}{t_a + t_d} \quad (19)$$

Thus, the SCP with respect to mass, SCP_m, and with respect to volume, SCP_v, can be calculated by dividing $\dot{Q}_c$ by the appropriate mass or volume. Most often, the SCP_m and SCP_v metrics in literature is with respect to the mass or of the adsorbent material, respectively. As mentioned earlier, this can be misleading unless the goal is only to compare materials or coating methods against each other (as we will do later in this work). We recommend using $SCP_{m,tot}$ and $SCP_{V,tot}$ for all device designs as a more holistic figure of merit. An additional metric to consider is the ratio of adsorbent mass to mass of the heat

exchanger components before adding adsorbent, which can serve as a quantitative assessment of the overall device design efficiency by comparing power generating mass to thermal mass.

3.3. HEAT TRANSFER DESIGN CONSIDERATIONS

The unit cell discussed in Chapter 2 can be thought of as an extended fin with a temperature and concentration dependent volumetric heating term, with a convective boundary condition at the base and a adiabatic fin tip. As this is a problem that can only be solved numerically, we look to simplify the problem to get intuition and understand the impact of the ratio of the spacing between the tubes *S* to the tube diameter and the temperature distribution along the length of the fin. The first step that can be taken is to reduce the heat transfer problem to a 1D problem, which can be possible if the Bi number is less than 0.1 through the thickness of the fin [67]. Considering the thermal conductivity in the direction of the thickness to be found according to Eq. (20) and an effective heat transfer coefficient approximated by Eq. (21), we can see that the Bi is much less than <0.1 by order of magnitude analysis.

$$k_{eff,t} = \frac{\left(k_{fin}\frac{\delta_{fin}}{2} + k_{foam}\delta_{foam}\right)}{\frac{\delta_{fin}}{2} + \delta_{foam}} \quad (20)$$

$$\bar{h}_{eff} = \frac{\frac{\dot{Q}_c t_a}{(t_a + t_d)V_{ads}}\frac{h_{ad}}{h_{fg}}\left(\delta_{foam} + \frac{\delta_{fin}}{2}\right)}{\Delta T_t} \quad (21)$$

$$\overline{Bi}_{eff} = \frac{\bar{h}_{eff}\left(\delta_{foam} + \frac{\delta_{fin}}{2}\right)}{k_{eff,t}} \quad (22)$$

With sufficient $\boldsymbol{h_c}$ and $\boldsymbol{\delta_{fin}}$, there will be a negligible temperature gradient along the length of the fin and a near constant boundary temperature, enabling the quickest possible adsorption by effectively removing the heat generated due to the enthalpy of adsorption. However, for a given tube diameter, higher $\boldsymbol{h_c}$ requires a faster fluid velocity and consequentially more pumping power according to Eq. (18), and the fin thickness adds more thermal mass that does not have any uptake potential. To explore the tradeoffs of

this problem, Figure 20 and Figure 21 show the impact of the performance of the device while varying the tube spacing $\boldsymbol{S}$ and $\boldsymbol{t_{fin}}$, for a given $\boldsymbol{D}$ and flow rate using the COMSOL model described in Chapter 2.

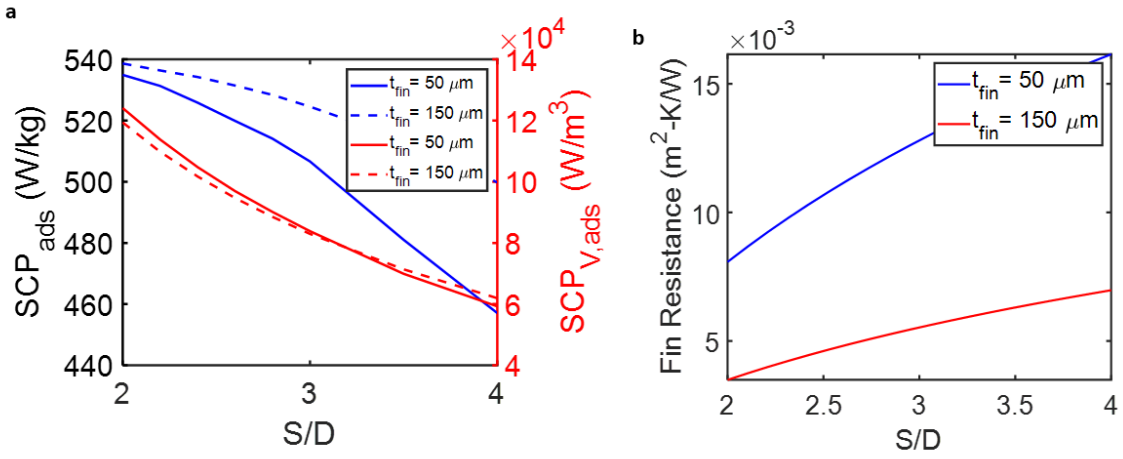

Figure 20. a) SCP with respect to adsorbent mass and volume as a function of S/D for different fin thicknesses. b) Fin resistance as a function of S/D and fin thickness.

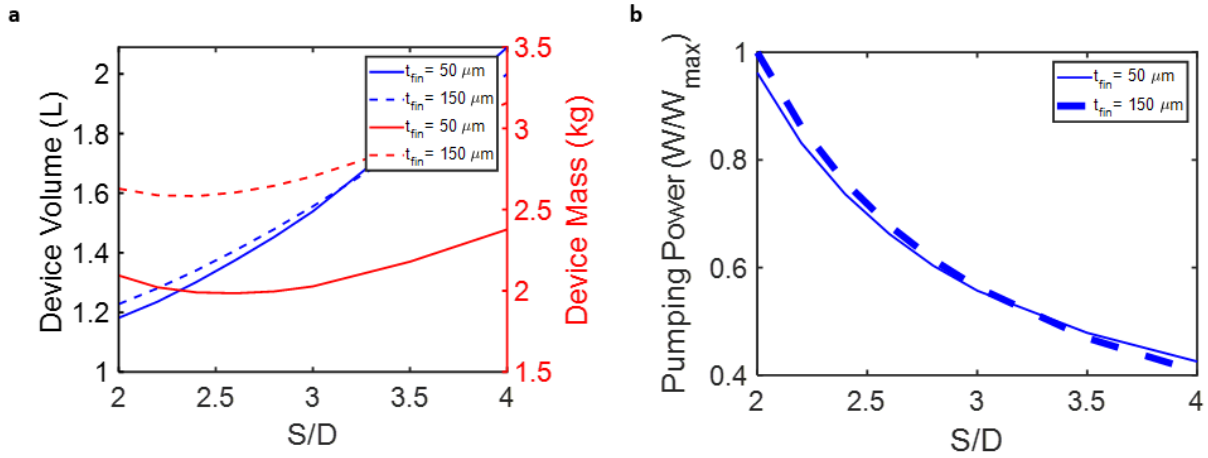

Figure 21. a) Total device volume and mass as a function of S/D. Fin thicknesses vary from 50 μm to 150 μm. b) Normalized pumping power as a function of S/D.

Figure 20 shows that while the SCP_{ads} decreases with S/D with constant fin thickness and flow rate, it increases with t_{fin}. This is because the ratio of conductive resistance through the fin to convective resistance at the base decreases. With just this information, the designer may think to minimize S/D. However, Figure 21, shows the total mass and volume of the device needed to meet the target objective and different, more holistic conclusions can be drawn. In fact, an S/D of 2.7 is the mass optimal solution for a 50 μm fin, and a fin thickness of 150 μm is much less efficient at the systems level, despite better specific

cooling powers with respect to material mass and volume. This is a result of the additional thermal mass added that has no ability to generate power. Thus, we recommend that more consideration be given to the system level efficiency, rather than just the performance of the material by itself, to create the best overall designs, as new design trends emerge at this level. While greater performance can be gained in terms of maximum cooling power for a thicker fin, it is less mass efficient. There is a tradeoff for volumetric efficiency, however, as longer fins require a thicker fin to reduce their thermal resistance, as can be seen in Figure 20 where the volume lines cross. If the fin is not sufficiently thick, it is not able to effectively transfer heat from the adsorbent to the coolant, reducing the uptake ability of the adsorbent at the end of the fin. As a result, the thinner fins require more unit cells once S/D>3.3 and become less volume efficient, also impacting the required pumping power for operation.

However, in addition to system level considerations of mass and volume, as Figure 21 also shows the impact of S/D on the pressure drop through the ABU. Smaller unit cells (low S/D) require a large number of total unit cells to achieve the given power requirement, and require longer lengths of tubing creating a higher pressure drop. By normalizing the pressure drop by the largest measured pressure drop calculated for this set of points, it is clear that the pumping power is very sensitive to the S/D ratio. While we can see that in general SCP_{ads} and $SCP_{V,ads}$ decrease with a higher pitch distance, it is favorable to move to a higher pitch distance to reduce the required pumping power and overall device mass at the expense of system volume.. We show Figure 22 for convenience to see that and while S/D<2.67, increasing S/D decreases ABU total mass and pumping power. It is here that we see the interplay between a highly efficient design from a power generation standpoint, and an effective system design. Taking the entire system into account, we can see in that there indeed is an optimal S/D ratio and fin thickness for the given set of operational conditions in the previous figures. Because the mass of the copper tubing is a significant portion of the unit cell mass, reducing the total length of tube required is essential to reducing the mass of the device.

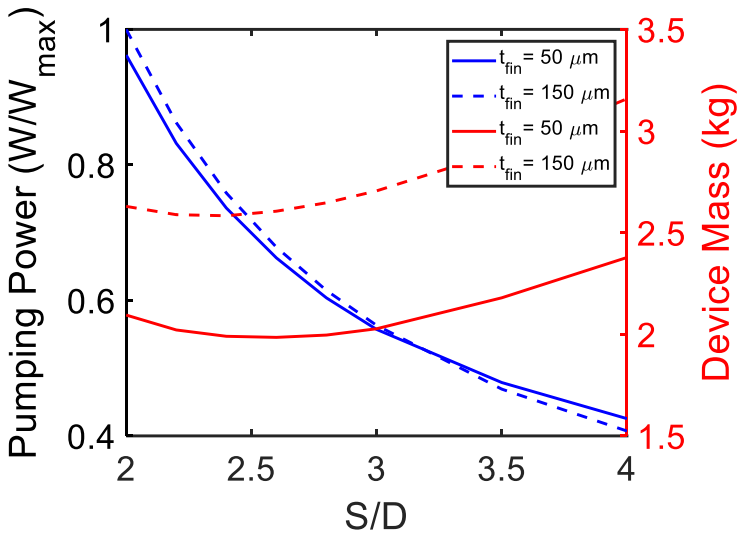

Figure 22. Pumping power and device mass as a function of S/D and fin thickness.

In addition to the fin thickness, the thickness of the copper foam has an impact on the thermal performance of the device, but as can be recalled from our discussion of the mass transport governing equations, the diffusion time scale for adsorption scales with $\frac{1}{\delta_{foam}^2}$ and has a much larger impact on performance than the thermal considerations for moderately thin, conductive coatings such as these.

Finally, the mass flow rate of the coolant and the size of the tube have a significant role in the thermal performance of the device, as a high Re number are required to ensure sufficient Nu number according to the Dittus-Boelter correlation. However, it is generally understood that the pressure drop penalty for Re>10,000 quickly overcome the additional heat transfer benefits and should generally not be exceeded for these devices except under high adsorption temperature conditions where the uptake is very temperature dependent.

3.4. MASS TRANSFER DESIGN CONSIDERATIONS

For an optimal device design, efficient mass transfer must be balanced with a mass, volume, and pumping power. Unfortunately, there is an inverse relationship between the packing density, or the amount of adsorbent per unit volume, and the adsorption rate. Highly porous adsorbent coatings enable the fastest vapor transport through the thickness of the coating, as it is governed by the $\varepsilon^{\frac{3}{2}} * D_K$ term in Eq (5), which we will refer to as the effective diffusivity D_v. D_K is also a function of porosity, as higher porosities also have larger characteristic pore sizes d_p and thus creates a lower mass transfer resistance.

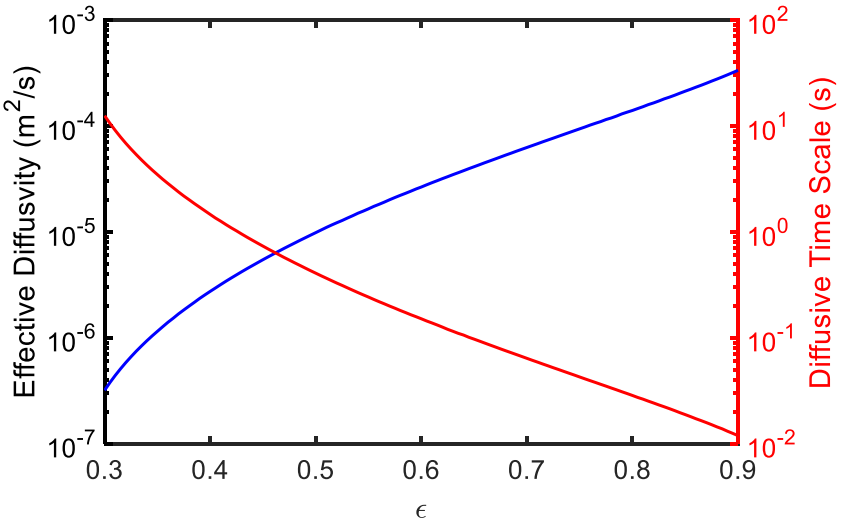

Figure 23. Effective diffusivity as a function of porosity on left axis, assuming a crystal radius of 2.5 micrometers. On the right axis is the characteristic diffusive time scale for a 2 mm adsorbent coating as a function of porosity.

Figure 23 shows how the effective diffusivity changes as a function of porosity, which drastically impacts the inter-crystalline diffusive time scale $\left(\frac{t_{foam}^2}{D_v}\right)$ through the thickness of the adsorbent coating. The inter-crystalline diffusive time scale shifts from the order of seconds at porosities of 0.5, to 0.1 seconds at 0.65 porosity. Kim *et al*. were able to develop an effective scaling analysis to derive the optimal thickness for thermal energy storage that is a good approximation to use for this device [14]. It should be noted, however, that there is a key difference between the previous thermal storage work and this device: power generation takes precedence over energy storage density, and thus it is advantageous to have thinner coatings, more porous structures, and to end the cycle well before the saturation conditions for both adsorption and desorption to ensure a large driving potential exists at all times to keep kinetics fast.

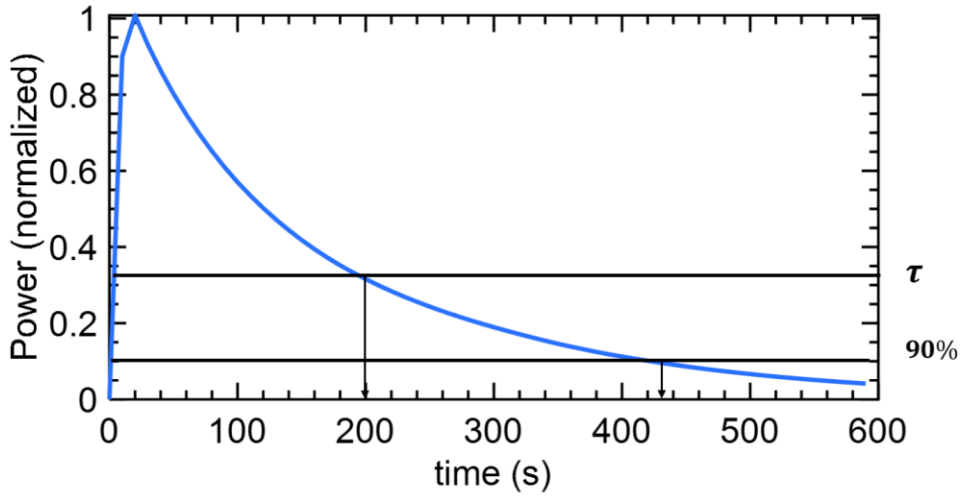

Figure 24. The normalized power curve for a 1 mm adsorbent coating, S/D =3, with 200 seconds for adsorption and desorption. Also shown are the characteristic time of adsorption for this design for optimal performance, and the time for 90% power saturation.

Figure 24 shows the normalized power curve for one of the final designs as a function of time. If we stop the adsorption time at 200 seconds, it coincides with a general characteristic time scale τ of $\left(1-\frac{1}{e}\right)$, often used for the optimization of dynamic cyclical systems [68]. While one could increase the adsorption time, it is clear that the integral under the curve after 200 seconds is small compared to the first 200. It takes around 430 seconds to reach 90% of the total energy possible, but has only added an additional 20% energy while more than doubling the adsorption time. This pulls $\dot{Q}_c$ down significantly, indicating that a shorter adsorption time will result in a more efficient design. In terms of scaling, if we reduced the porosity or increased the coating thickness, this curve would flatten slightly, shift to the right, but would have a higher tail due to its slower adsorption but higher adsorbent density.

Understanding the impact of porosity and thickness on the inter-crystalline diffusive time scale τ_v enables us to balance it with the intra-crystalline diffusive time scale τ_μ, which scales with $\frac{r_c^2}{15D_\mu}$. Qualitatively, this balance can be seen in Figure 25.

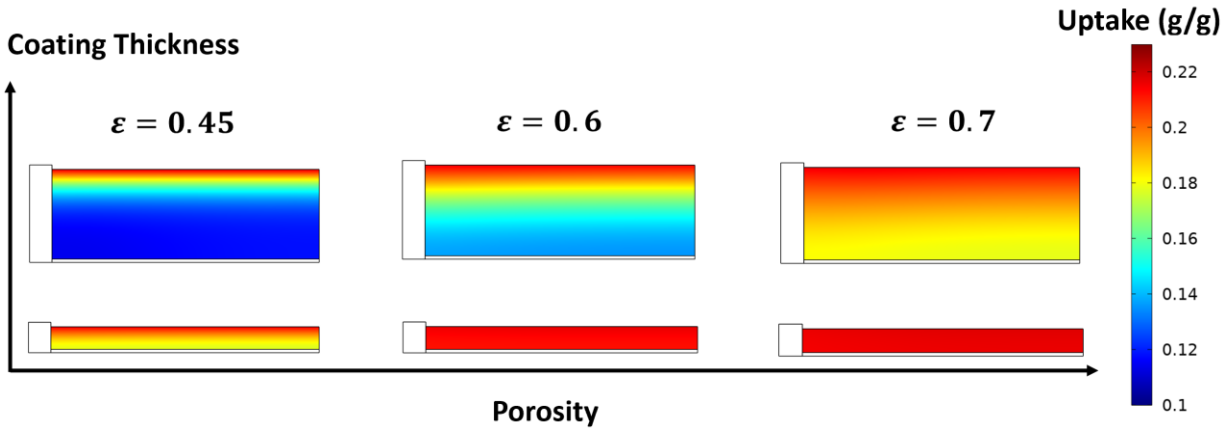

Figure 25. Spatial variations in uptake as a function of porosity and coating thickness from COMSOL model. The top figures have an adsorbent coating of 2 mm, and the bottom are 0.5 mm.

In this figure, all models used a 200 second adsorption time at 38 ℃, S/D = 3, tube diameter of 5 mm, fin thickness of 150 micrometers, and a mass flow rate of 0.15 l/s. For low porosities, even for very thin coatings, we see that at the end of adsorption there is still a spatial gradient in the utilization of the adsorbent coating. This is very pronounced for the thicker 2 mm coating. It should also be noted that the 1D nature of the gradient demonstrates sufficient heat transfer is taking place to ensure that temperature gradients in the radial direction are negligible. A higher S/D would require a thicker fin or faster flow rate to maintain this relationship. As we move to a more moderate porosity of 0.6, we see that the thin coating is nearly saturated and fully utilized, while the thicker coating still has a non-negligible gradient. τ_v is still too large, but as we move to a higher porosity the 2 mm coating shows good utilization. The existence of a spatial gradient indicates that the coating is still adsorbing at a fast rate, keeping power production high. For the thinner coating, it would be advantageous to end adsorption earlier as its peak power generation has passed.

In Figure 26 - Figure 28, we can move towards understanding the system level impacts of balancing porosity and coating thickness. In all of the figures that follow, a discrete set of points were simulated due to the computational resources required. However, we have confidence that these figures capture the trends well enough to understand the system level tradeoffs to inform final designs. In Figure 26, we can see some distinct trends. The uptake difference $\Delta\omega$ can be seen to saturate for the 200 second cycle at 0.5 mm coating thickness at relatively low porosities, and less than 5% of the potential uptake is gained after a porosity of 0.6. This must be balanced with the packing density of the adsorbent per unit volume of device, which decreases linearly with porosity. It should also be noted that the packing density increases with coating thickness, as the ratio the vapor gap, fin thickness, and volume taken up by the tubing to useful adsorbent coating decreases with coating thickness. This trend then elucidates the trade-offs that can be seen in Figure 27, where the adsorbed water density can be calculated as:

$$\rho_{\Delta\omega} = \Delta\omega\, \rho_c\, (1-\varepsilon) \frac{V_{ads}}{V_{unit}} \quad (23)$$

As the packing density decreases linearly and $\frac{d\Delta\omega}{d\varepsilon}$ decreases rapidly as the porosity increases past 0.6, we see that an optimal porosity for the coating thickness shifts as it gets thinner to have the most volume effective design for a given adsorption time. Thinner coatings will be more volume efficient for shorter adsorption times and lower porosities to maintain the ratio of $\frac{\tau_v}{t_a}$, or more explicitly $\frac{\delta_{ads}^2}{\varepsilon^{\frac{3}{2}} D_k(\varepsilon) t_a}$, and thus have a volumetric advantage over thicker coating for short adsorption times.

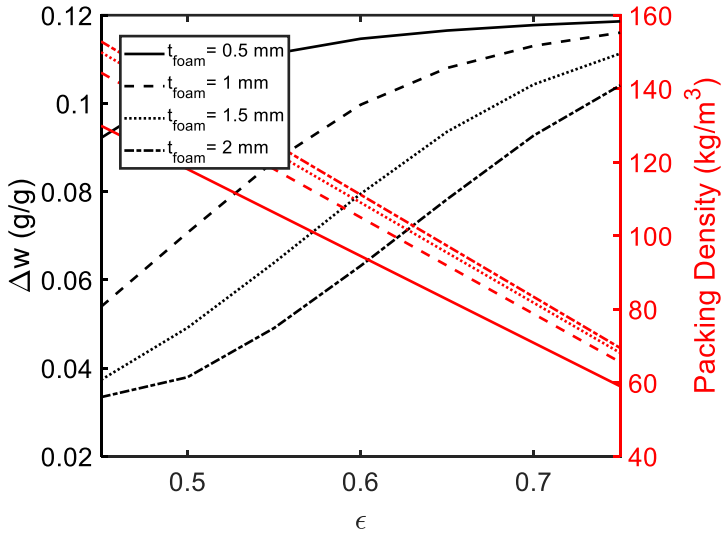

Figure 26. Uptake difference as a function of porosity shown with the packing density of adsorbent per unit volume. Outputs are shown for various adsorbent coating thicknesses.

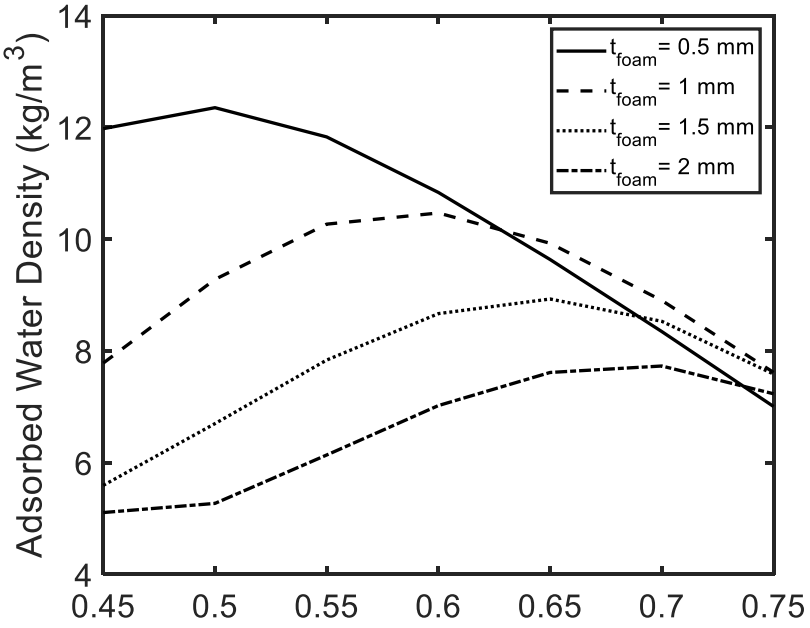

Figure 27. Absolute adsorbed water density in kg of water per volume of adsorbent as a function of porosity. Outputs are shown for various adsorbent coating thicknesses.

However, as has been seen in the case of our thermal analysis, the most volume efficient solution may not be the most mass efficient design due to its need for more individual unit cells and thus more tubing. Figure 28 shows that at the device level for these parameters, a coating thickness of 0.6 porosity and 1 mm is the optimal design, followed by 0.5 mm at 0.5 porosity. Roles reverse on the volume front, as 0.5 mm is the

most volume efficient design at the device level and 1mm is the second best. While thicker coatings were explored, it was clear from early analysis that this is the ideal range based on the particular working part and adsorption time for this cycle.

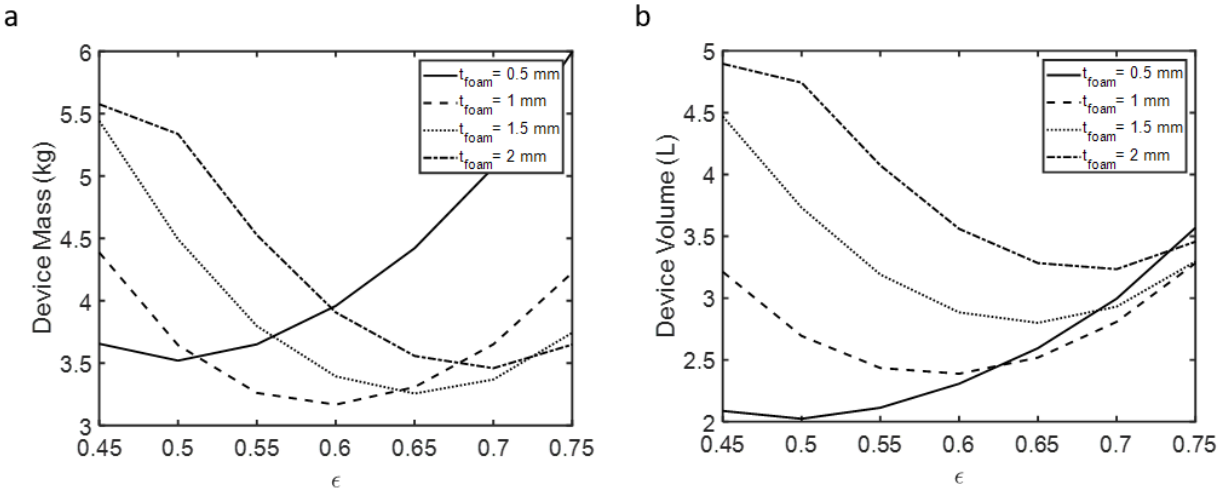

Figure 28. a) Total device mass in kg as a function of porosity. Values are shown for various adsorption coating thicknesses. b) Device volume as a function of porosity.

Once again, this problem will not have a single optimum solution, but rather a surface of optimal solutions trading mass, volume, and required pumping power. In the next section, we will lay out the multi-objective framework that was followed to generate this set of optimal designs to balance these tradeoffs.

3.5. MULTI-OBJECTIVE DESIGN FRAMEWORK

We can take our understanding of the tradeoffs between the physical parameters of the device, trying to ensure as isothermal of a process without introducing excessive pumping power penalties and additional mass for thick copper fins, while also balancing mass transport with packing efficiency. Additionally, we aim to operate in the fastest part of the uptake curve by stopping adsorption and desorption processes before saturation occurs. With eight parameters to sweep in a highly transient process while simultaneously trying to minimize the mass, volume, and pumping power of the device to meet our design requirements, we utilize a formal multi-objective optimization framework [69].

First, we create the design parameter space α_i, where *i* is an index representing the design parameter number (in this case we have eight total) and based on our intuition from studying the impact of individual components on the heat and mass transfer we can set upper and lower bounds on the design parameters as α_i^* and α_i^{**}, respectively. These design variable constraints are iterative, and when working with suppliers can continue to be adjusted or even add discretized constraints to fit the stock on hand. Functional

constraints, such as the overall height, width, and length of the final device can be captured as another set of equations $f(\alpha)$. This should include ranges of feasible design variable relationships, such as a pitch distance that is possible to manufacture, or the expected Bi of a given fin and adsorbent coating configuration. At this point, we have drastically reduced the solution space that needs to be swept once our intuition built upon scaling analysis is combined with practical limitations.

Finally, we implement the set of criteria constraints ϕ_i, summarized in Table 1 to ensure sufficient performance and bounding the volume and mass deemed acceptable. These criteria equations can be thought of as the objective functions, and as such we seek to minimize the mass, volume, and pumping power required for a given design. When running the optimization code in MATLAB, which is built around MATLAB's built in Pareto-optimal functions, each point that satisfies the maximum allowed ϕ_i will be included in the possible solution space. With three objective functions, there does not exist a single optimal solution, but rather a surface of optimal solutions that consists of the design points that have the minimum distance from the origin (assuming each criteria is weighted equally). With the surface in hand, we generate multiple solutions that the customer can chose from based on their own preference of mass, volume, and pumping power that can be further explored to ensure the detailed design is feasible. This approach needed to be taken twice, once for the full-scale design and again for the scaled down prototype, as each had its own unique optimum conditions.

3.6. DEVICE DESIGN RESULTS

Based on this approach, we were able to select designs for various adsorption times to work with Ford, with the following results in Table 2, with a an $SCP_{m,tot}$ of 234 W/kg, and $SCP_{V,tot}$ of 125 kW/m^3. While these values are projections and must be validated, they would represent the most efficient adsorption bed for automobiles to date, and the only one clearly tested in literature p to the required 43 ℃.

Table 2. Results from the multi-objective optimization for a full scale 1.5 kW waste heat driven air conditioning system for various adsorption times.

t_a (s)	200	250	300	600
Zeolite Mass (kg)	3.3	3.6	3.9	6.4
Foam Mass (kg)	3.2	3.5	3.8	6.2
Fin+Pipe Mass (kg)	1.0	1.1	1.2	1.9
Total Mass (kg)	7.5	7.0	7.7	14.5
dP (Pa)	3.71E+04	4.07E+04	4.42E+04	7.85E+04
Volume (L)	12.2	13.3	14.5	23.7

The objectives are best met with the 200 second cycle design, with the smallest overall device design in terms of mass and volume, while also having the smallest pressure drop. The target volume and mass for the overall device were easily met with this approach. It can be noted that in the case of this larger scale design, where the tubes are 2 cm (OD), the tube mass becomes less overall because the ratio of tube mass/unit volume decreases with increasing OD due to geometric factors and a better radius to wall thickness ratio.

While the prototype did not have explicit performance constraints on volume or mass, the final design for the prototype was designed around the constraints of the vacuum chamber that it will be tested in and to average 150 kW cooling power. We chose to keep the adsorption cycle time, coating thickness, and

porosity the same as the full scale device to keep comparable mass transfer performance.

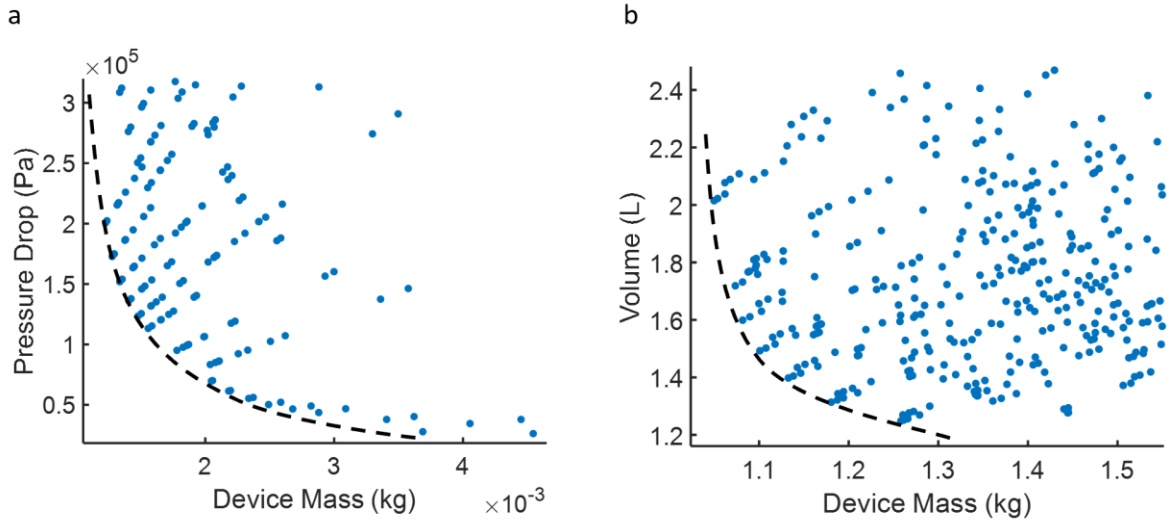

Figure 29. a) Pressure drop and device mass shown with the Pareto front in the black dashed line from simulation results. b) Volume and device mass shown with the Pareto front in the black dashed line from simulation results. Each dot represents a simulated design.

We show the results of our simulations and optimization framework to generate the Pareto optimal surface split into two charts in Figure 29. There is a clear pareto front that has formed, as expected for a well-conditioned multi-objective optimization problem. It can be seen from Figure 29a that the device mass shown on the x axis is very different from Figure 29b, and this is expected because the most mass efficient designs require fast flow rates, often requiring excessive pressure drops through small tubes. As a result, pressure drop grows with the square of the fluid velocity, and the only way to outperform previous designs is with a faster flow with more pressure drop. With the Pareto surface formed, the final design for the prototype to be manufactured was selected. After considering the limitations of the manufacturers, and suppliers, the design in Figure 30 was created. It is of no surprise from our previous analysis showing the optimal S/D ratio to sit below 3 from a mass standpoint. However, we also see from previous results that the pressure drop decays rapidly until an S/D of 3.25. As such, an S/D of 3.25 was selected. The system level predictions are shown in Table 3.

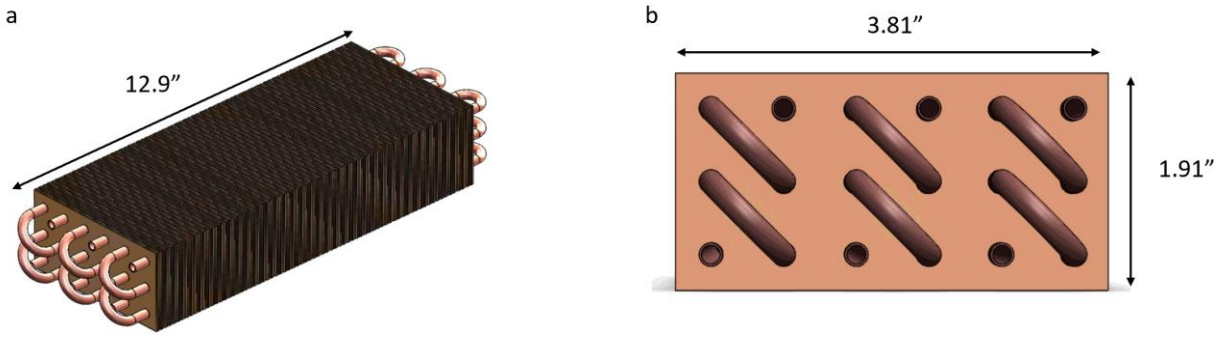

Figure 30. Final design of the 1:10 scaled down prototype, complete with seventy-five fins, and three 5 mm tubes.

Table 3. Summary of Prototype Parameters and Performance Metrics.

System Parameters		Performance Metrics	
t_a (s)	200	SCP_{ads} (W/kg)	490.45
Zeolite Mass (kg)	0.31	$SCP_{m,tot}$ (W/kg)	127.42
Foam Mass (kg)	0.29	$SCP_{V,tot}$ (W/L)	207.45
Fin+Pipe Mass (kg)	0.58	$\frac{m_{ads}}{m_{dm}}$	0.35
Total Mass (kg)	1.2		
dP (Pa)	2.1e5		
Volume (L)	1.6		

The device is currently under fabrication and being assembled at the time that this thesis is being submitted. The fabrication process includes 4 major steps. First, Voss Manufacturing has created custom dyes and rigs to cut the foam and fin with tight positional tolerances to minimize tolerance stack up over the length of the device for latter steps, as well as created a flange to ensure good contact with the copper tubes. Next, the foams and fins were sent to VacuuBraze, which uses a custom brazing process involving an 80% by weight metal powder paste coated on the fin. The fins are placed in a vacuum brazing oven to keep the samples from oxidizing and to remove the filler from the paste, leaving only the highly conductive metal behind to form a highly conductive bond between the foam and fin. Next, we deposit the zeolite on the brazed assembly, which will then be sent to Super Radiator Coils for tube expansion and the final assembly of the header/ connection ports.

So far, the foams and fins have been cut with custom dyes and rigs to ensure minimal tolerance stack up during the brazing and consequent tube expansion process and can be seen in Figure 31. In Figure 31b, we see the 1 mm flanges that were punched and oversized for the 5 mm copper tubes to be inserted. The custom dyes were created at Voss Manufacturing to create 1 mm flange on the copper fin to ensure there is sufficient contact with the copper tubes after tube expansion for maximum heat transfer. It should be noted that while a fin thickness of 50 μm was optimal, it is too thin to achieve the desired flange height of 1 mm required for tube expansion with 5 mm tubes. With larger tubes for the full scale device, we do not expect this to be the case as the stress around the hole scales with $1/r^2$ and should not see any cracking. Between this manufacturing limitation and the less than ideal tube wall thickness to tube radius ratio for small tubes, the adsorbent mass to HX mass ratio is higher than expected for the full scale device.

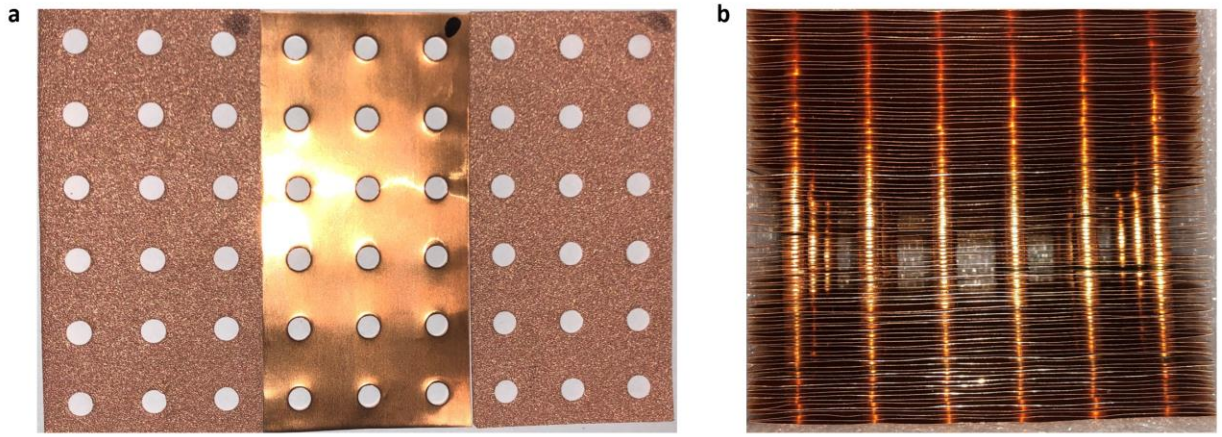

Figure 31. a) Copper foam and copper fins cut to size for the final device. b) Copper fins aligned show precise positional location of flanges ensures sufficient tolerance for tube expansion process.

3.7. EVAPORATOR DESIGN AND ANALYSIS

One key area in adsorption cooling solutions that is often overlooked is the evaporator and condenser design. Often times, they are copper tubes immersed in water, resulting in a substantial thermal mass of water. Unless the device operates with enough of a superheat to boil, this design is very inefficient as it has to overcome the large conductive thermal resistance of the water layer on top of the evaporator surface, potentially leading to a very small temperature difference between the working fluid and the evaporator tube surface. Additionally, the condenser is often a tube that is wasted space and mass during adsorption. We propose a compact combined evaporator and condenser unit (ECU) that utilizes capillary wicking to wet the surface of the tube coated with a copper foam. Similar to the previous section, we

will focus on the analysis for the prototype that is currently being produced, as the methodology is exactly the same.

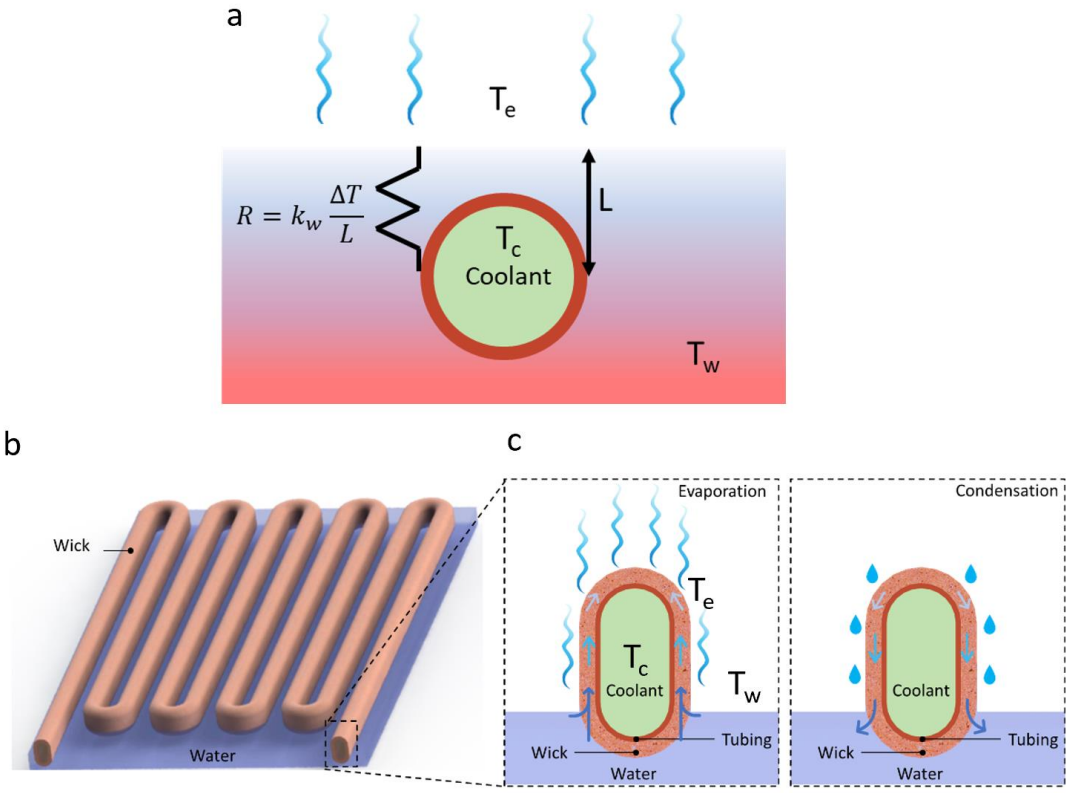

Figure 32. a) Fully submerged evaporator coil that must overcome the thermal mass of the water layer before providing cooling to the coolant. b) Schematic of proposed thin film evaporator in a serpentine path. c) Detailed view of working principal of the ECU. *Figures b) and c) were created by Dr. Xiangyu Li and adapted for this work.

In Figure 32, we show the submerged circular tube design with high thermal resistance between the coolant and the evaporating surface. In panels *b* and *c*) we show the proposed ECU in a common serpentine path for easy visualization, and a cross-sectional view of the proposed capillary wick coated flat copper tube. The benefit of the thin-film capillary evaporator, which will also serve the purpose of condenser, is two-fold. First, the addition of a thin capillary wick, likely a copper foam, allows us to reduce the thermal resistance between the evaporative surface and the coolant. The alternative that we have commonly seen for sorption systems is a fully submerged evaporator coil, which relies on cooling the entire thermal mass of the water at temperature T_w before the coolant traveling though the tube will see any effect of cooling. It should be noted that the conductivity of water is only 0.4 W/mK, so the temperature difference between the water at the evaporative surface and the tube wall is much higher than is the case for a capillary wick evaporator. The wick has an effective conductivity of 19 W/mK, and by intentionally keeping the wick

thin, and with reasonably small pores, the entire wick-water coating on the tube will be almost equal to the temperature at the evaporative interface T_e - decoupling the tube surface temperature from T_w of a larger thermal reservoir, as is the case in Figure 32*a*. The second benefit is that the capillary wick on the evaporator enables the whole surface of the evaporator to be used as an evaporative surface. When combined with the first effect, the effective heat transfer coefficient, *U*, and the surface area available for evaporation, *A*, is considerably higher than a traditional evaporator for sorption systems, which likely has no surface directly exposed to T_e . This performance enhancement results in shorter tube lengths, requiring less footprint, bends, and ultimately thermal mass than traditional evaporative coils for the same cooling potential. The reduction in materials/footprint and higher efficiency of this system offsets the estimated cost of the commercially available copper foam that would be brazed to the surface.

We propose the use of a flattened tube for the ECU due to its enhanced perimeter to area ratio, simultaneously increasing the fluid velocity and the exposed area of the wicking structure by limiting the covered portion of the tube to the tube width and the desired height of working fluid. For small reservoir heights, as is desired to minimize thermal mass of the water, a flat tube has much more exposed area than a circular tube. These tubes are made by creating custom mandrel with a thickness set to b, the inner width of the tube, to form the tube around with compression. The inner height of the tube, a, is simply the result when assuming the midline-perimeter stays constant- a reasonable assumption for ductile materials like soft copper tubing. We are able to calculate the pressure drop for this configuration by calculating the hydraulic diameter of the new cross section [70]. This pressure drop estimate can be further refined by the prior work of Jones showing that the effective-laminar-diameter idea used to relate pressure drops can further be collapsed onto the moody chart and has generated tables that were used in our analysis [71]. We can estimate the length of the evaporator needed to take a 8 ℃ inlet down to 6 ℃ at the outlet for our desired flow rate based on the LMTD approach with a constant surface temperature. Based on the cooling power and thermal resistance across the evaporator, we expect the surface temperature T_e to be 5.5 ℃. With such a small temperature difference, and the inlet and outlet temperatures defined, the mass flow rate was locked in and the only free parameters to design around are the tube diameter to be used and the length of the device. Multiple design sweeps were made to find the tradeoffs between length and pressure drop with the following equations as a guide:

$$\dot{Q} = \dot{m} c_p (T_o - T_i) \quad (24)$$

$$\dot{Q} = U A_s \frac{(T_e - T_o) - (T_e - T_i)}{\ln((T_e - T_o)/(T_e - T_i))} \quad (25)$$

Here, *U* can be calculated with standard convective heat transfer relations discussed previously along with the anticipated conductive resistances through the tube and foam/water matrix, and $A_s = \pi D L$. Setting Eq.

(24) and (25) equal to each other, we can vary the tube diameter or length to ensure a sufficient surface area for our desired ΔT. By adding in the ability to change the aspect ratio of the tube, we introduce an additional parameter to optimize, with the results shown in Figure 33. By increasing the a/b ratio to 2.67, the ECU's total length and consequent mass is reduced by 25% compared to the circular tube design. This design still requires a pumping power that is less than 3% of the total cooling power produced in the cycle and is thus more than acceptable given the mass and volume reductions. While this analysis was conducted for the 0.25" tube used for the prototype, a similar trend is found for the full scale device with less pumping power required due to the larger hydraulic diameter. In order to make the final design decision, we need to ensure once again consider the mass, volume, and pumping power required at the system level.

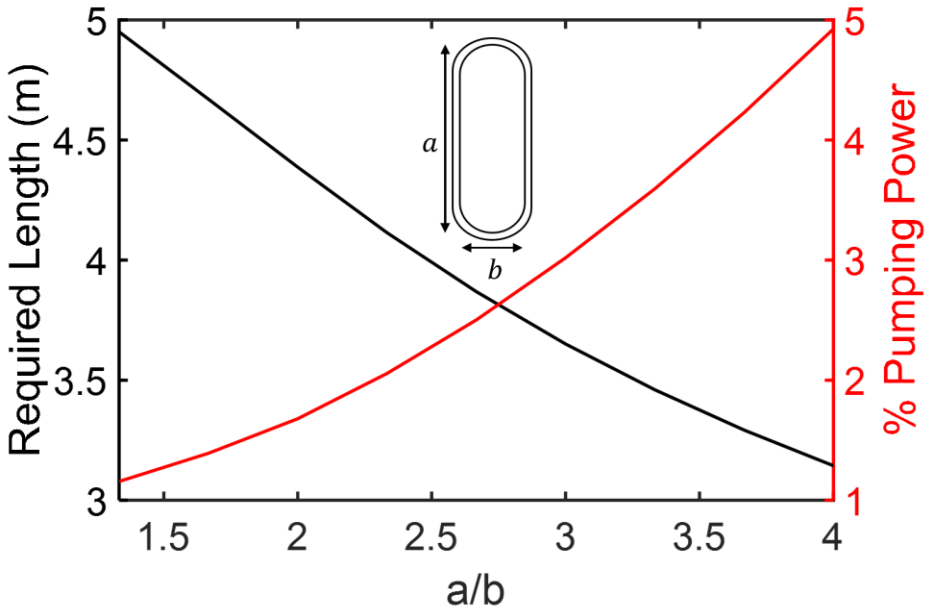

Figure 33. Impact of a/b ratio on the total required length of ECU tubing and the % pumping power required. This ratio compares the required pumping power to the cooling load for a constant flow rate and starting tube of 0.25" for the prototype.

We can once again use the multi-objective design framework discussed previously to generate a Pareto front for the smallest, lightest configuration with the smallest pressure drop in Figure 34. In attempting to keep the pressure drop less than 5% of the overall cooling power, as is recommended in Shah's Handbook [72], we show the Pareto front with the criteria constraints added for ease of reference.

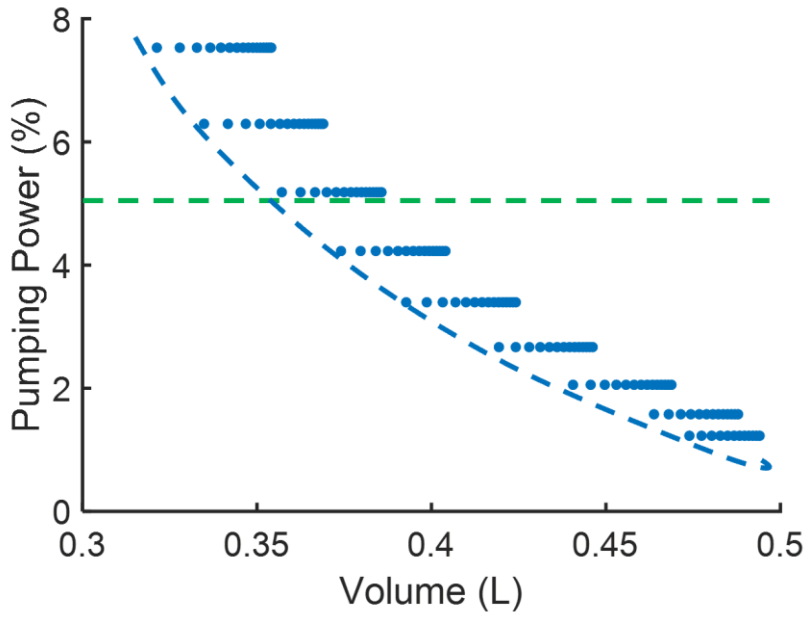

Figure 34. Pareto front for the prototype ECU in terms of pumping power and volume, with a pumping power cutoff value in green.

The final design is the result of much iteration in the machine shop with points along this Pareto front, while making custom mandrels and understanding runout lengths, limits of tube bending, and exploring the limits of different copper alloys. While the traditional serpentine evaporator is well established, it is not an effective design for the application of a surface evaporator. The serpentine path sets the design volume at the limit of the centerline radius (CLR) of off the shelf parts, as the overall width scales with $CLR * 2 * (n_{turn} - 1)$, where n_{turns} is the number of bends in the ECU to meet the total length requirements while maintaining the geometric constraints allowed for the ECU. As such, we propose a tiered hairpin design that ensures easy manufacturing and assembly, while minimizing the amount of thermal mass of water required to maintain desired reserve levels. Figure 35 serves as a qualitative guide to the difference in water reserve and footprint required. Quantitatively, the serpentine path has a very poor footprint utilization (the ratio of the projected footprint of the copper tubes to the footprint of the water reservoir [m^2]). Only 25% of the footprint has ECU tubing over it, creating a significant amount of thermal mass in the extra water required to maintain a minimal reservoir height to prevent dry out. For the prototype, this requires an additional 200 grams of water on top of what is needed for the adsorption process, while the proposed tiered hairpin design has >90% footprint utilization, requires less metal to make the reservoir to hold the water, and requires 50% less water than the serpentine design.

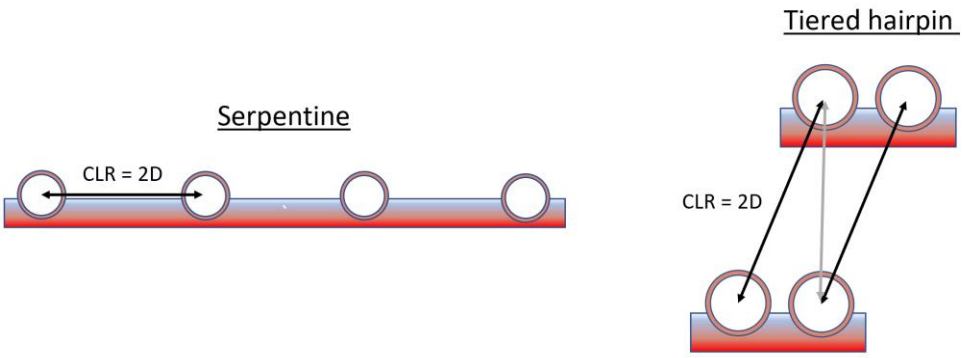

Figure 35. Comparison of the footprint and thermal mass of serpentine versus tiered hairpin design.

Additional benefits of this approach are that tubes can be bent into hairpins and flattened into shape as one part to eliminate misalignment, and it require half of the soldered joints required by the serpentine flat tube design. The only thing limiting the gap between tubes for each base is the clearance required to install the return bend. The final assembly of the evaporator can be seen in Figure 36 with an aspect ratio of 2.66 and the final volume was 0.45 L. For reference, both the prototype ABU and ECU are shown in the vacuum chamber where they will be tested.

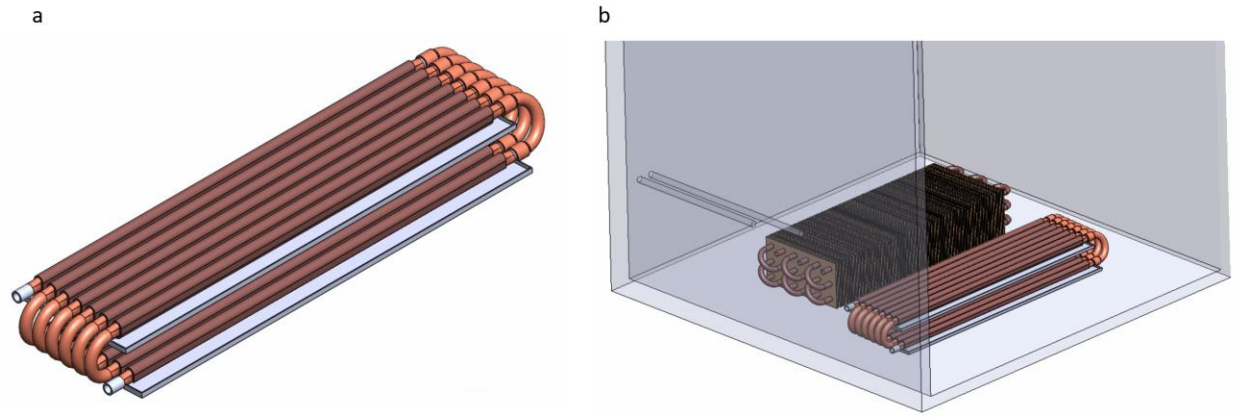

Figure 36. a) Tiered hairpin ECU design, shown with water trays for reference. b) Final ABU and ECU prototypes shown in the 16"x16"x16" vacuum chamber for future testing.

3.8. SUMMARY

In order to navigate the many tradeoffs between the mass, volume, and pumping power required for the desired performance of our scaled down waste heat driven sorption cooling system, we examined the key parameters that impact thermal and mass transfer processes involved in the cooling cycle for both the ABU and the ECU. We introduced a multi-objective optimization approach at the system level for the

first time to shift away from the trend found in literature that takes a very narrow view of optimizing sorption cooling devices. Ultimately, we propose a tube and adsorbent (AQSOA Z02) coated copper foam-fin assembly for the ABU, and a tiered hairpin assembly of capillary wicking flat tubes for the ECU. With a combined volume of less than 2.1 L, our device is predicted to produce 150 W of cooling power for a 400 second total adsorption-desorption cycle. We expect the kinetics of this prototype device to be exactly the same as the full scale device by keeping the cycle time and coating thicknesses the same. Due to manufacturing limitations, we were not able to achieve the same SCPs that the full-scale device is projected to have, but testing of this scaled prototype will validate the newly proposed systems level optimization approach presented in this chapter. Despite the lower SCPs, the 1:10 scale prototype is projected to have the highest SCPs at the system level than anything tested in literature to date for these operating conditions, and would be a significant step forward in translating this technology out of the laboratory and into industry. The framework itself was used to design two different systems due to its generality, and promises to be a useful tool for the field moving forward to avoid too much emphasis on material performance. A rendering of the final 1:10 scale device is shown in Figure 37, with a total volume of 2 L. The form factors of the final ABU and ECU were created together via additional paired geometric constraints in the optimization. This ensures minimal surface area and mass of the required vacuum enclosure required to be implemented outside of the lab.

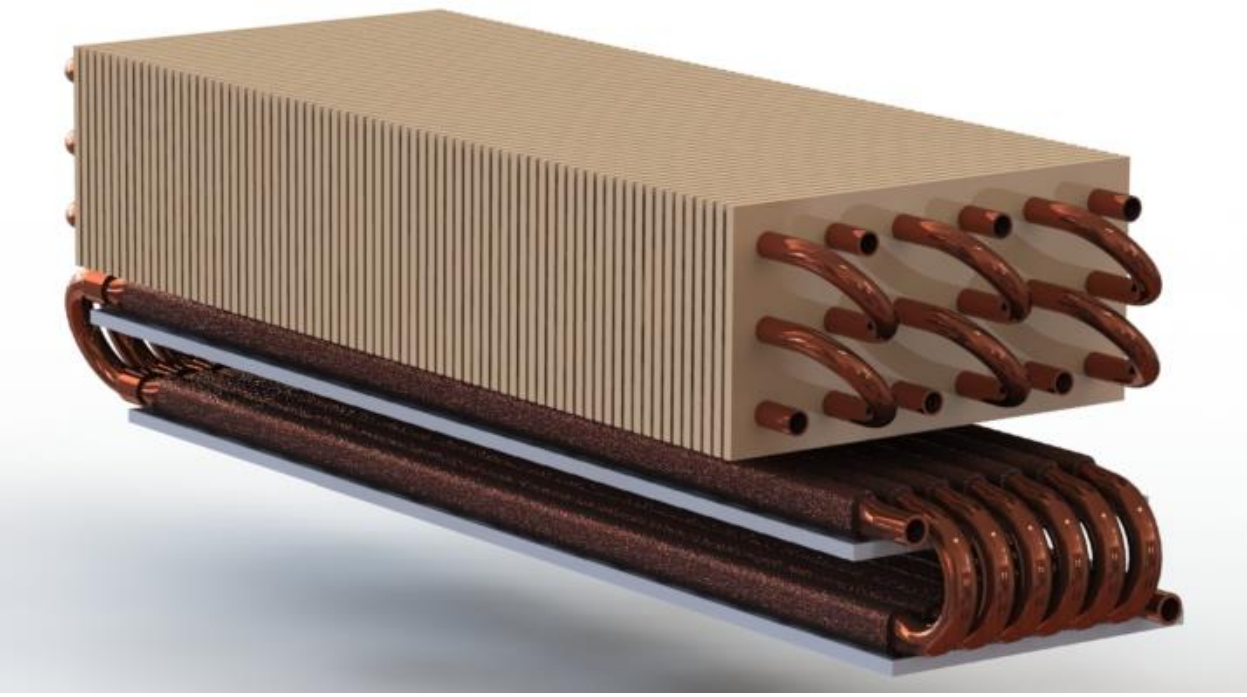

Figure 37. Rendering of the ABU and ECU prototypes currently under fabrication.

Chapter 4

4. Adsorption Coating Fabrication and Testing

In order to validate our modeling approach before finalizing the design, we successfully fabricated samples and developed a testing procedure to evaluate the performance of adsorbent fins. Often in literature, we only see testing of the performance of the material on their own, or mass-based measurements of adsorbent coatings that can be unreliable due to noise introduced by flow rate variations or creep of the attached tubing. These mass-based measurements require large masses to keep experimental uncertainty low and thus do not facilitate testing variations in the coating method or coating porosity. We are able to characterize the uptake of the fabricated adsorbent fins by measuring the heat flux generated during adsorption for various cycle times, adsorption temperatures, flow conditions, coating thicknesses, and fabrication techniques in our custom build adsorption bed simulator, enabling rapid iteration of coating methods and design variations. Through our trials, we developed a novel method of adsorption fin fabrication to maximize the mass transport of the device while achieving an identical packing factor to previous fabrication methods, while simultaneously reducing fabrication time from 24 hours to 5 minutes to enable a more scalable approach.

4.1. ADSORBENT COATING FABRICATION

First, before cleaning the copper foam, a mixture of AQSOA Z02 and deionized (DI) water was created. The mass of Z02 was measured using a mass balance, (Scout SPX2202, OHAUS) with 0.02 mg resolution. Through experimentation, we found that a mass ratio of zeolite: DI water of 1:1 worked best for coatings as it was viscous enough to maintain a good dispersion of particles through the entire deposition process. Too much water created a runny mixture that often resulted in the Z02 separating during the drying process, leaving the top of the sample bare. Once the mixture has gently been stirred for 1 minute to break up any large agglomerations of particles, the mixture is then sonicated in a bath sonicator for 30 minutes. While sonication is occurring, the copper foam was prepared.

In order to make the adsorbent fins, we sourced highly porous (95% porous) copper foam in various thicknesses from Green Creation Electronic Technology in 200x300 mm sheets. The copper foam was cut using a laser-cut template to size for the experiments- 18x18 mm, which corresponds to the size of the heat flux sensor used later in the experiments. Afterwards, the foam was rinsed with DI water, followed by an ethanol rinse to make the foam hydrophilic, followed by another DI rinse. The copper foam was then finally cleaned in 2 M HCl to remove any present oxidation prior to deposition. The foam was then rinsed again with DI water, and immediately dried using compressed air to reduce any oxidation before deposition. We

found that removing any excess water was essential for consistent coating fabrication, as any retained water diluted the zeolite-water mixture used later for deposition, leading to higher than desired porosity and occasionally oxidation during the air drying process. Immediately after drying, the foam should enter the deposition process.

There were multiple deposition processes tested over the course of this work. The initial method followed the work of LaPotin and Kim, and will be referred to as immersion drying, and we introduce a new method of fabrication that creates a dense coating within the copper foam while simultaneously seeding vapor channels to enhance kinetics [37], [73]. In the first method, the cleaned copper foam is placed into a glass dish and Z02 is poured over top until the material is entirely covered. This sample will dry overnight in ambient conditions and takes anywhere from 12 to 24 hours depending on the environmental conditions and the thickness of the coating.

The second method, introduced for the first time in this work, is called boiling-assisted channel templating (BACT). This method allows for the creation of nearly 1D vapor channels that can be seen without a microscope on our samples, and further visual examination reveals that these vapor channels are ubiquitous throughout the coating. The first step of this deposition method is to dip the copper foam into the mixture for 1 minute to allow for full infiltration of the mixture into the pores. It is then placed on a hotplate at 120 ℃ for 5 minutes. During this process, boiling is visible and bubbles can be seen at the surface of the foam. Various temperatures and loading ratios were tested for this process to achieve a reliable porosity of 0.6 of the resulting adsorbent coating, with 120℃ giving the best results.

In order to measure the porosity of the sample, the samples were made sure to dry for at least 24 hours to reach equilibrium with the laboratory. By using a temperature and relative humidity sensor (RH820U, OMEGA) to measure the relative humidity and temperature of the environment that the sample is in equilibrium with, the mass of the adsorbent can be calculated along with the coating porosity utilizing the measured isotherm of the adsorbent.

4.2. ADSORBENT COATING FABRICATION RESULTS

Samples were created for 0.5, 1.0, 1.5, and 2.0 mm thick copper foam using both approaches.

The immersion drying approach makes it very difficult to tailor the porosity, as the only adjustment that can be made is fine tuning the Z02-water ratio. A higher Z02 loading enables very dense coatings, with porosities as low as 0.4, making it ideal for applications that favor dense coatings, such as a thermal battery. This approach results in samples that resemble a random porous media very well, as is consistent with our previous work. This approach, however, results in a significant amount of material waste- less

than 50% yield of material due to the fact that the entire foam needs to be covered with extra Z02-water mixture to ensure a good coating. It also takes at least 24 hours before the coating is dry enough to remove for the 1.5 and 2 mm samples. In Figure 38, we show a SEM image of the immersion dried sample that shows a uniform coating over the copper foam. In the zoomed in panel of the figure is the coating filling a single pore. It should be noted that the pore is uniformly blocked, with clear sub 5 micrometer voids for vapor to transport through. This sample had a porosity of 0.6, which should have an average void size of approximately 2 μm based on the probabilistic model and seems to be the case when examining the SEM image.

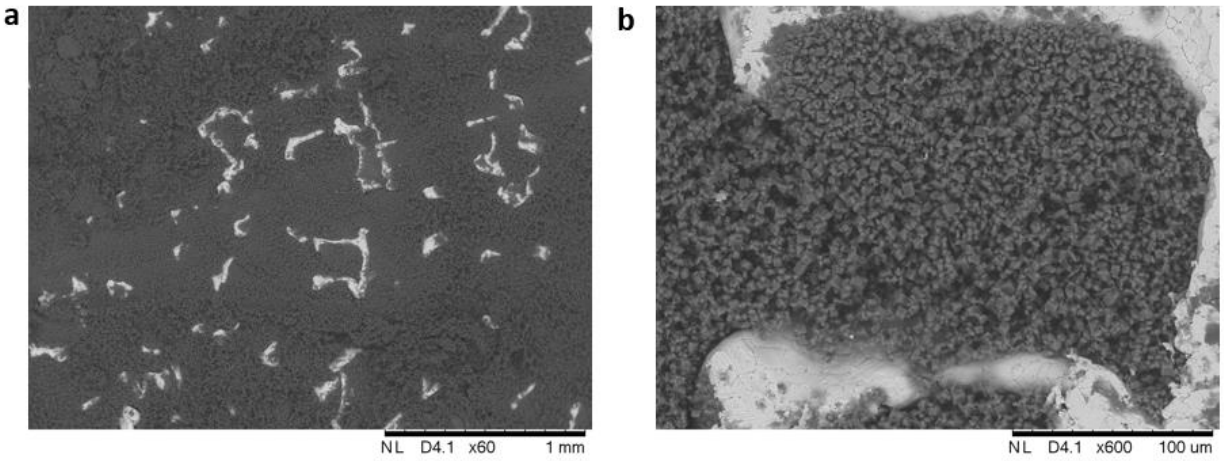

Figure 38. a) SEM image of the immersion dried sample. b) Zoomed in SEM of a single pore of the same sample shown in a).

The BACT process created to address the shortcomings of the immersion drying method in terms of material waste, long processing times, and poor adsorption rate to vapor transport rates due to its small resulting inter-crystalline pore sizes and naturally tortuous structure.

This fabrication method was tested between 80 ℃ to 170 ℃, which is well-below the >400 ℃ threshold where some zeolites begin to break down [74]. A temperature of 120 ℃ was empirically found to be best for achieving the goal porosity of 0.6 consistently. It was also hot enough to create sufficient vapor pressure at the hotplate and copper interface for vapor channels to form, but not too high that the sample would vibrate on the plate. The generated vapor pressure compresses the adsorbent crystals in the mixture against the foam surface to create very dense coating layers on the foam. Even though there are large vapor channels, the component level porosity, which will be referred to as the macro-porosity, is still the same as the immersion drying method. Below 90 ℃, there is still an improvement in the coating performance, but the structure of the adsorbent crystals still resembles a loosely packed random porous media. High

temperatures favor rapid release of vapor and often create vapor channels directed towards the sides rather than 1D channels normal to the hot plate to escape faster as vapor pockets coalesce at the base. The vapor generates enough pressure through the viscous mixture to lift the sample upwards, creating a scaffold of adsorbent crystals that is not structured around copper foam. This is less favorable as the scaffolded adsorbent will have limited heat transfer capability without the copper foam to facilitate heat conduction. These vapor pockets and scaffold can be seen in Figure 39. The coating is very sparse in these areas and is not the most efficient packing for optimal adsorption rate through the full device. We show Figure 40 as a schematic of the result of operation temperature on pore structure. At temperatures below 90 ℃, the coating resembles a random porous media. As the temperature increases, visual boiling can be seen during the process and vapor channels are created. However, at high temperatures, adsorbent scaffold form at the bottom as the vapor pressure lifts the sample off of the surface, creating sparse coatings and less 1D vapor channels as the vapor tries to escape through the bottom of the rapidly dried and porous structure.

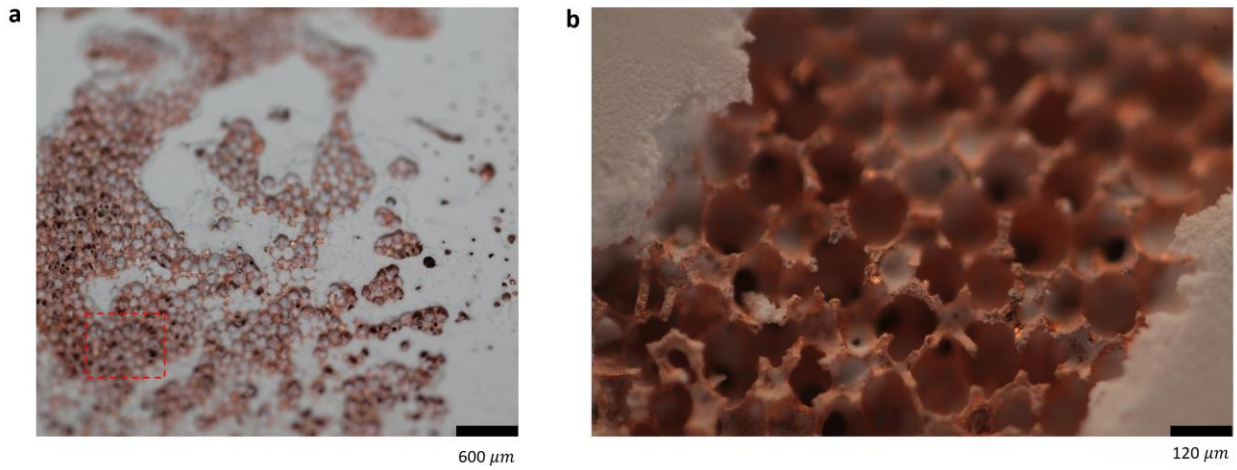

Figure 39. a) BACT sample using 150 ℃, with clear coalesced vapor pockets resulting in large sections of sparsely coated copper foam and clogged pores elsewhere. b) Magnified view of sample revealing limited adsorbent crystals coating the foam in the coalesced vapor pocket.

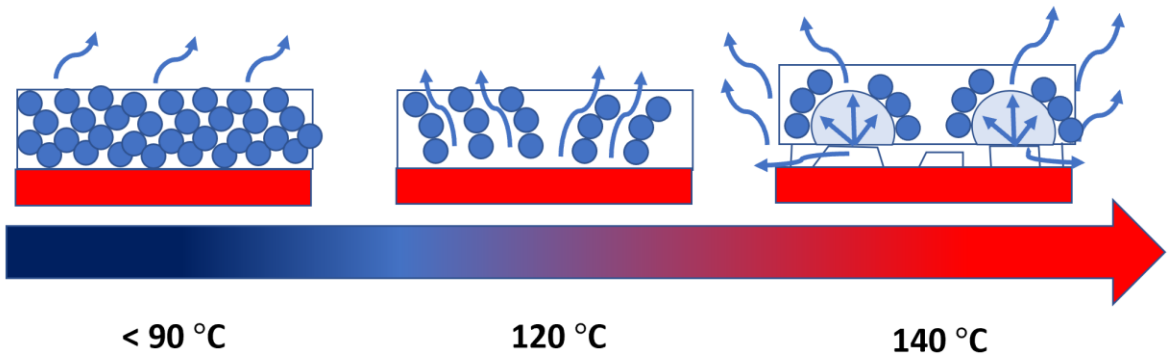

Figure 40. Different adsorbent coating structures as a function of temperature used for BACT coatings, where the blue circles represent adsorbent crystal alignment. Low temperatures result in a random porous media, and high temperatures results in large vapor pockets that escape through sides rather than the top of the coating, as well as scaffolding that forms at the bottom. The red bar represents the hot plate.

In Figure 41, we show the results of a BACT sample and the clear vapor channels that were created. Optical microscopy confirmed that many of the vapor channels are continuous from top to bottom, or are connected to channels that span the thickness. This transforms the mass transfer problem for a majority of the coating from one that reduces the effective diffusivity coefficient for the tortuosity of a random porous media, $\varepsilon^{\frac{3}{2}}$, to a simple 1D diffusion problem in the radial direction limited by Knudsen diffusion of a thin random porous media. For these samples, that transforms the predominant characteristic length scale for water vapor transport from the foam thickness, on the order of millimeters, to the dense 10-30 μm coating

surrounding the copper foam struts. In terms of order of magnitude analysis, while the pore size for diffusion through the adsorbent coating is smaller (10 times smaller than immersion dry samples for the same porosity) for BACT samples, the 100x reduction in the characteristic length scale for a 1 mm sample results in the reduction of the time scale for inter-crystalline diffusivity by 100, enabling rapid adsorption by via the high surface area for adsorption. To confirm this expected enhanced performance, experiments were conducted to characterize these samples along with the baseline samples used for the ABU.

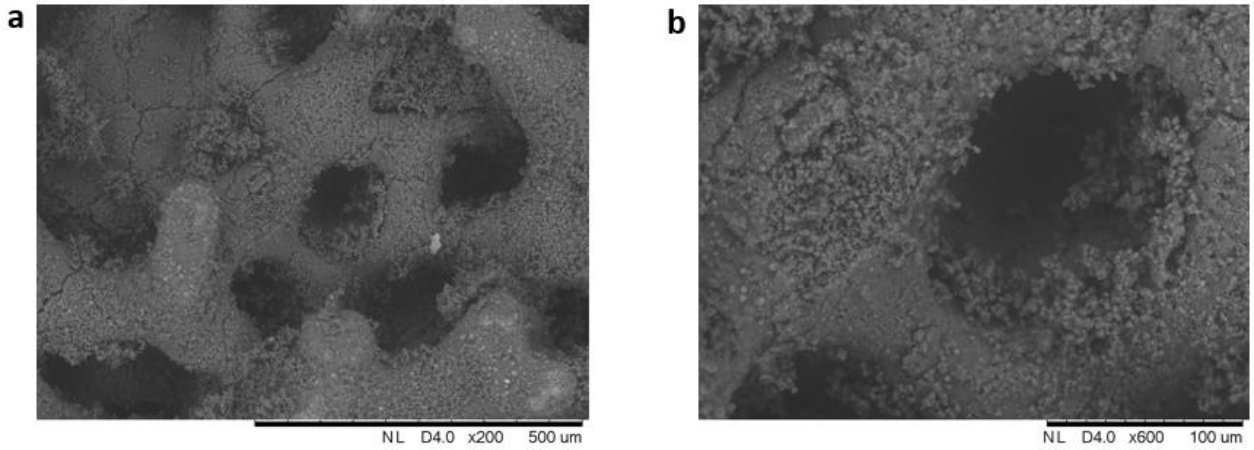

Figure 41. a) SEM image of BACT sample. b) Magnified SEM of a single pore of the same sample in a).

4.3. EXPERIMENTAL SETUP AND PROCEDURE

In order to compare the performance of the traditional ID coatings to the BACT coatings and validate the models used to design the ABU, the experimental setup in Figure 42 was created. This experimental setup obtained the uptake of water by measuring the heat flux at the interface of a temperature-controlled surface and the adsorbent sample. With knowledge of the mass of the adsorbent in the sample and the adsorption enthalpy of the material, the adsorption rate was determined and was integrated to determine the uptake. By controlling the temperature of the coating and the operating relative pressure, we were able to test the adsorbent samples at the various conditions we expect the ABU to experience in field use.

Experiments were conducted in a custom-built Kurt J. Lesker Vacuum chamber. The chamber was connected to a vacuum pump (Pascal 2010 SD, Adixen) vacuum pump that passes through a liquid nitrogen trap to pump down the chamber and remove any non-condensable gases and protect the pump from water vapor. There was a connection to a custom built water vapor generator consisting of a stainless steel, sealed chamber filled with DI water. This water vapor line was opened and closed with a regulated needle valve

that allows for fine control of the flow of vapor to control the vapor pressure inside of the testing chamber accurately. In order to reject the enthalpy of adsorption as the sample adsorbs to maintain a target adsorption temperature, a fluid line was connected to the chamber that was cooled by a circulating chiller (Isotemp II, Fischer Scientific). The chamber was also surrounded with resistive heaters to regulate the chamber temperature to limit radiative losses. We measured the heat flux at the adsorber-cold plate interface using a calibrated heat flux sensor (1: XI 26 9C, gSkin). Fluid inlet and outlet temperatures, sample temperature, and the chamber temperature were measured using J-type thermocouples. The pressure of the chamber at low pressures (<10 Pa) was measured using a pressure transducer (2: 925 MicoPirani,MKS), while the pressure during experiments was measured using a pressure transducer more accurate at low to medium pressures (3: Baratron 722B12TGA2FJ, MKS).

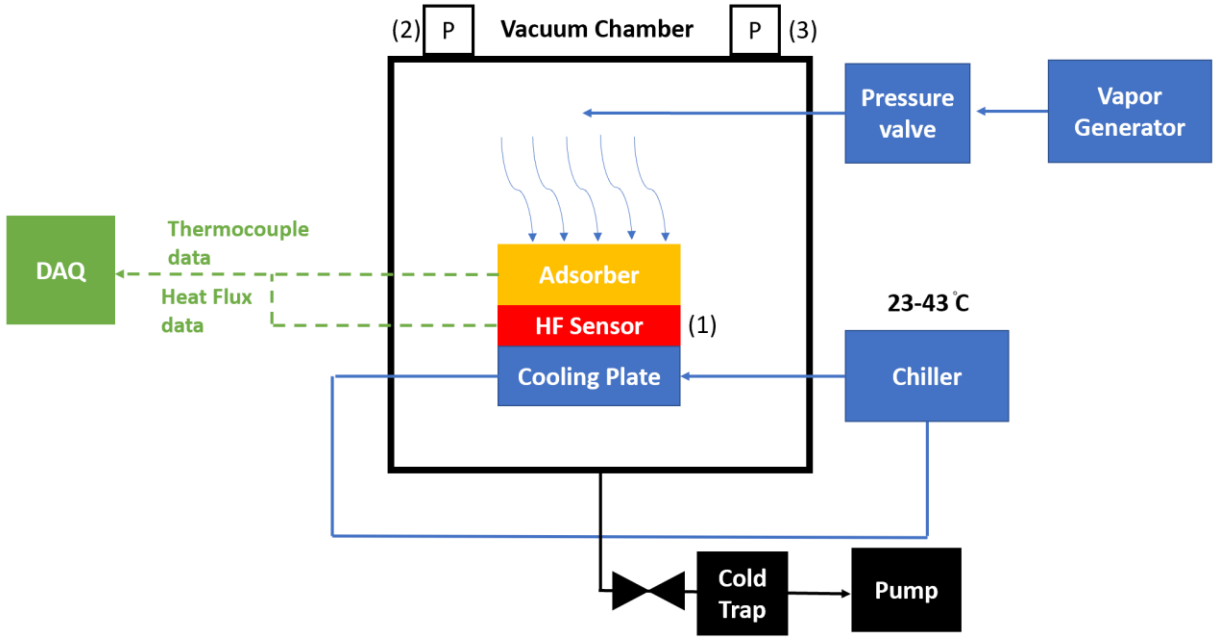

Figure 42. Schematic of experimental setup to test the performance of fabricated adsorbent samples.

The experimental procedure to test the adsorber began with pumping down the chamber to <1 Pa and allowing the sample to desorb for 24 hours. After this period, the chiller was started and the operating temperature was set. The chamber was pumped down again for another hour to ensure the removal of any desorbed gases before beginning experiments. Once a thermal steady state was achieved and the calibrated heat flux measurement was steady, the material was determined to be fully desorbed and experiments began. Once the custom LabView program began recording, the needle valve was opened to allow water vapor to enter the chamber. The pressure was monitored and the valve was adjusted to maintain the target vapor pressure. In this case, it was kept constant to replicate a 5.5 ℃ evaporator temperature. The pressure was

maintained for the target adsorption time, and then the valve was closed to start desorption. The chamber is then evacuated for 30 minutes, and repeated again two more times so that each operating condition is tested three times for the sample. In addition to adsorption performance, the procedure was adapted to show the cyclical ability of the sample through multiple adsorption-desorption cycles by alternating between exposure to water vapor and evacuating the chamber using the vacuum pump. While it was not necessarily representative of the desorption process that was used in the target device (temperature swing desorption rather than pressure swing desorption), the focus of these experiments was to show the repeatability and relative performance of the samples against our model that was created to reflect these conditions and temperature swing experiments were not possible due to shortages in circulating baths. These experiments were run from 23 – 43 ℃ for samples ranging from 0.5 mm to 2 mm using both fabrication methods.

4.4. ADSORPTION EXPERIMENTAL RESULTS

Figure 43 shows the results of a single run of a 1 mm sample with a macro-porosity of 0.6 run with an adsorption temperature of 38 ℃. This sample was one of the first samples made with the BACT method at 90 ℃. The temperature of the coolant did not change by more than 0.5 ℃ during the peak of adsorption, which is in good agreement with our model. We also show that after an initial period that it takes for the chamber to fill with water vapor, the pressure remained constant at the desired pressure to simulate a 5.5 ℃ evaporator water surface. Figure 44 is the result of three experiments with the same sample under the same conditions, showing good repeatability between runs. The average of the results is shown with error bars to represent the uncertainty of the measurements, which is dominated by resolution limitations of the scale to determine the uptake on a g/g basis based on the calculated sample macro-porosity. Also shown is the reference COMSOL model that was used. Our results are in good agreement with the model at the end of the cycle, but it is clear that this sample was adsorbing faster than a random porous media model would predict, as is the current standard in literature. These results encouraged the work done to optimize the fabrication temperature used for the BACT method.

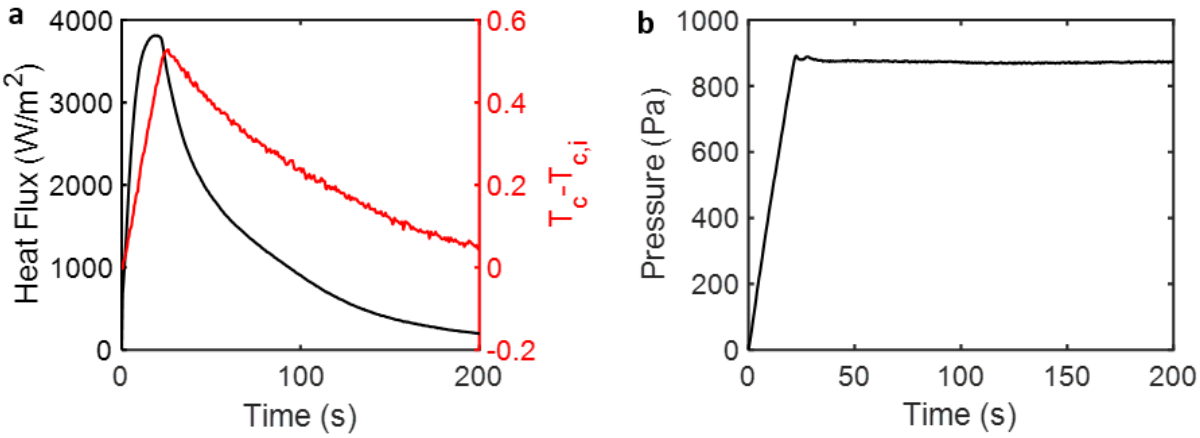

Figure 43. a) Heat flux and change in temperature of the fluid over the course of the 200 second experiment. b) Pressure measured during the experiment using the Baratron pressure transducer. This was a 1 mm sample tested at 38 ℃ with a porosity of 0.6.

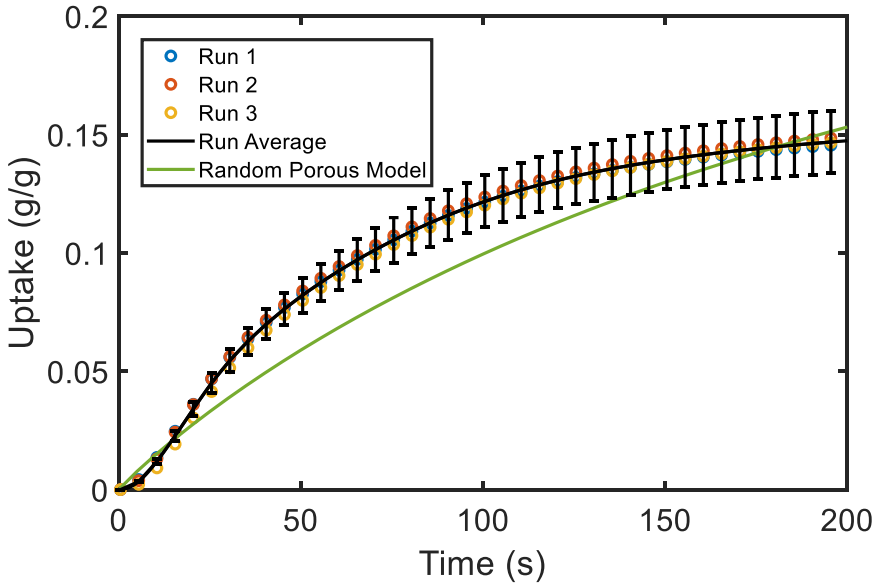

Figure 44. Uptake curve as a function of time for three experimental runs with 1 mm sample at 38 ℃ and 0.6 porosity. The error bars are shown for the run average, and the green line represents the reference model.

The resulting cooling powers calculated from these uptake rates was higher than leading literature values. In the recent work of Sapienza *et al.,* the team produced an adsorption device with *in situ.* SAPO-34 coated al fins with an SCP_{ads} of 1100 W/kg for a half cycle, which translates to 550 W/kg at the full cycle of 700 seconds [56]. The most direct comparison point comes at 177 seconds, shown in Figure 45 as a black diamond with a reported SCP_{ads} of 805 W/kg, whereas our device has an SCP_{ads} of 950 W/kg at that point. With such thin coatings, the thermal time scales become more important and their material choice of

aluminum fins at a length of 20 mm likely led to the reduced performance. Further, their approach has an adsorbent material to heat exchanger mass ratio of 0.15, which was far lower than if the BACT coating method was applied to our prototype device (ratio of 0.35) to achieve better performance. At this design point, our device performed 20% better than this literature leading value from an SCP_{ads} standpoint, but more importantly, promises to be better at the system level with double the ratio of adsorbent to heat exchanger mass.

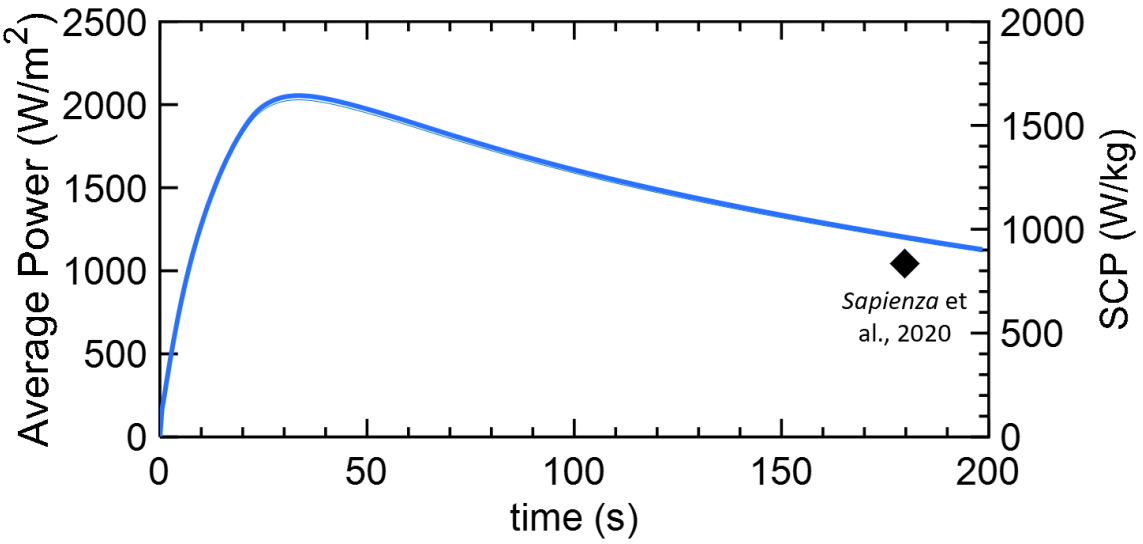

Figure 45. Average Power and SCP of sample as a function of time. Shorter adsorption periods result in higher performance metrics. In black is a reference point from recent work from Sapienza et al. as a literature leading benchmark for Z02 at these conditions[56]**.**

Theoretically, BACT samples would be less limited by sample thickness and thus could have better specific cooling power with respect to mass and volume than thinner samples given their higher packing factor. The results of a sample made with the BACT method for a 120 second cycle time is shown in Figure 46. Not only does the BACT sample significantly outperform the ID sample, but it even approached the practical limit of a straight walled channel. The details of the straight walled channel model can be found in the appendix, but serve as a practical limit of what could be manufactured given current micro-machining technology and standard nano-fabrication techniques. A straight walled channel with a structural pore size of 120 μm and a coating thickness of 20 μm at 0.3 porosity (this will be called the micro-porosity to reflect the local porosity of the adsorbent coating on the copper foam) was used to reflect findings in the SEM images and validated with first order calculations given the macro-porosity of the sample. Straight walled channels of this size would see limited diffusive resistance through the thickness of the foam and were modeled with the ideal case of a constant concentration boundary condition along the pore walls. The performance enhancement can be explained by increasing the surface area of adsorbent exposed to the

boundary concentration due to the negligible mass transfer resistance through an 80 μm channel under vacuum conditions. In terms of order of magnitude analysis, the amount of adsorbent exposed to water vapor in the random porous model scales with the rectangular footprint of the coating. For the unit cell, this only has the surface area of a 120x120 μm rectangle. Adsorbent below this surface only adsorbs water vapor once the material above it approaches saturation, which is a very slow process that increases in length as the coating thickness grows. The straight wall channel, however, has this rectangular footprint surface area in addition to the surface area of a cylinder with 80 μm diameter and a height of 2 mm. This increases this surface area by approximately 35 times. Given that this process is intra-crystalline limited, increasing the surface area of exposed adsorbent is the most effective way to increase the kinetics of the process and thus create higher cooling powers.

The experiments were able to follow this limit closely until the end of the cycle. We attribute this deviation from the limit due to non-uniform coating, especially near the adsorbent coating closer to the side that was at the top during fabrication, as more of the material tended to collect at this side due to the vapor pressure transporting the mixture upwards. While there will be significant surface area for uptake immediately during the adsorption process, these thicker coatings would decrease the adsorption rate as time goes on, as can be seen in Figure 46. It is also expected that there exists some level of tortuosity in the sample still, and removing the tortuosity entirely from the governing equation through the coating thickness would be desired but not yet achieved.

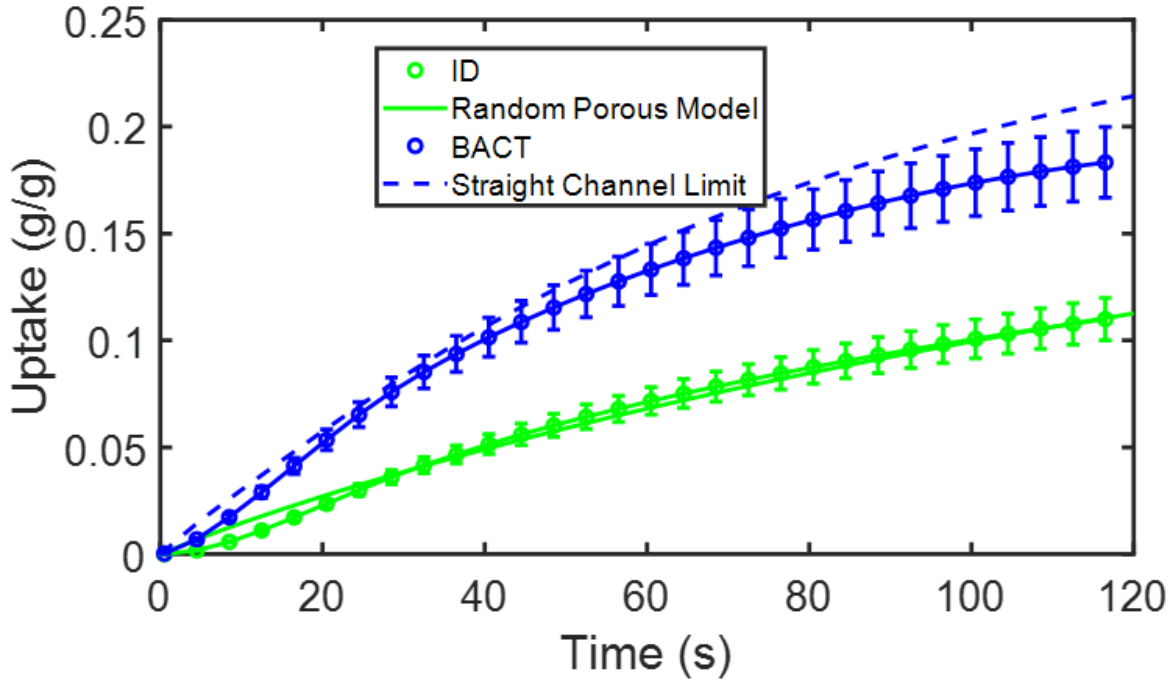

Figure 46. Uptake for optimized BACT sample compared against the straight channel limit model for a 2 mm sample at 38 ℃, 0.68 porosity. Also shown is a 2 mm ID sample tested at 38 ℃, 0.63 porosity compared against the random porous model.

To validate this assumption about the constant boundary concentration used in the model, we can compare the internal mass transfer resistance of the water vapor moving through the channel, to the external mass transfer resistance of the vapor being adsorbed by the adsorbent coating the surface of the channel to gain insight into the limiting resistances. With these resistances defined as $R_{int,m} = \frac{t_{ads}}{\frac{D_k \pi d_{mp}^2}{4}}$ and $R_{ext,m} = \frac{1}{\frac{15\,D_\mu}{r_c^2} * \pi d_{mp} * t_{ads}}$, we can compare their ratios as a function of the vapor templated pore size d_{mp} and adsorbent coating thickness t_{ads}. In Figure 47, we see that compared to previous approaches that only have pore sizes on the order of a single micrometers, we see that $\frac{R_{ext,m}}{R_{int,m}} >> 1$ for a 1 mm sample height after a macro-pore size of 30 μm and 56 μm for a 2 mm thick sample. Our fabrication method was able to create pores much larger at 80 μm. If we compare the mass transfer *Biot* number Bi_m, where $Bi_m = \frac{R_{int,m}}{R_{ext,m}}$, we see that for a 2 mm sample, such as the ones fabricated in our samples, $Bi_m < 0.1$. This implies that a constant concentration through the pore channel is a valid assumption with <0.05% error as the resistance for water vapor transport through the pore is significantly less than the resistance to be adsorbed. For a $Bi_m < 0.01$, we can be very confident in the results and a simple 1D model for diffusion of the vapor through the thin adsorbent coating on the copper foam should have less than a 1% error.

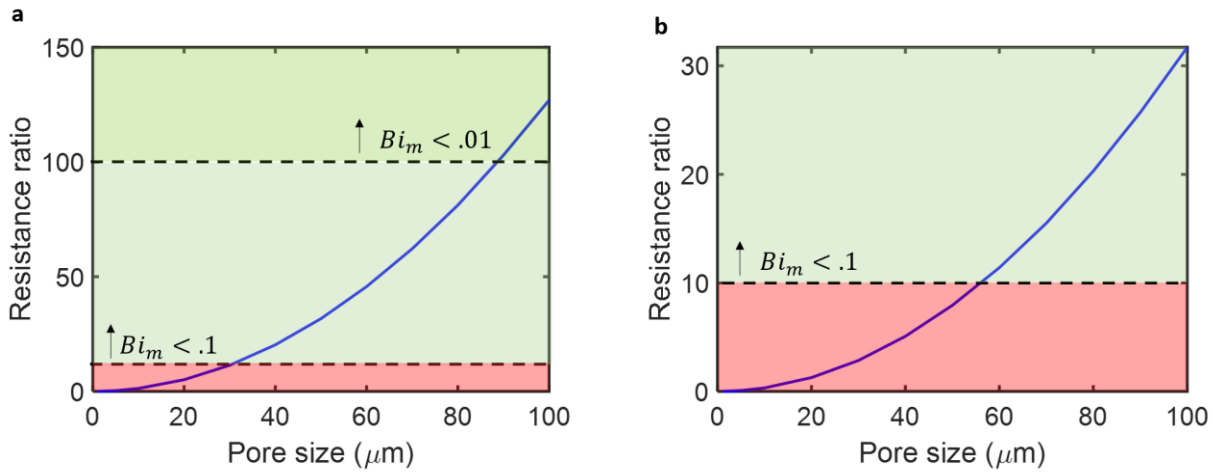

Figure 47. a) Ratio of the mass transfer convective resistance of water vapor to the mass transfer conductive resistance for a coating height of 1 mm. A $Bi_m < 0.1$ indicates that the pore can be modeled as having a constant concentration through the height of the pore. b) Resistance ratio for a 2 mm coating height.

4.5. DISCUSSION AND EXTENSIONS

The 2 mm sample shows a $SCP_{m,ads}$ of 1875 W/kg, an $SCP_{m,ads+foam}$ of 1060 W/kg, and a $SCP_{V,ads}$ of 2.85e3 kW/m^3. Compared to the work of Sapienza et al, where Z02 was deposited into foam and on fins directly, a T_e of 20 ℃, T_a of 30 ℃, and a T_d of 90 ℃. As we discussed previously, the thin tube coatings are not a fair comparison when considered on a volume basis, as very thin coatings always perform well. Compared to coating aluminum foam in the same work, which had an SCP_{ads} = 300 W/kg and a SCP_{tot} of approximately 60 W/kg, if we assume the same adsorbent mass to HX mass ratio from our prototype of 0.35 and a cyclical knockdown of 20% [52],[16], we would be able to have an SCP_{tot} = 375 W/kg. These are very exciting results that warrant further exploration, as it is ~1.5x more mass efficient than the proposed prototype $SCP_{tot,}$, meaning it could cut the mass and volume of the adsorber in half. We will utilize the optimization framework proposed in this work to design a next generation adsorption cooling system using this approach. While this approach holds promise for adsorption cooling, it also has significant opportunity to improve the performance of atmospheric water harvesting, as will be discussed in the future work section.

We have also shown that by tailoring the macro-pore size for hierarchical vapor transport through the adsorbent layer, we can shift the ratio of mass transfer resistances to the point that $Bi_m < 0.1$, indicating that the entire coating of the vapor channel (80 μm in this work) is exposed to the boundary concentration of water vapor. This is a significant improvement over previous work that typically had pore sizes less than a micrometer going through the entire thickness of the adsorbent layer. This effectively increases the surface area of adsorbent coating by 35 times and drastically improves the power generating capabilities of

the adsorbent by reducing the required saturation time. We recommend that for devices that are focused on power generation, the pore size be tailored such that $Bi_m < 0.1$, compared to previous designs that operate on the order of $Bi_m \gg 1$, which is more suited towards thermal energy storage as the objective is to maximize energy density and not necessarily power density. TES systems that may be more focused on storing as much energy as possible for future use. Power density critical applications require rapid cycling, favoring designs that have the fastest kinetics. In fact, setting $Bi_m = 0.1$, we can determine the optimal scaling for the pore size and coating thickness $\frac{t_{ads}^2}{d_{mp} * D_k(d_{mp},T)} = \frac{r_c^2}{600 D_\mu}$ to ensure vapor transport through the macro-pores will not be limited and the highest power for a given amount of adsorbent can be achieved under isothermal conditions.

In the future, we hope to build a predictive model to capture the agglomeration physics in the three phase flow involved in this coating method to predict the coating thickness on the copper foam to aid in further testing and investigating the impact of the macro-pore diameter, layer height, and coating thickness on the device performance. We will then test model against various samples made that vary operational conditions, such as the process temperature, heat flux, or operating pressure, as well as the solvent, adsorbent, mixture viscosity, and structural binder. We have begun the early drawings of a variation of this approach that involves introducing a gas stream, rather than boiling the solvent away, which introduces new operating regimes in terms of pressure and evaporation rate that could not be achieved with temperature alone. We also aim to explore the nanofabrication of these straight walled channels as a structure to apply the BACT method to, in addition to working with suppliers to tailor the pore size of metallic and other foam structures. More work needs to be done to explore the system level mass and volumetric tradeoffs of this approach, much of which can be done leveraging the framework presented in chapters 2 and 3. Finally, we hope to explore the applications that this work might have in the fields of carbon capture, atmospheric water harvesting, catalytic reactions, adsorption-based desalination, and many other adsorption-based systems.

4.6. SUMMARY

We devised a testing setup to characterize the adsorption performance of highly porous copper foam developed using accepted and novel manufacturing methods. The introduction of the BACT method will reduce material waste, fabrication time, and enhances the kinetics of the adsorption process to mimic that of straight walled channels- eliminating the tortuosity term through the foam thickness. With such fast kinetics enabled by high surface area and low mass transfer resistance, we were able to create a coating with a SCP_{ads} of 1875 W/kg, a $SCP_{V,tot}$ of 2.85e3 kW/m^3, and an $SCP_{m,tot}$ of 375 W/kg- all of which are the best of literature to our knowledge. This represents a 2x improvement over the ID sample used to design

the 1:10 scale prototype, which means that it could effectively cut the mass and volume of the device by 1/2 to achieve the same power requirements. The proposed BACT method promises to deliver significant performance enhancements across adsorption devices by decoupling the saturation time from the coating thickness by introducing a new optimization parameter, the size of the straight walled channel pore, to enhance the surface area of exposed adsorbent to the boundary concentration and shift the inter-crystalline diffusive length scale from millimeters to μm. We also show that the ideal macro-pore size or adsorbent layer thickness, depending on whichever is fixed, can be computed based on setting $Bi_m = 0.1$ to ensure that maximum power can be delivered at all times by utilizing the adsorbent coating through the foam thickness. We expect the BACT method to open new doors in other adsorption-based systems, such as carbon capture and atmospheric water harvesting. Further studies will be conducted to create predictive models to capture the coating process parameters and their impact on coating structure, as well as studying the system level mass and volume impacts of tailoring this approach for adsorption systems.

Chapter 5

5. Conclusions and Future Work

5.1. CONCLUSIONS

In this work, we have reviewed the current state of the art in adsorption cooling systems for automotive climate control. We have discussed current design and modeling approaches, as well as the limitations of previous work that was not able to account for system level implications of design considerations for adsorption-based cooling. As a result, the proposed designs were too heavy and bulky for market application. To address this challenge, we partnered with Ford to better understand customer requirements. We then introduced a design and optimization workflow, including new equilibrium maps to help with working pair down selection. We also highlight the importance of designing with the system level mass, volume, and pumping power required to ensure the best design is produced, levering multi-objective optimization methods to generate Pareto-optimal designs.

As a result of this work, we produced an AQSOA Z02 coated fin-tube design for a 1.5 kW ABU with an $SCP_{m,tot}$ of 234 W/kg, and $SCP_{V,tot}$ of 125 kW/m^3. In order to validate the system-level modeling used, we will be testing a 1:10 scale prototype producing 150 W of power with an $SCP_{m,tot}$ of 127 W/kg, and $SCP_{V,tot}$ of 207 kW/m^3, and an adsorbent mass to HX mass ratio of ~3:1. Despite being heavier due to manufacturing limitations, this device was able to be more volume efficient due to a custom hairpin tube design that will be tested for this device and implemented into the next generation ABU. This prototype will be tested with a brand new ECU deign, featuring a custom flattened tube coated with a wicking copper foam to create a very compact evaporator/condenser. This prototype is currently under fabrication and will be tested by the end of 2021.

In addition to a novel design that promises to have the highest $SCP_{m.tot}$ for an adsorption-based system for adsorption temperatures greater than 40 ℃ and a desorption temperature less 100 ℃, we introduce the novel boiling assisted channel templating (BACT) method for enhanced adsorption cooling applications. By understanding the dominant diffusive resistances, we were able to develop a new fabrication method to increase the performance of our coatings by more than double the traditional immersion drying approach per unit mass of adsorbent. The characteristic inter-crystalline diffusive length scale decreased from 1 mm to 20-30 μm, reducing the characteristic inter-crystalline diffusion time scale by about 250. This result helped produce a record $SCP_{m,ads}$ of 1875 W/kg for Z02 at these operating conditions, but has the potential to double the projected $SCP_{m,tot}$ of the prototype currently under fabrication. This approach promises to

bring adsorption based cooling significantly closer to deployment by cutting the required mass and volume of the ABU by a projected 50%. This would translate to a 1.5 kW system with a $SCP_{m,tot}$ of 375 W/kg- 2.5 times that of the work produced by Sapienza under comparable conditions [75]. We also presented a scaling guideline that be used to ensure $Bi_m < 0.1$ by varying the adsorbent layer thickness and macro-pore diameter ratio, as this will lead to optimal performance for adsorption devices focused on maximizing power output.

5.2. FUTURE WORK

The most immediate next steps are to finish the construction of the prototype and test it to validate the system level model predictions. Our adsorbent coating characterization results indicate that the unit-cell model was in good agreement with the experiments, so the experiments at full scale will validate the system level assumptions made. The experiments will include a sweep of adsorption temperatures matching our customer requirements, and various adsorption cycle periods to validate the optimal cycle time predicted in this work.

This work sets the stage for many other future projects. The design optimization framework is currently being applied to atmospheric water harvesting, and is being enhanced further through AI-assisted design optimization via genetic algorithms. This approach has shown good initial results, and is going to be implemented to improve the recommended workflow in this work to generate better future ABU designs. The implementation of a machine learning model trained on the COMSOL simulations has drastically reduced computational time and has helped converge on optimal design features rapidly, and is being investigated further for its integration into adsorption-based cooling design.

Another set of work that comes from this thesis is the refinement of the BACT method. We will explore the impact of characteristic pore sizes generated in this method, and build a model to try to control them through the process temperature, mixture loading and viscosity, particle size, and binding scaffold geometry. Leveraging the generality of the design framework presented in Chapter 2 and Chapter 3, we will explore the system level mass and volume implications of this approach to determine optimal parameters for the best holistic design, depending on if the focus is storage or power based. This will enable this method to be used for multiple applications, from space cooling, catalysis, carbon capture, to atmospheric water harvesting. This last area shows considerable promise, and some initial results are presented below to show its potential.

Atmospheric water harvesting is the process by which water can be pulled out of the air using adsorbents that can then be used for drinking or other applications requiring high quality water. It has the same thermodynamic cycle as our adsorption-based cooling, and uses many of the same materials. In both cases,

it is essential to maximize the adsorption rate to increase cooling power or to maximize the water harvested per day. Using the same models and adjusting the diffusivities to account for the diffusivity of water in air, we are able to compare the potential water adsorbed per day, assuming a 10 minute desorption cycle using resistive heating or combustion to generate heat to desorb the material. We also assume that there is a fan blowing air over the device such that the boundary concentration is equal to the environmental conditions at all time, that also keeps the adsorbent isothermal. In this case, we simulated a material that has an uptake of 0.5 g/g uptake at 27 ℃. While the amount of water adsorbed is relative in Figure 48, the timescale analysis will hold for any uptake as it is a function of nondimensional uptake. This assumes an 80 μm pore with 30 μm coating thickness, a macro-porosity of 0.6 and local coating porosity of 0.3.

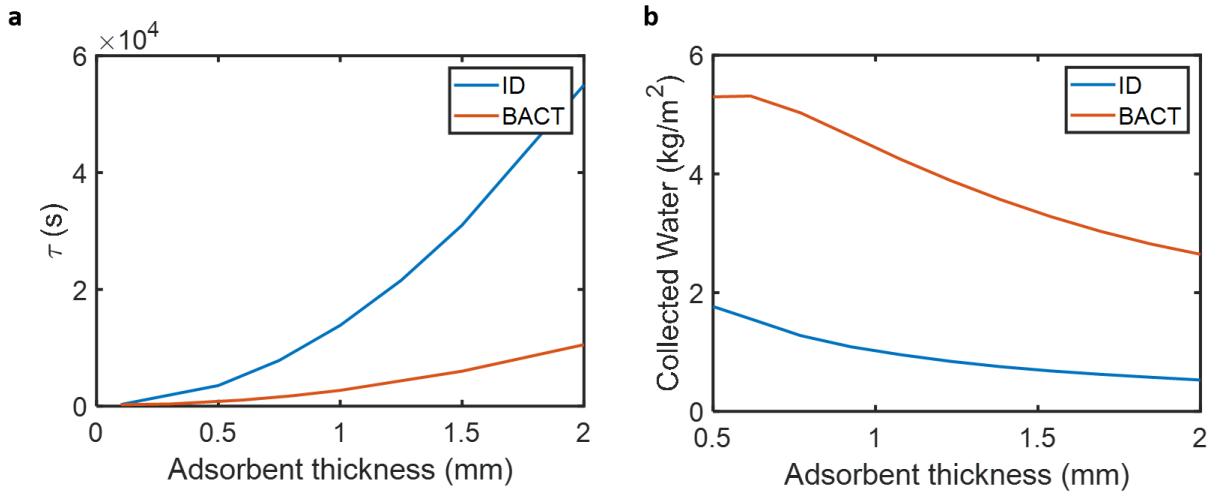

Figure 48. a) Characteristic time to adsorb $\left(1-\frac{1}{e}\right)\Delta w$ for traditional ID and BACT samples. b) Collected water in kg/m^2 of device as a function of adsorbent thickness for ID and BACT samples.

In Figure 48, we compare the amount of time τ it takes for a fully desorbed coating to adsorb $\left(1-\frac{1}{e}\right)\Delta w$, which in this case was an uptake of 0.316 g/g. The divergence in the characteristic adsorption time grows rapidly as the coating thickness grows due to the lack of exposed adsorbent to humid air and slow transport through the thickness of the coating. For the 2 mm sample, it takes the ID samples 5.2 times longer to adsorb the required amount as the BACT samples do. Shorter cycle times enable more cycles per day, generally resulting in more water produced per day, peaking at 5.3 kg/m^2-day for the BACT sample with a 0.6 mm coating thickness. The ID samples are only able to produce 1.7 kg/m^2-day for the same coating thickness due to its reduced surface area.

5.3. FINAL REMARKS

We hope that this thesis, which has explored the design and optimization of adsorption-based systems, specifically for automotive cooling, will serve as a useful guide for future adsorption system designs. We have presented a general design and optimization procedure that will be useful for any temperature swing adsorption system for energy storage, gas separation (water harvesting), or cooling/heating cycles. We have presented an experimental setup that enables rapid testing of new coating methods, material-binder combinations, and temperature/pressure conditions. This work has addressed these systems from the nanometer scale, up to the meter scale system design. We have examined the creation of adsorption layers from material selection, to the physical or thermal binder used, all the way to inventing new deposition techniques to create new design avenues for higher power densities and water harvesting potential than was possible before. We hope that this work creates a platform for others to build upon to not only improve the performance of adsorption-based devices, but enter their design and analysis with a holistic approach that will lead to the most rapid deployment of a technical platform that promises to address many of the climate related challenges we will face in the coming decades. We show that adsorption cooling is feasible, for the first time, for automotive applications by exceeding industry requirements, and our advancements unlock new potential in atmospheric water harvesting. We look forward to the work we have ahead, and hope that this helps others along the way.

Bibliography

[1] "OECD iLibrary | Climate Change and Social Inequality." [Online]. Available: https://www.oecd-ilibrary.org/content/paper/2c62335d-en. [Accessed: 07-May-2021].

[2] S. N. Gosling and N. W. Arnell, "A global assessment of the impact of climate change on water scarcity," doi: 10.1007/s10584-013-0853-x.

[3] "Drinking-water." [Online]. Available: https://www.who.int/en/news-room/fact-sheets/detail/drinking-water. [Accessed: 07-May-2021].

[4] "LLNL Flow Charts." [Online]. Available: https://flowcharts.llnl.gov/. [Accessed: 07-May-2021].

[5] A. Henry, R. Prasher, and A. Majumdar, "Five thermal energy grand challenges for decarbonization," *Nature Energy*, vol. 5, no. 9. Nature Research, pp. 635–637, 01-Sep-2020, doi: 10.1038/s41560-020-0675-9.

[6] I. Energy Agency, "Energy Technology Perspectives 2020."

[7] E. Garofalo, M. Bevione, L. Cecchini, F. Mattiussi, and A. Chiolerio, "Waste Heat to Power: Technologies, Current Applications, and Future Potential," *Energy Technol.*, vol. 8, no. 11, pp. 1–22, 2020, doi: 10.1002/ente.202000413.

[8] G. J. M. Velders, D. W. Fahey, J. S. Daniel, M. McFarland, and S. O. Andersen, "The large contribution of projected HFC emissions to future climate forcing," *Proc. Natl. Acad. Sci. U. S. A.*, vol. 106, no. 27, pp. 10949–10954, Jul. 2009, doi: 10.1073/pnas.0902817106.

[9] M. Wolf, A. Meier, B. Nyland, S. Youn, and W. Jacobs, "Institutions and Governments Can Slow Climate Change by Regulating and Reducing Halocarbon Refrigerant Use," *MIT Sci. Policy Rev.*, vol. 1, pp. 39–43, Aug. 2020, doi: 10.38105/spr.575mrlgdjw.

[10] E. Hastürk, S. J. Ernst, and C. Janiak, "Recent advances in adsorption heat transformation focusing on the development of adsorbent materials," *Current Opinion in Chemical Engineering*, vol. 24. Elsevier Ltd, pp. 26–36, 01-Jun-2019, doi: 10.1016/j.coche.2018.12.011.

[11] V. Palomba, S. Vasta, and A. Freni, "Experimental testing of AQSOA FAM Z02/water adsorption system for heat and cold storage," *Appl. Therm. Eng.*, vol. 124, pp. 967–974, 2017, doi: 10.1016/j.applthermaleng.2017.06.085.

[12] S. Narayanan *et al.*, "A thermophysical battery for storage-based climate control," *Appl. Energy*, vol. 189, pp. 31–43, Mar. 2017, doi: 10.1016/j.apenergy.2016.12.003.

[13] B. Golparvar, H. Niazmand, A. Sharafian, and A. Ahmadian Hosseini, "Optimum fin spacing of finned tube adsorber bed heat exchangers in an exhaust gas-driven adsorption cooling system," *Appl. Energy*, vol. 232, pp. 504–516, Dec. 2018, doi: 10.1016/j.apenergy.2018.10.002.

[14] S. Narayanan, S. Yang, H. Kim, and E. N. Wang, "Optimization of adsorption processes for climate control and thermal energy storage," *Int. J. Heat Mass Transf.*, vol. 77, pp. 288–300, 2014, doi: 10.1016/j.ijheatmasstransfer.2014.05.022.

[15] G. Restuccia, A. Freni, and G. Maggio, "A zeolite-coated bed for air conditioning adsorption

systems: Parametric study of heat and mass transfer by dynamic simulation," in *Applied Thermal Engineering*, 2002, vol. 22, no. 6, pp. 619–630, doi: 10.1016/S1359-4311(01)00114-4.

[16] S. Graf, F. Lanzerath, A. Sapienza, A. Frazzica, A. Freni, and A. Bardow, "Prediction of SCP and COP for adsorption heat pumps and chillers by combining the large-temperature-jump method and dynamic modeling," *Appl. Therm. Eng.*, vol. 98, pp. 900–909, Apr. 2016, doi: 10.1016/j.applthermaleng.2015.12.002.

[17] M. Verde, K. Harby, R. de Boer, and J. M. Corberán, "Performance evaluation of a waste-heat driven adsorption system for automotive air-conditioning: Part I – Modeling and experimental validation," *Energy*, vol. 116, pp. 526–538, Dec. 2016, doi: 10.1016/j.energy.2016.09.113.

[18] B. Golparvar and H. Niazmand, "Adsorption cooling systems for heavy trucks A/C applications driven by exhaust and coolant waste heats," *Appl. Therm. Eng.*, vol. 135, pp. 158–169, May 2018, doi: 10.1016/j.applthermaleng.2018.02.029.

[19] A. Frazzica and A. Freni, "Adsorbent working pairs for solar thermal energy storage in buildings," *Renew. Energy*, vol. 110, pp. 87–94, 2017, doi: 10.1016/j.renene.2016.09.047.

[20] A. Freni, G. Maggio, A. Sapienza, A. Frazzica, G. Restuccia, and S. Vasta, "Comparative analysis of promising adsorbent/adsorbate pairs for adsorptive heat pumping, air conditioning and refrigeration," *Appl. Therm. Eng.*, vol. 104, pp. 85–95, Jul. 2016, doi: 10.1016/j.applthermaleng.2016.05.036.

[21] A. Frazzica *et al.*, "Design, realization and testing of an adsorption refrigerator based on activated carbon/ethanol working pair," *Appl. Energy*, vol. 174, pp. 15–24, Jul. 2016, doi: 10.1016/j.apenergy.2016.04.080.

[22] M. A. Lambert and B. J. Jones, "Automotive adsorption air conditioner powered by exhaust heat. Part 2: detailed design and analysis," 2006, doi: 10.1243/09544070JAUTO222.

[23] D. B. Boman, D. C. Hoysall, D. G. Pahinkar, M. J. Ponkala, and S. Garimella, "Screening of working pairs for adsorption heat pumps based on thermodynamic and transport characteristics," *Appl. Therm. Eng.*, vol. 123, pp. 422–434, 2017, doi: 10.1016/j.applthermaleng.2017.04.153.

[24] H. Furukawa, K. E. Cordova, M. O'Keeffe, and O. M. Yaghi, "The chemistry and applications of metal-organic frameworks," *Science*, vol. 341, no. 6149. American Association for the Advancement of Science, 30-Aug-2013, doi: 10.1126/science.1230444.

[25] M. J. Kalmutzki, C. S. Diercks, and O. M. Yaghi, "Metal – Organic Frameworks for Water Harvesting from Air," vol. 1704304, pp. 1–26, 2018, doi: 10.1002/adma.201704304.

[26] Y. Luo, H. H. Funke, J. L. Falconer, and R. D. Noble, "Yiwei Luo, † , ‡ Hans H. Funke, * , † John L. Falconer, † and Richard D. Noble † † ‡," pp. 2–10, 2016, doi: 10.1021/acs.iecr.6b02034.

[27] Y. Yamauchi and J. Na, "Practical MOF Nanoarchitectonics: New Strategies for Enhancing the Processability of MOFs for Practical Applications," 2020, doi: 10.1021/acs.langmuir.0c00236.

[28] E. H. S. and G. W. H. G. Yilmaz1, C. K. Peh1, W. Lu1, J. Abed2, 3, F. L. Meng1, M. Gao1, "Self-seeping polymer-MOF mixed-matrix for autonomous atmospheric water delivery," *Sci. Adv.*, vol. 5, 2020.

[29] M. Jiang, H. Li, L. Zhou, R. Xing, and J. Zhang, “Hierarchically Porous Graphene/ZIF-8 Hybrid Aerogel: Preparation, CO2 Uptake Capacity, and Mechanical Property,” *ACS Appl. Mater. Interfaces*, vol. 10, no. 1, pp. 827–834, Jan. 2018, doi: 10.1021/acsami.7b17728.

[30] L. Wang, H. Xu, J. Gao, J. Yao, and Q. Zhang, “Recent progress in metal-organic frameworks-based hydrogels and aerogels and their applications,” *Coord. Chem. Rev.*, vol. 398, p. 213016, 2019, doi: 10.1016/j.ccr.2019.213016.

[31] C. Lei *et al.*, “Fabrication of metal-organic frameworks@cellulose aerogels composite materials for removal of heavy metal ions in water,” *Carbohydr. Polym.*, vol. 205, pp. 35–41, Feb. 2019, doi: 10.1016/j.carbpol.2018.10.029.

[32] G. S. Lai *et al.*, “A practical approach to synthesize polyamide thin film nanocomposite (TFN) membranes with improved separation properties for water/wastewater treatment,” *J. Mater. Chem. A*, vol. 4, no. 11, pp. 4134–4144, 2016, doi: 10.1039/c5ta09252c.

[33] A. A. Askalany, S. K. Henninger, M. Ghazy, and B. B. Saha, “Effect of improving thermal conductivity of the adsorbent on performance of adsorption cooling system,” *Appl. Therm. Eng.*, vol. 110, pp. 695–702, 2017, doi: 10.1016/j.applthermaleng.2016.08.075.

[34] A. Karmakar, V. Prabakaran, D. Zhao, and K. J. Chua, “A review of metal-organic frameworks (MOFs) as energy-efficient desiccants for adsorption driven heat-transformation applications,” *Appl. Energy*, vol. 269, no. March, p. 115070, 2020, doi: 10.1016/j.apenergy.2020.115070.

[35] Y. Zhong, T. Fang, and K. L. Wert, “An adsorption air conditioning system to integrate with the recent development of emission control for heavy-duty vehicles,” 2011, doi: 10.1016/j.energy.2011.04.032.

[36] M. Hamdy, A. A. Askalany, K. Harby, and N. Kora, “An overview on adsorption cooling systems powered by waste heat from internal combustion engine,” *Renewable and Sustainable Energy Reviews*, vol. 51. Elsevier Ltd, pp. 1223–1234, 31-Jul-2015, doi: 10.1016/j.rser.2015.07.056.

[37] S. Narayanan *et al.*, “Thermal battery for portable climate control,” *Appl. Energy*, vol. 149, pp. 104–116, Jul. 2015, doi: 10.1016/j.apenergy.2015.03.101.

[38] K. H. Cho *et al.*, “Rational design of a robust aluminum metal-organic framework for multi-purpose water-sorption-driven heat allocations,” *Nat. Commun.*, vol. 11, no. 1, pp. 1–8, Dec. 2020, doi: 10.1038/s41467-020-18968-7.

[39] “JSA - JIS B 8627-3 - Gas engine driven heat pump air conditioners - Part 3: Ducted gas engine driven heat pump air conditioners - Testing and rating for performance | Engineering360.” [Online]. Available: https://standards.globalspec.com/std/1316080/jis-b-8627-3. [Accessed: 08-May-2021].

[40] A. LaPotin, H. Kim, S. R. Rao, and E. N. Wang, “Adsorption-Based Atmospheric Water Harvesting: Impact of Material and Component Properties on System-Level Performance,” *Acc. Chem. Res.*, vol. 52, no. 6, pp. 1588–1597, 2019, doi: 10.1021/acs.accounts.9b00062.

[41] A. K. Sharma, “Modeling and simulation of a downdraft biomass gasifier 1. Model development and validation,” *Energy Convers. Manag.*, 2011, doi: 10.1016/j.enconman.2010.10.001.

[42] M. F. de Lange, K. J. F. M. Verouden, T. J. H. Vlugt, J. Gascon, and F. Kapteijn, "Adsorption-Driven Heat Pumps: The Potential of Metal–Organic Frameworks," *Chem. Rev.*, vol. 115, no. 22, pp. 12205–12250, Nov. 2015, doi: 10.1021/acs.chemrev.5b00059.

[43] J. S. Lee *et al.*, "Porous Metal-Organic Framework CUK-1 for Adsorption Heat Allocation toward Green Applications of Natural Refrigerant Water," *ACS Appl. Mater. Interfaces*, vol. 11, no. 29, pp. 25778–25789, 2019, doi: 10.1021/acsami.9b02605.

[44] S. Wang *et al.*, "A robust large-pore zirconium carboxylate metal–organic framework for energy-efficient water-sorption-driven refrigeration," *Nat. Energy*, vol. 3, no. 11, pp. 985–993, 2018, doi: 10.1038/s41560-018-0261-6.

[45] D. Lenzen *et al.*, "A metal–organic framework for efficient water-based ultra-low-temperature-driven cooling," *Nat. Commun.*, vol. 10, no. 1, pp. 1–9, 2019, doi: 10.1038/s41467-019-10960-0.

[46] J. J. Low, A. I. Benin, P. Jakubczak, J. F. Abrahamian, S. A. Faheem, and R. R. Willis, "Virtual high throughput screening confirmed experimentally: Porous coordination polymer hydration," *J. Am. Chem. Soc.*, vol. 131, no. 43, pp. 15834–15842, Nov. 2009, doi: 10.1021/ja9061344.

[47] M. F. De Lange, K. J. F. M. Verouden, T. J. H. Vlugt, J. Gascon, and F. Kapteijn, "Adsorption-Driven Heat Pumps: The Potential of Metal-Organic Frameworks," *Chem. Rev.*, vol. 115, no. 22, pp. 12205–12250, 2015, doi: 10.1021/acs.chemrev.5b00059.

[48] J. Canivet, J. Bonnefoy, C. Daniel, A. Legrand, B. Coasne, and D. Farrusseng, "Structure-property relationships of water adsorption in metal-organic frameworks," *New J. Chem.*, vol. 38, no. 7, 2014, doi: 10.1039/c4nj00076e.

[49] J. Canivet, A. Fateeva, Y. Guo, B. Coasne, and D. Farrusseng, "Water adsorption in MOFs: Fundamentals and applications," *Chemical Society Reviews*, vol. 43, no. 16. 2014, doi: 10.1039/c4cs00078a.

[50] B. Coasne, A. Galarneau, R. J. M. Pellenq, and F. Di Renzo, "Adsorption, intrusion and freezing in porous silica: The view from the nanoscale," *Chem. Soc. Rev.*, vol. 42, no. 9, 2013, doi: 10.1039/c2cs35384a.

[51] B. Coasne, K. E. Gubbins, and R. J. M. Pellenq, "Temperature effect on adsorption/desorption isotherms for a simple fluid confined within various nanopores," in *Adsorption*, 2005, vol. 11, no. 1 SUPPL., doi: 10.1007/s10450-005-5939-y.

[52] Y. I. Aristov, I. S. Glaznev, and I. S. Girnik, "Optimization of adsorption dynamics in adsorptive chillers: Loose grains configuration," *Energy*, vol. 46, no. 1, pp. 484–492, Oct. 2012, doi: 10.1016/j.energy.2012.08.001.

[53] H. Kim *et al.*, "Characterization of Adsorption Enthalpy of Novel Water-Stable Zeolites and Metal-Organic Frameworks," *Sci. Rep.*, vol. 6, no. June 2015, pp. 1–8, 2016, doi: 10.1038/srep19097.

[54] J. Ammann, B. Michel, and P. W. Ruch, "Characterization of transport limitations in SAPO-34 adsorbent coatings for adsorption heat pumps," *Int. J. Heat Mass Transf.*, vol. 129, pp. 18–27, Feb. 2019, doi: 10.1016/j.ijheatmasstransfer.2018.09.053.

[55] M. Wu *et al.*, “Metal- and halide-free, solid-state polymeric water vapor sorbents for efficient water-sorption-driven cooling and atmospheric water harvesting,” *Mater. Horizons*, 2021, doi: 10.1039/d0mh02051f.

[56] V. Palomba *et al.*, “Evaluation of in-situ coated porous structures for hybrid heat pumps,” *Energy*, vol. 209, 2020, doi: 10.1016/j.energy.2020.118313.

[57] X. H. Li, X. H. Hou, X. Zhang, and Z. X. Yuan, “A review on development of adsorption cooling - Novel beds and advanced cycles,” *Energy Conversion and Management*, vol. 94. Elsevier Ltd, pp. 221–232, 01-Apr-2015, doi: 10.1016/j.enconman.2015.01.076.

[58] R. Z. Wang, J. Y. Wu, Y. X. Xu, Y. Teng, and W. Shi, “Experiment on a continuous heat regenerative adsorption refrigerator using spiral plate heat exchanger as adsorbers,” *Appl. Therm. Eng.*, vol. 18, no. 1–2, pp. 13–23, 1998, doi: 10.1016/s1359-4311(97)00038-0.

[59] Z. Xu *et al.*, “Study on heat transfer and cooling performance of copper foams cured MIL-101 adsorption unit tube,” *Energy*, vol. 191, p. 116302, 2020, doi: 10.1016/j.energy.2019.116302.

[60] A. Freni, L. Bonaccorsi, L. Calabrese, A. Caprì, A. Frazzica, and A. Sapienza, “SAPO-34 coated adsorbent heat exchanger for adsorption chillers,” *Appl. Therm. Eng.*, vol. 82, pp. 1–7, May 2015, doi: 10.1016/j.applthermaleng.2015.02.052.

[61] L. Yong and K. Sumathy, “Review of mathematical investigation on the closed adsorption heat pump and cooling systems,” *Renew. Sustain. Energy Rev.*, vol. 6, no. 4, pp. 305–338, Aug. 2002, doi: 10.1016/S1364-0321(02)00010-2.

[62] M. Alonso, E. Sainz, F. A. Lopez, and K. Shinohara, “Void-size probability distribution in random packings of equal-sized spheres,” *Chem. Eng. Sci.*, vol. 50, no. 12, pp. 1983–1988, Jun. 1995, doi: 10.1016/0009-2509(95)00061-9.

[63] E. Alpay and D. M. Scott, “The linear driving force model for fast-cycle adsorption and desorption in a spherical particle,” *Chem. Eng. Sci.*, vol. 47, no. 2, pp. 499–502, Feb. 1992, doi: 10.1016/0009-2509(92)80041-A.

[64] C. T. Hsu, P. Cheng, and K. W. Wong, “Modified Zehner-Schlunder models for stagnant thermal conductivity of porous media,” *Int. J. Heat Mass Transf.*, vol. 37, no. 17, pp. 2751–2759, Nov. 1994, doi: 10.1016/0017-9310(94)90392-1.

[65] A. Cengal, Yunas; Ghajar, *Heat and Mass Transfer: Fundamentals and Applications*, Fifth Edit. 2016.

[66] C. F. Colebrook, “Turbulent Flow in Pipes, with Particular Reference to the Transition Between Smooth and Rough Pipe Laws,” *J. Inst. Civ. Eng. London*, vol. 11, pp. 133–156, 1939.

[67] C. F. . Mills, A.F.;Coimbra, *Heat Transfer*, Third. San Diego: Temporal Publishing LLC, 2016.

[68] G. N. Vanderplaats, *Numerical Optimization Techniques For Engineers and Designers*, Third. Colorado Springs, CO: Vanderplaats Research and Development, 2001.

[69] J. B. Statnikov, Roman B.; Matusov, *Multi-Criteria Opimtization in Engineering*, First. New York: International Thomson Publishing, 1995.

[70] F. M. White, *Fluid Mechanics*, 6th ed. New York, NY, 2008.

[71] O. G. Jones, “An improvement in the calculation of turbulent friction in rectangular ducts,” *J. Fluids Eng. Trans. ASME*, vol. 98, no. 2, pp. 173–180, Jun. 1976, doi: 10.1115/1.3448250.

[72] R. K. Shah, *Fundamentals of Heat Exchnager Design*, 1st ed. Wiley, 2003.

[73] A. LaPotin *et al.*, “Dual-Stage Atmospheric Water Harvesting Device for Scalable Solar-Driven Water Production,” *Joule*, vol. 5, no. 1, pp. 166–182, Jan. 2021, doi: 10.1016/j.joule.2020.09.008.

[74] L. Z. Zhang, “Design and testing of an automobile waste heat adsorption cooling system,” *Appl. Therm. Eng.*, vol. 20, no. 1, pp. 103–114, Jan. 2000, doi: 10.1016/S1359-4311(99)00009-5.

[75] M. Verde, L. Cortés, J. M. Corberán, A. Sapienza, S. Vasta, and G. Restuccia, “Modelling of an adsorption system driven by engine waste heat for truck cabin A/C. Performance estimation for a standard driving cycle,” *Applied Thermal Engineering*, vol. 30, no. 13. Elsevier Ltd, pp. 1511–1522, 2010, doi: 10.1016/j.applthermaleng.2010.04.005.

Appendix

COMSOL MODEL TO EVALUATE AXIALLY SYMMETRIC ASSUMPTION OF UNIT CELL

Figure 49 shows the 3D model used in the beginning of this work, but was computational expensive. Given the symmetry of the problem, we created a radially symmetric model to use to accelerate the optimization process. Figure 50 shows that there was a negligible difference between the two models, and validated the use of the 2D model instead of the 3D model.

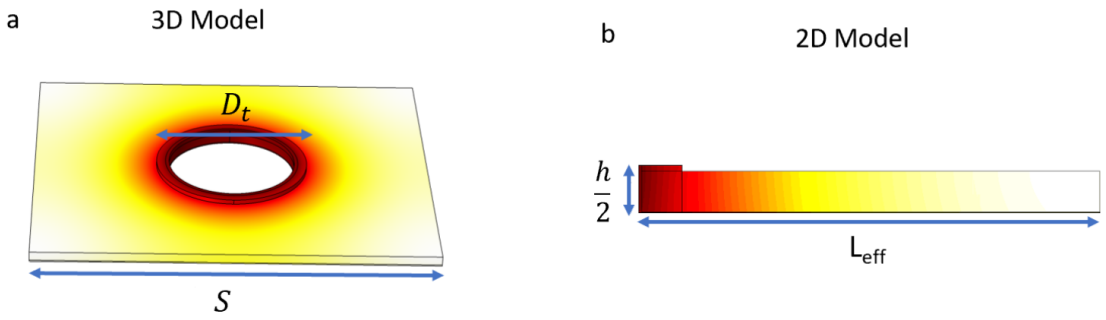

Figure 49. a) 3D model of adsorption bed unit cell. b) 2D model of unit cell with D_eff scaled to match the square unit cell area.

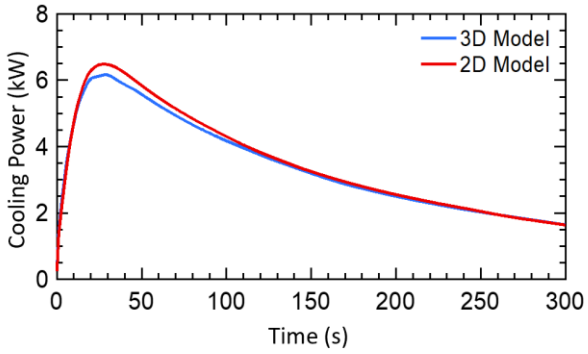

Figure 50. Comparison of cooling power curves for 3D and 2D COMSOL models.

CYCLICAL STABILITY

In the experiments described in Chapter 4, cyclical stability tests were completed to validate the assumption that the ABU would reach steady state by its third cycle. This is confirmed by the experimental results shown in Figure 51 for a 200 second adsorption and desorption time. The larger peak during adsorption compared to desorption can be accounted for by the larger enthalpy of adsorption compared to desorption (h_{ad}~$1.4 * h_{fg}$). While the first peak is significantly higher, this is also expected as the enthalpy of adsorption is significantly higher at low uptakes than for higher uptakes as stronger water-adsorbent interactions occur in the beginning of adsorption. The consistency of the second and third cycle peaks show that the adsorption and desorption have reached their steady state value and that we can use the values to determine the resulting cooling power for steady state operation of 200 second cycles.

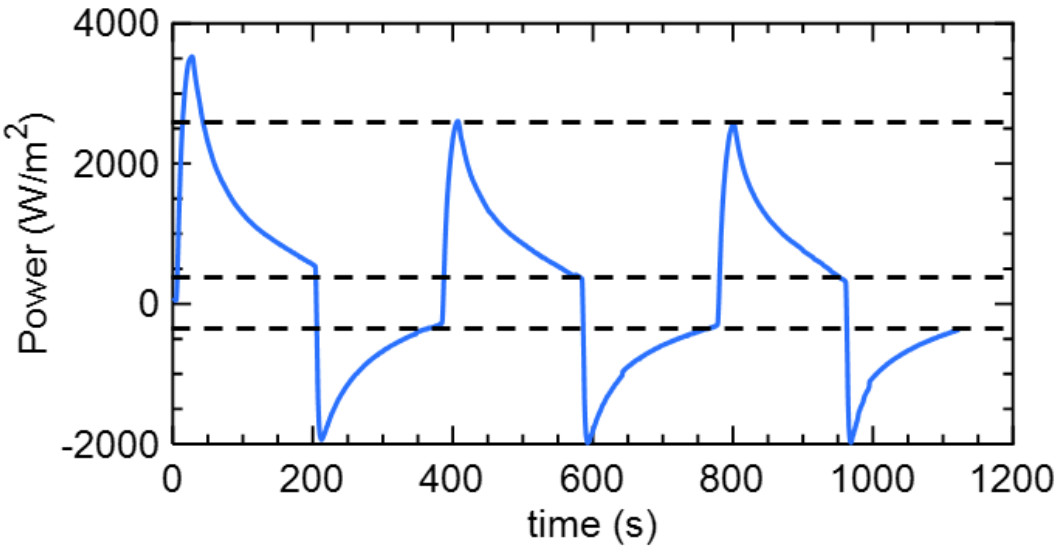

Figure 51. Adsorption and desorption cycle with 1mm sample at 38 ℃ with a porosity of 0.6. This is measurement of the heat flux measured during the experiment. The initial curve is first curve after sitting in vacuum for 30 min, and the second and third peaks represent steady state. Dashed black lines are shown as a reference to highlight the repeatability of each cycle.

MODELING STRAIGHT CHANNEL PORES

To create an upper limit for practical adsorbent coating designs to compare the BACT samples against in this work, we created a straight channel pore model in COMSOL. This model was almost identical to the model used for the ABU optimization, except the we are only modeling a single pore within the adsorbent coating. We assume that this channel has a pore diameter of 80 μm, as was found to be the average diameter of the pores of the BACT method. Based on the macro-porosity measurements of the adsorbent coating,

we are able to calculate the local porosity of the coating on the copper foam to be 0.3. At this macro-pore size, the concentration at the boundary can be approximated as constant. While the adsorbent coating layer now as very small intra-crystalline pore sizes that impede transport, it's the coating thickness t_{coat} is so small that the timescale to diffusive through the dense-thin coating is still on the order of 10 times faster than through a 1 mm coating. In Figure 52, we show a schematic of the straight channel pore model, as well as the results at 75 seconds into a 120 second adsorption cycle to show the nearly uniform uptake through the coating to validate this assumption. The concentration at the boundary is derived from the partial pressure of vapor created by the evaporator at 5.5 ℃. As was discussed in the Chapter 4, there is a coolant loop running underneath of the heat flux sensor to absorb the heat generated by the adsorbent. The right-hand side of the coating is assumed to have no heat or mass transfer assuming that there is another coating of equal thickness at the neighboring pore.

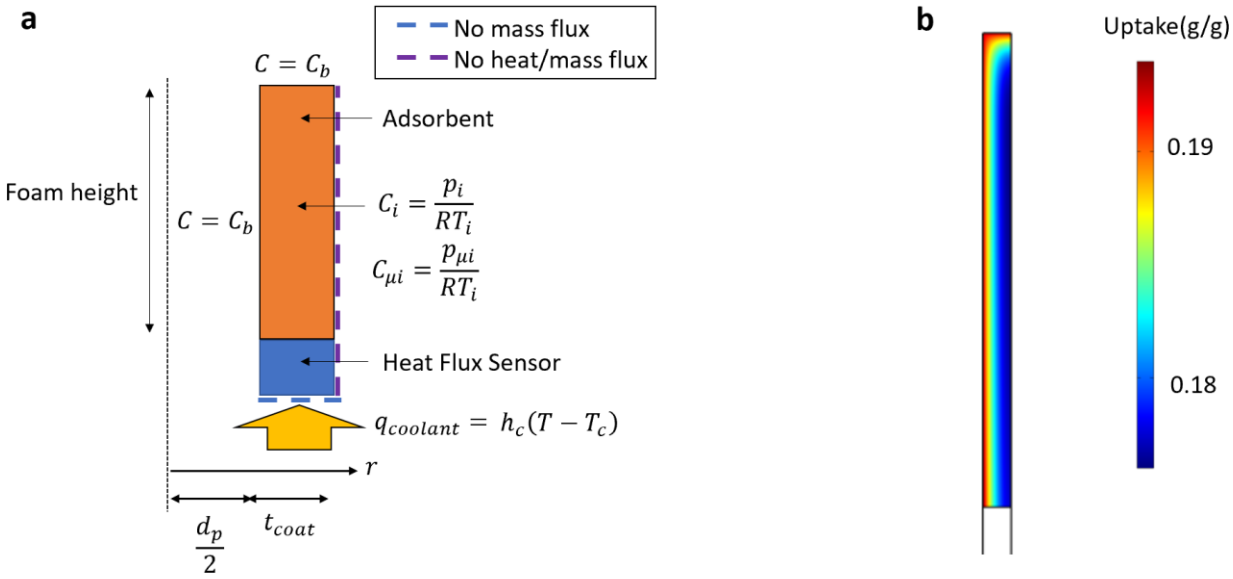

Figure 52. a) Boundary conditions for the straight channel pore model. b) The uptake at 75 seconds for a 1mm tall, 20 micrometer adsorbent coating shows a very small spatial dependence due to the small length scale of the coating.